PROPERTIES OF MUONS AND JETS IN PROTON-ANTIPROTON COLLISIONS AT 540 AND 630 GEV CENTRE OF MASS ENERGY.

Jonathan Mark Streets

Thesis submitted for the degree of Doctor of Philosophy.

Department of Physics,
Faculty of Science and Engineering,
The University of Birmingham.

1986

Synopsis

This thesis describes the details of the author's work within the UA1 experiment at the SPS collider at CERN. The introductory chapter describes the original proposals for the UA1 experiment, and the basic theoretical concepts behind the proceeding work. The second chapter gives a description of the apparatus, indicating the reasons for the subsequent improvements and the methods of analysis described in later chapters.

The remaining chapters represent the bulk of the work to which the author feels he has made a substantial contribution. Chapter III describes the upgrade of the UA1 muon trigger system before the 1983 run, and tackles problems associated with microprocessor programming and interface electronics. Chapter IV is a short description of work from the period between October 1982 and spring 1983, when new muon detectors were tested for use in UA1. For this, the author joined a small team to investigate the properties of Iarocci chambers, leading to tests in a beam from the SPS. Chapter V describes some early analysis of the properties of jets and their fragmentation, from the author's first and second years. Finally in chapter VI there is the analysis of the 1984 muon-jet data, with a comparison to Monte Carlo calculations. This project, started in the summer of 1985, compares theoretical calculations with the data and presents the differential cross-section for the transverse momentum of the muon.

To my Mother and Father.

Acknowledgements

The UA1 Collaboration contains over 150 names, and it would be impossible to acknowledge all those who have contributed to this thesis on one page, I shall therefore only mention those directly associated with the work presented here. First I would like to thank Professor D.Colley and Professor J.Dowell for the use of the facilities of the department and for the chance to work on the UA1 experiment. I would also like to thank my supervisor, Dr.I.Kenyon, for his advice and encouragement over the last few years. This work would not have been possible without the funding from the Science and Engineering Research Council, and the University of Birmingham.

During my studies at CERN I have had the privilege to have discussions with many people, but the following require special mention as they have had a direct influence on this thesis. In an order related to the order of subjects in the index, I would like to thank; Dr.J.Wilson, for his help with the understanding of the electronics of the muon trigger; Dr.H.Reithler, for letting me work with his trigger system, and for his ideas on the VMEFT program; Drs.S.Cittolin, M.Demoulin, W.Haynes, for answering many questions about CPUA1; Drs. K.Sumorok and T.Markiewicz for letting me work with their Iarocci tubes; Dr.I.Kenyon and Dr.N.Ellis for their help with the analysis of the muon-jet data; and the UA1 scanning team at Birmingham, namely Professor J.Dowell, Drs.M.Corden, G.Cox, I.Kenyon, P.Watkins, J.Wilson, and Messrs.T.Edgecock, S.Haywood, M.Jimack.

Finally I would like to thank Professor J.Dowell, Dr.N.Ellis & Dr.I.Kenyon for their suggestions about this thesis.

CONTENTS

TABLES

FIGURES

1. INTRODUCTION

Since the last century physicists have been investigating the basic properties of nature by studying the interactions of sub-atomic particles. Their motivation has been to understand the elementary constituents of matter, and the forces between these building blocks. Today, the work requires its own advances in engineering and computing, and in this thesis the author attempts to show some of the methods used and the results obtained in one of the larger experiments in the field of particle physics.

1.1 History of the UA1 Experiment

The UA1 (Underground Area 1) detector is situated on an intersection region on the Super Proton Synchrotron at CERN, and was designed to investigate a new energy region in particle physics. In 1976 C.Rubbia, P.McIntyre and D.Cline [1] suggested that the SPS should be transformed into a collider, which could reach the energy region required to produce the predicted Intermediate Vector Bosons (IVB). When the SPS accelerates protons to a momentum of 450 GeV/c and releases them onto a stationary target, the energy in the centre of mass ($\sqrt{s}$) from which new particles can be made is around 29 GeV, compared to the rest masses of the IVB of 80 to 90 GeV/c^2. However, operated in a proton-antiproton colliding mode the centre of mass energy equals the sum of the beam energies. In a pulsed mode the beams can attain 450 GeV/c but for continuous running there is a limit due to overheating of the guiding magnets in the SPS tunnel, hence only 273 GeV/c beams were used which resulted in a centre of mass energy of 546 GeV. In 1984, the water cooling to the magnets was increased so that a centre of mass energy of 630 GeV could be attained. The highest energy data collected so far by the UA experiments were the 50,000 events taken at 900 GeV during a short run in the spring of 1985. To attain this energy, the particle bunches were kept coasting whilst the beam energies were ramped during a 21.6 second cycle between 100 and 450 GeV, keeping at the maximum energy for 4 seconds per cycle. These data have been used to show trends in minimum bias triggers at increasing $\sqrt{s}$, but only data from the 546 GeV and 630 GeV runs are presented here.

1.2 Motivation for the UA1 Experiment

The principal aim of the UA1 experiment was to test the standard model by searching for the IVBs which mediate the weak force, but in the proposal [2] searches for other possible new physics were mentioned. The theoretical calculation of the masses of the IVBs in the standard model predicts the existence of one or more Higgs bosons arising from the breaking of the gauge symmetry of the electroweak interaction. In the simplest Weinberg-Salam model there is only one Higgs, which is neutral and couples to particles with strengths proportional to their masses. However, no solid predictions of the Higgs mass can be made, and there is no experimental evidence to show that any have been observed.

With the new energy range of the collider it would also be possible to investigate the strong interaction and compare with extrapolations from lower energies such as that of 63 GeV at the Intersecting Storage Rings (ISR) at CERN. De Broglie's wave equation gives a relationship between distance and momentum, and at 630 GeV/c one is probing distances of 0.004 fm, where the proton is no longer a single particle but rather a system containing quarks, antiquarks and gluons, collectively known as partons. UA1 could therefore study the scattering of these particles for which no evidence for further substructure has yet been found. The scattering produces high transverse momentum sprays of particles, named jets, where a struck parton emerges from the nucleon and fragments into colourless particles. At that time, convincing evidence for jets existed only at electron-positron colliders, the highest energy hadron collider was the ISR, where the cross-section for energetic jets with a transverse energy greater than 10 GeV was small. The low momentum debris from the other partons in the event obscured the simple two jet structure which had been seen at comparable energies in electron-positron annihilations.

Finally, there was one other particle which it was thought possible to detect at the collider, namely the sixth quark, top, which would complete the third weak isospin generation (table 1). It was noted in the proposal that the decay of its massive, narrow vector meson might be seen, although it was realised then that a signal would be difficult to extract from the data.

Table 1: The Elementary Fermions

	leptons		quarks	
charge	0	−1	+2/3	−1/3
family				
1	ν_e	e^-	up	down
2	ν_μ	μ^-	charm	strange
3	ν_τ	τ^-	top	bottom

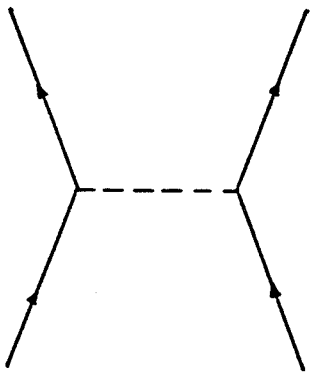

Figure 1: Lowest Order Feynman Diagram

Table 2: The Elementary Forces of Nature

generic name	mediator	associated quantum number
electromagnetic	photon	electric charge
weak	IVBs	weak isospin
strong	gluon	colour
gravitational	graviton	mass

1.3 Basic Concepts in Particle Physics

The equations in particle physics which succeed in describing the forces between particles are not listed here, but it is useful to review some of their basic concepts and introduce some of the associated terms. The reader will find details of the relevant theories discussed in this thesis in the following section, and a thorough description can be found elsewhere [3]. In table 1 we can see the elementary fermions which account for all the substantiated experimental observations in particle physics. The forces acting between these particles can be represented by the diagram in figure 1, showing the exchange of a boson between two particles. Any theoretical calculation begins with one or more similar diagrams, and the prediction of the forces magnitude and direction depends on properties of the vertices. The classification of the known forces then reduces to a classification of the exchanged bosons, electromagnetic interactions arise from photon exchange, the weak interaction from W and Z exchange and strong interaction from gluon exchange. Although it has not been experimentally verified, the force of gravity could then be associated with the exchange of gravitons. The forces are listed in table 2, along with the mediator which transmits the force and the property or quantum number on which the force acts. The forces can all be parameterised at the low energy scale, but in order to predict their effects at the scale of the fermions in table 1 they need to be quantised. After quantisation it is possible to describe the forces at energies and times which are related by Heisenberg's Uncertainty Principle i.e. $\Delta E.\Delta t \approx \hbar$.

The electromagnetic force was formulated by Maxwell in the 1860's, and has been successfully quantised in the theory of QED (Quantum ElectroDynamics). It agrees remarkably well with all experimental results, and requires only one experimental input, usually represented by the dimensionless scale of the force, α_{em}.

The weak interaction was parameterised successfully at low energies by Fermi in the 1930's (eg neutron β-decay and the neutrino cross-section to several GeV), and was quantised to cover the higher energy spectrum by the electroweak theory [4] which combined electromagnetism and the weak interaction, and also predicted the IVBs. As has already been mentioned, the theory predicts the

existence of at least one Higgs boson, which has yet to be found, and it also requires experimental input to calculate the masses of the IVBs.

The strong interaction was understood at the range of the nucleus in the 1930's, and from its parameterisation experiments produced controlled and uncontrolled fission in the 1940's. Its quantisation by Quantum ChromoDynamics (QCD) has been very successful, and is described in more detail in the next section. Unlike the electromagnetic theory, in which photons are electrically neutral, gluons carry colour and so can couple to themselves (the theory is known as non-Abelian). This is negligible in the weak interaction as the coupling strength, α_{em}, is small, but in QCD the corresponding coupling, α_s, is twenty times greater, making the higher order terms significant in the simplest cases of parton scattering. The predictions for experiments at the collider are therefore not yet perfect, and further refinement is needed.

Finally the force of gravity has been included merely for completeness, its influence is far too small to be seen at masses produced at available accelerators. It should be noted that gravity is well described at low energies (≡ large distances), by the theories of Newton and Einstein, however its quantisation remains unsolved, reflecting the difficulties imposed by the nature of the force for experimental investigation.

The ultimate aim is to find the Hamiltonian which describes the four fundamental forces as properties of space and time, and should infer the existence and masses of all the known particles. This is known as the process of grand unification. A significant step was to combine the electromagnetic and weak forces into one. The quantised theories were all originally derived from group theory, where the quantum numbers of the particles are related to the dimension of the sets. The electromagnetic, weak and strong forces can be expressed as the unitary groups U(1), $SU(2)_L$ and SU(3) respectively, so that any grand unification theory (GUT) must reduce to these groups in the low energy limit. Unfortunately the simplest group to do this, SU(5), has been ruled out by recent experimental studies [5]. SU(5) imposes a new force which can transform a quark-quark pair into an anti-lepton and an anti-quark, and gives accurate predictions of the decay of the proton to a neutral pion and a positron. This decay mode has not been observed at the expected lifetime of less than 10^{32} years, and so other

groups have had to be investigated. The current models rely on a symmetry between fermions and bosons but the present experiments have not been able to detect evidence for 'supersymmetric' phenomena, and future experiments at high energies are required to investigate these theories.

1.4 Jets and QCD

In this section we will discuss the properties of particle production at the collider, which will be investigated later in this thesis.

1.4.1 The Parton Model

Fundamental to our understanding of hadrons is the idea that they contain point-like quarks which are bound together by gluons. At low energies, the experimental properties of baryons suggest that they contain three quarks while mesons contain a quark and an anti-quark (known as the valence quarks). In the lowest baryon decuplet the Pauli Principle is apparently violated by the Δ^{++}, and it is essential to introduce a new quantum number, colour. Colour has three degrees of freedom, and by having each quark in the Δ^{++} of a different colour the overall wavefunction of the particle can be antisymmetrised. Quarks obey the property of being confined to hadrons, single quark and di-quark states have not been found in experimental searches. The absence of quark or di-quark states is imposed by the condition that all particles must be neutral in colour (i.e. a colour singlet) e.g. red + blue + green = white, red + $\overline{\text{red}}$ = white, etc.. This condition alone does not explain the absence of $(qqqq\bar{q})$ states or $(qqqq\bar{q}\bar{q})$ states except that they will be energetically unstable with respect to the states $(qqq)+(q\bar{q})$ and $(qqq)+(\bar{q}\bar{q}\bar{q})$ respectively, and hence will decay rapidly. The field particles in this model are gluons which carry the colour force between partons. Colour is thought to form a special unitary group SU(3), in which there would be eight orthogonal coloured gluons,

$$r\bar{b},\ b\bar{r},\ r\bar{g},\ g\bar{r},\ g\bar{b},\ b\bar{g},$$

$$(r\bar{r}-b\bar{b})/\sqrt{2} \text{ and } (r\bar{r}+b\bar{b}-2g\bar{g})/\sqrt{6},$$

and a colour singlet

$$(r\bar{r} + b\bar{b} + g\bar{g})/\sqrt{3}.$$

It is the exchange of coloured gluons which provides the force to bind coloured quarks into hadrons.

As well as the valence quarks, it is possible to excite $q\bar{q}$ pairs in hadrons. These extra quarks are known as sea quarks, and are important in hard scatterings where an energetic particle can pull one of the heavy quarks from the sea, so creating a heavy flavour baryon and meson.

1.4.2 Densities of Partons in Hadrons

The momentum of the i'th parton, p_i, inside the proton is described by its fraction of the longitudinal momentum of the proton, $p_i = x_i p_p$, where $0 \leq x_i \leq 1$ and $\Sigma_i x_i = 1$. For high momentum protons, the momentum of the parton transverse to the direction of the proton is negligible. The structure function, $F_i(x)$, is defined as the probability of finding a parton, i, with a fraction of the proton momentum, x, times the value of x. It is normalised such that

$$\Sigma_{i0} \int^1 F(x_i) dx = 1 \qquad 1.4.1$$

where the sum is over all partons labelled i. The structure functions have been measured directly for quarks in deep inelastic neutrino scattering experiments [6], and it is found that the quarks account for roughly one half of the momentum of the proton. The remaining half is attributed to the gluons in the proton which do not participate in weak interactions, hence it is possible to calculate the gluon structure function of the proton. These structure functions have been evolved to the energies (or Q^2) of the collider by using the Altarelli-Parisi equations [7] in the work by Eichten et al. [8]. The exact functions are given by [8] but they can be approximated by the values in table 3.

The proton structure function has also been measured in UA1 [9], and it compares well with the evolved functions from CDHS (figure 2).

Table 3: Approximate Structure Functions for the Proton

Valence Quarks	$u_V(x) \propto (1-x)^3$
	$d_V(x) \propto (1-x)^4$
Sea Quarks	$u_S(x) = d_S(x) = s_S(x) \propto x^{-1}(1-x)^8$
Gluon	$g(x) \propto x^{-1}(1-x)^5$

1.4.3 Jet Cross-sections

Once we have defined the incoming partons, we need to find the jet cross-section, σ which is defined by the sum of the individual subprocesses where partons i and j interact to form states k and l ($i+j \rightarrow k+l$). This has been calculated [10] and can be expressed as

$$d\sigma/d\hat{t} = \pi\alpha_S^2(Q^2)\hat{s}^{-2}\Sigma_i d\sigma_i/d\hat{t} \qquad 1.4.2$$

where $\hat{s}$ and $\hat{t}$ are two of the Mandelstam variables,

$$\hat{s} = x_i x_j s$$

$$\hat{t} = -x_i x_k s \qquad 1.4.3$$

$$\hat{u} = -x_j x_k s.$$

The scale of the strong interaction, α_S, is defined by

$$\alpha_S(Q^2) = 12\pi\{(33-2n_f)\ln(Q^2/\Lambda^2)\}^{-1}, \qquad 1.4.4$$

where Q^2 is the square of the interaction energy (usually taken as $\hat{s}$), n_f the number of flavours available at this energy, and Λ a constant measured by experiment (approximately 200 MeV).

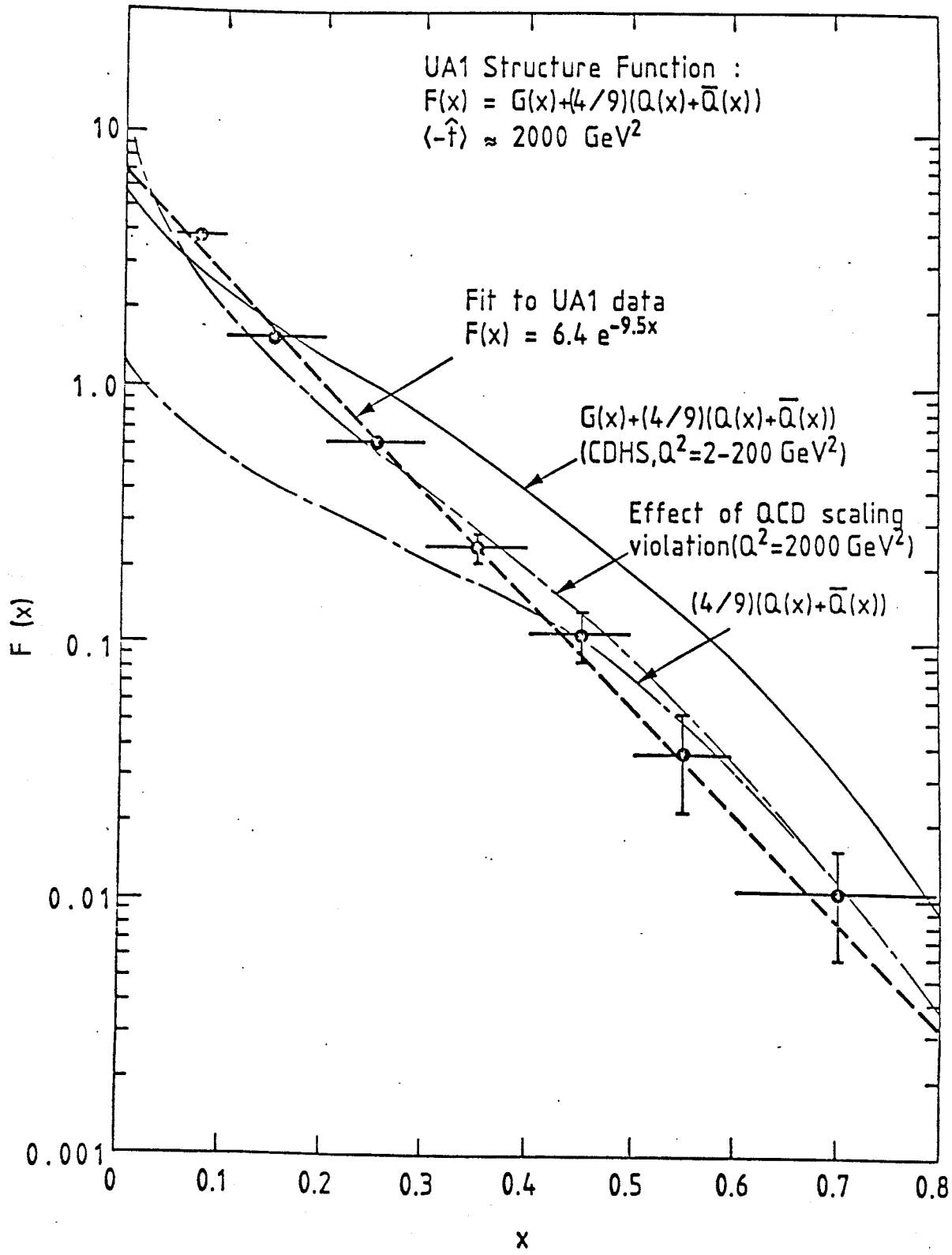

Figure 2: The UA1 Structure Function

The cross-sections of the individual processes are calculated from lowest order QCD, and are defined by

$$d\sigma_i/d\hat{t} = \pi\alpha_s^2(Q^2)|A_i|^2\hat{s}^{-2}. \qquad 1.4.5$$

The lowest order processes have been calculated by Combridge et al. [10] and are presented in figure 3.

The outgoing partons can radiate gluons and quarks at small angles to their direction, which is known as final state bremsstrahlung. This has been formulated by Fox and Wolfram [11] by a Leading Log Approximation, and is included in the Monte Carlo in chapter VI. They have calculated the probability of a parton, i, with mass $\sqrt{t}$ and momentum p_i to propagate from its production and decay into (massless) partons of type j and k, which carry the fractions of momenta zp_i and $(1-z)p_i$. This probability may be expressed as

$$\alpha_s(t)(2\pi t)^{-1}P_{i\to j,k}(z), \qquad 1.4.6$$

where $P_{i\to j,k}(z)$ may take one of three forms;

1. Gluon radiating from a quark

$$P_{q\to qG}(z) = 4(1+z^2)/3(1-z)$$

2. Gluon decay to $q\bar{q}$ pair

$$P_{G\to q\bar{q}}(z) = 0.5(z^2+(1-z)^2)$$

3. Gluon radiating from a gluon

$$P_{G\to GG}(z) = 6(1-z+z^2)^2/z(1-z)$$

These processes diverge in this model as partons would radiate an infinite number of soft gluons. To overcome this a cut-off is introduced to halt the process when the invariant mass of the parton reaches $\sqrt{t_c}$. The value of $\sqrt{t_c}$ is paramaterised from e^+e^- data, and is taken as 7 GeV in chapter VI. The bremsstrahlung ceases when the original t has been converted into the transverse momentum of the partons.

The contributions of the different QCD subprocesses

	Subprocesses	$\|A\|^2$
1	$q_i q_j \to q_i q_j$, $q_i \bar{q}_j \to q_i \bar{q}_j$ $(i \neq j)$	$\frac{4}{9}(\hat{s}^2 + \hat{u}^2)/\hat{t}^2$
2	$q_i q_i \to q_i q_i$	$\frac{4}{9}\left(\frac{\hat{s}^2+\hat{u}^2}{\hat{t}^2} + \frac{\hat{s}^2+\hat{t}^2}{\hat{u}^2}\right) - \frac{8}{27}\frac{\hat{s}^2}{\hat{u}\hat{t}}$
3	$q_i \bar{q}_i \to q_i \bar{q}_i$	$\frac{4}{9}\left(\frac{\hat{s}^2+\hat{u}^2}{\hat{t}^2} + \frac{\hat{t}^2+\hat{u}^2}{\hat{s}^2}\right) - \frac{8}{27}\frac{\hat{u}^2}{\hat{s}\hat{t}}$
4	$q_i \bar{q}_i \to gg$	$\frac{32}{27}\left(\frac{\hat{u}^2+\hat{t}^2}{\hat{u}\hat{t}}\right) - \frac{8}{3}\left(\frac{\hat{u}^2+\hat{t}^2}{\hat{s}^2}\right)$
5	$gg \to q_i \bar{q}_i$	$\frac{1}{6}\left(\frac{\hat{u}^2+\hat{t}^2}{\hat{u}\hat{t}}\right) - \frac{3}{8}\left(\frac{\hat{u}^2+\hat{t}^2}{\hat{s}^2}\right)$
6	$q_i g \to q_i g$	$-\frac{4}{9}\left(\frac{\hat{u}^2+\hat{s}^2}{\hat{u}\hat{s}}\right) + \left(\frac{\hat{u}^2+\hat{s}^2}{\hat{t}^2}\right)$
7	$gg \to gg$	$\frac{9}{2}\left(3 - \frac{\hat{u}\hat{t}}{\hat{s}^2} - \frac{\hat{u}\hat{s}}{\hat{t}^2} - \frac{\hat{s}\hat{t}}{\hat{u}^2}\right)$

Figure 3: Lowest order Matrix Elements in $p\bar{p}$ collisions [10]

1.4.4 Fragmentation in Jets

Fragmentation is the process by which a struck parton emerging from a baryon forms a hadron jet, and this hadronisation can tell one about the gluon fields. The fragmentation is described by a function $D_i^h(z)$, which is the probability of finding a particle, labelled h, emerging from a struck parton, labelled i, with a fraction between z and $z+dz$ of the linear momentum of the parton. It is normalised such that

$$ {}_0\int^1 z D_i^h(z) dz = 1. \qquad 1.4.7 $$

The fragmentation function is measured in electron-positron, electron-proton and neutrino-proton scattering experiments which can identify the particle type, h, and measure the cross-section, i.e.

$$ \Sigma\sigma(i) D_i^h(z) = \frac{d\sigma(h)}{dz}, \qquad 1.4.8 $$

where on the left hand side we have

- $\sigma(i)$ for the production cross section of the parton, i;
- $D_i^h(z)$ for the probability of fragmentation of the parton, i, to the hadron, h, summed over all the partons;

and on the right hand side there is the differential cross section of the hadron.

The fragmentation functions have been studied in e^+e^- and it has been found that the fragmentation of light quarks and gluons are very similar, i.e.

$$ D_q^h(z) \approx D_g^h(z) \approx 3(1-z)^2/z. \qquad 1.4.9 $$

For heavy quarks, work on e^+e^- has shown that [12],

$$ D_Q^h(z) = z(1-z)^2[1-(2-\varepsilon)z+z^2]^{-2}. \qquad 1.4.10 $$

The value of ϵ is small, and is fitted for the quark type, it is consistent with $\epsilon = m_s^2/m_Q^2$, where m_s is the mass of the strange quark, and m_Q the mass of the quark under investigation.

The two simple viewpoints which have been developed to parameterise the fragmentation functions are the independent fragmentation (IF) model of Field and Feynman [13], and the string model of Andersson et. al. [14]. The IF model makes two assumptions (i) each parton fragmentation depends only on the momentum from the parton next higher up in the process and (ii) at high momentum all distributions scale so that they depend only on the ratio of the hadronic to parton momenta. The process of this fragmentation is continued until all the particles are on mass shell, conserving the original energy and momentum of the initial parton. This leads to the picture in 4(a), which shows the jets from a gluon-gluon interaction.

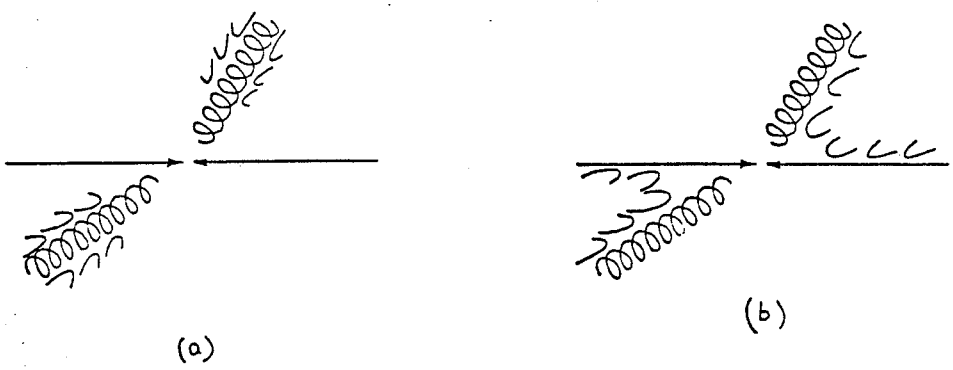

Figure 4: Fragmentation in gluon-gluon scattering

In the string model the partons are assumed to act as terminators of a colour string which fractures, pulling quark-antiquark pairs from the vacuum, indicated in 4(b). The strings are associated with the stretching colour field between partons which exist between the coloured objects. The string model is so called due to a property of the strength of the force, F, between partons separated by distance, x, expressed as

$$F = k \quad (x > 1 \text{ fm}), \qquad 1.4.11$$

where k is a constant determined experimentally. This gives an energy density in the field like

$$dE = kdx. \qquad 1.4.12$$

The model propagates particles by the breaking the string with an equal probability along its length, and terminates when the particles are all on mass shell. The energy density, k, can be calculated from fitting the mass levels of the excited meson states. It is found by experiment that the square of the masses of hadron states are proportional to their spin, forming Regge trajectories [15]. Assuming the (massless) quarks to revolve relativistically about an (infinitely) strong string of length R, the energy inside the field is then

$$E = 2\int_0^R \frac{k\,dr}{\sqrt{(1-\beta^2)}} = kR\pi \qquad 1.4.13$$

where the velocity of the quark, β, in units of c, is given by r/R. The angular momentum can be calculated from

$$J = \frac{2}{\hbar c}\int_0^R \frac{kr\beta\,dr}{\sqrt{(1-\beta^2)}} = \frac{kR^2\pi}{2\hbar} + \text{const.} \qquad 1.4.14$$

Eliminating R we obtain $J = bE^2 + a$, where b depends on the string constant, k. A measurement of the slope of the trajectory therefore measures k, and it is found that $k \cong 1$ GeV/fm.

The two models have been compared extensively with data from electron-positron colliders, but it has been found that to a first approximation both models can be fitted to the data by fine tuning of parameters. Intuitively, one could hope to differentiate between the models by looking at the track distribution between the jets and the beam jets, higher track densities would indicate that the string model would be a better candidate than the IF model.

1.4.5 Heavy Flavour

There are several reasons for investigating Heavy Flavour production:

- For a high quark mass one can assume that the interaction had a hard scatter. This implies that $\alpha_s(m_Q^2)$ is small, so that perturbation theory calculations will be reliable.

- In $Q\bar{Q}$ systems, the velocity of the quarks will be small, so that non-relativistic potential models may be used.
- In $Q\bar{q}$ systems, the heavy quark will carry most of the momentum, and the decay of the meson will reduce to a calculation at the quark level (this property is known as the spectator model).

In the spectator model, the heavy quark is assumed to decay with a life-time which is independent of the flavour of the lighter quark, and with a width proportional to the fifth power of the quark mass. This model predicts that the properties of the meson decay are identical to the properties of the decay of the heavy flavour quark in the meson. (This is not perfectly true, because the lifetime of the D^0 is half that of the D^+, indicating spectator interactions.)

The weak decay conserves helicity which leads to difference in the p_t^{μ} spectra from b and c decays. As helicity is conserved, then at high momentum a quark will tend to donate more of its momentum to a particle than an anti-particle. For $c \rightarrow \mu^+ \nu s$, the p_t spectra of the ν and s will be harder than that of the μ^+, but for $b \rightarrow \mu^- \bar{\nu} c$, the μ^- and c will be harder than the $\bar{\nu}$. This predicts that b decays contribute a larger fraction of high p_t muons in the muon-jet analysis (chapter VI) than c decays.

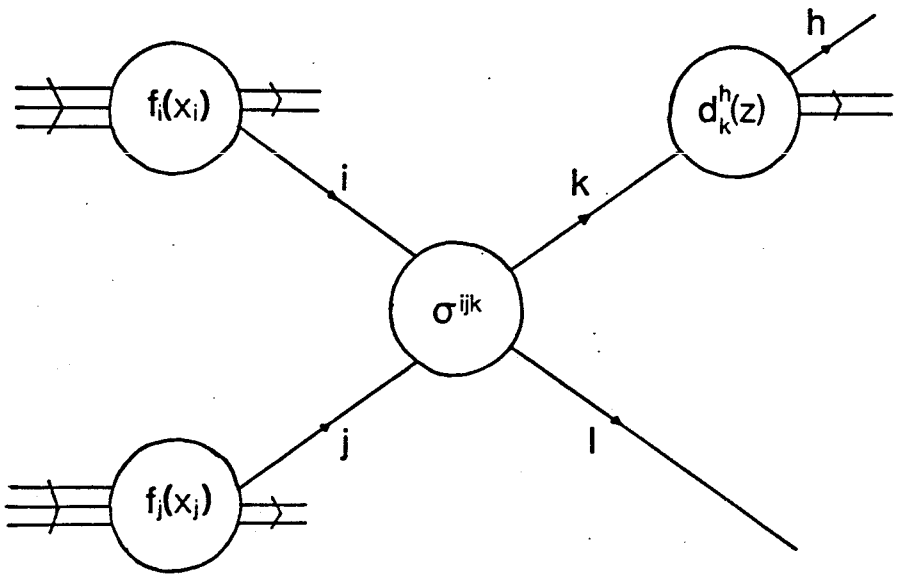

Figure 5: Schematic of Hadron Production in $p\bar{p}$ collisions

1.4.6 Hadron Production

Combining the above information one obtains the picture in figure 5. Here, two partons labelled i and j, are scattered from hadrons with cross-section, σ^{ijk}, forming partons k and l. The invariant cross-section for a parton, k, to be emitted from an interaction between a proton and anti-proton, can be written as [16]

$$E_k \, d\sigma/d^3p_k = \Sigma_{i,j} \int dx_i dx_j \, F_i(x_i) \, F_j(x_j) \, \hat{s}\pi^{-1}\delta(\hat{s}+\hat{t}+\hat{u}) \, d\sigma^{ijk}/d\hat{t} \qquad 1.4.15$$

where

- $F_i(x_i)$ is the probability of finding parton i with x_i from the proton (or anti-proton),
- $\hat{s}\pi^{-1}\delta(\hat{s}+\hat{t}+\hat{u})$ are phase space terms,
- $d\sigma^{ijk}/d\hat{t}$ is the partial cross-section for $i+j \rightarrow k+l$,
- and the sum. $\Sigma_{i,j}$ is over all partons.

In order to find the single particle inclusive cross-section, we need to fold in the probability of obtaining a hadron, h, from the parton, k, with a momentum fraction z ($p_h = zp_k$), obtaining

$$E_h d\sigma^h/d^3p_h = \Sigma_k \int z^{-2} dz \, D_k^h(z) \, E_k d\sigma^k/d^3p_k. \qquad 1.4.16$$

Which is the inclusive cross-section for particle production in $p\bar{p}$ collisions.

1.5 This Thesis

This thesis covers the details of the author's work in UA1. Chapter II is a general introduction to the apparatus and describes the parts of the detector used in the following chapters i.e. the drift chambers, calorimeters, trigger system, and a guide to the chain of programs used to order the data before any analysis can begin.

The principal design of UA1 was to observe the electrons from the decay of the IVBs, requiring the identification of electrons and any possible background from other particles produced at the previously unobserved high energies. The observation of the IVBs has also been verified by their decay to muons, proving the muon detection to be a valuable feature. The muon detection has been upgraded since the original design, and chapter III follows the creation of a new muon trigger system and the improvements it has made to the experiment. Extra chambers (Iarocci tubes) have also been incorporated into the detector, to improve the detection and resolution of muons. Chapter IV describes the preliminary work which investigated the properties of these detectors using X-rays, cosmic rays and a beam from the SPS, comparing the results with simple Monte Carlo studies.

The hybrid design of UA1 has led to a system with which it is possible to detect jets, and in chapter V the UA1 jet algorithm is used to investigate jet properties by combining information from the calorimetry and the central tracking chamber. The jet algorithm is used to look for events containing a single jet in the 1982 data. The large number of single jets is incompatible with the number expected from the standard model for this data sample, and the study is used to obtain a better understanding of the jet algorithm within the limitations of the apparatus. Then the distribution of tracks around jets is studied using different methods to measure properties associated with jet fragmentation.

In the last chapter, the muon and jet information is combined for the study of heavy quark production in proton-antiproton collisions. The large amount of data in this study required a software selection technique which was verified by scanning a substantial sample of events. The corrected differential cross-section for muon-jet events is presented and is followed by a detailed comparison with the standard model, resulting in a calculation of the inclusive cross-section for heavy flavour.

2. THE UA1 APPARATUS

The previous chapter has reviewed some of the phenomena which the UA1 detector is designed to detect and record. The experiment involves a complex array of detectors which can recognise the many types of particles produced in the collisions. The beam crossings in the SPS tunnel occur at intervals of 7.6 μs whereas data can only be written to tape at a few events per second. This means that a reliable trigger needs to be included in the data acquisition, which can give an on-line decision of the importance of an event and either reject or record the whole event. In the first three data taking runs the detector was the same as described in the original proposal [2] but before the run in autumn 1984, there was a proposal [17] for an upgrade of the existing muon detection and triggering, and the introduction of extra drift chambers, which will be described in the following chapters.

2.1 The SPS Collider

The 2.2 km diameter collider (figure 7) is used to produce proton-antiproton collisions at a point to within 0.3 m of the centre of the detector. This length corresponds to a timing of 1 nanosecond. The obvious complexity of such a machine makes any detailed description impossible here. Only the main aspects relevant to UA1 are considered.

The luminosity, $\mathscr{L}$, of a collider varies as

$$\mathscr{L} = N(p)N(\bar{p})nf/4\rho^2 \qquad 2.1.1$$

where N(p) [N($\bar{p}$)] is the number of protons [antiprotons] in n bunches which revolve around the SPS at a frequency f. The (common) particle bunch radius, ρ, is of the order 0.01 cm, and the numerical factor of one quarter takes into account the integration over the Gaussian profiles.

The design luminosity was 1 $\mu b^{-1}s^{-1}$ with six bunches of protons and antiprotons. However in the last run (autumn, 1984) the peak luminosity reached 0.5 $\mu b^{-1}s^{-1}$, with only three bunches each. Although there are 7.6 μs between beam crossings, UA1 has kept to the 3.8 μs timing for triggers for the present, because six bunch operation of the SPS may become feasible.

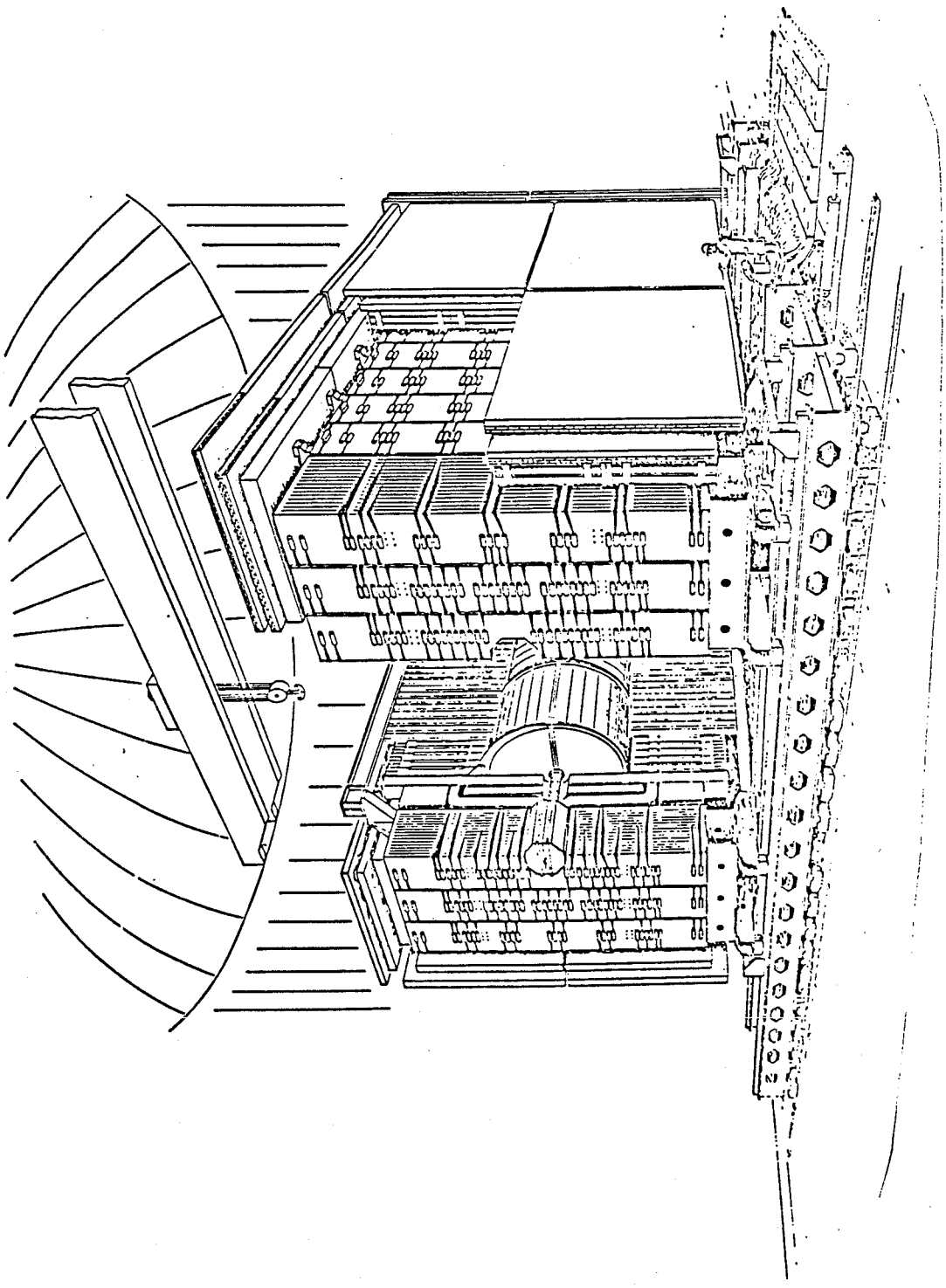

Figure 6: The UA1 Detector

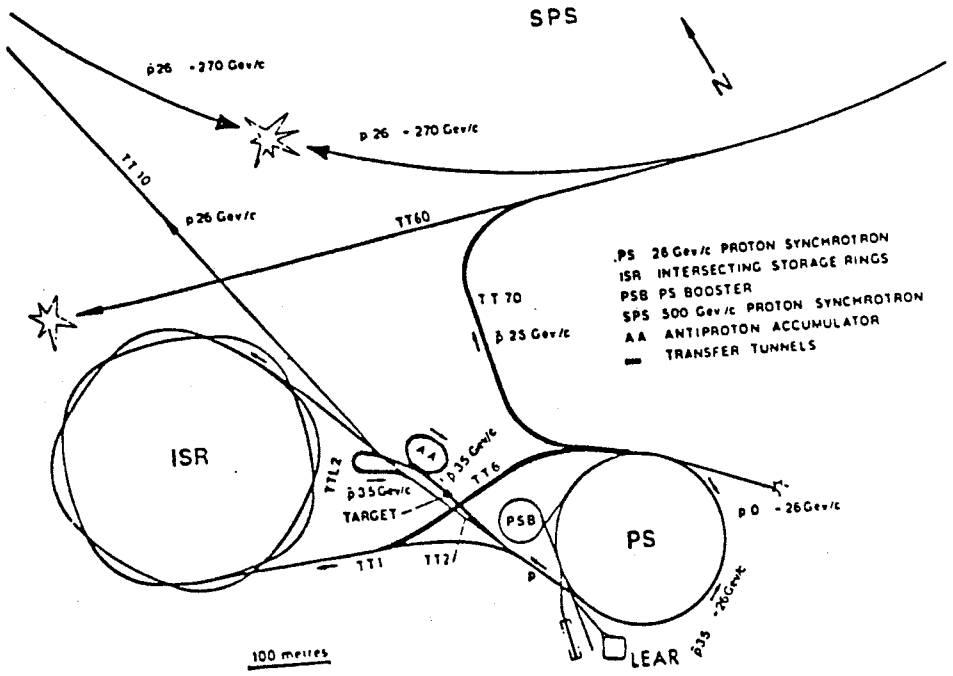

Figure 7: Overall Site Layout

Antiprotons are produced at about 3.5 GeV/c by 26 GeV/c protons from the CERN Proton Synchrotron (CPS) incident on a copper target. The target is a 3 mm diameter copper wire enclosed in a graphite and aluminium casing. The antiprotons are collected by a magnetic horn and injected into the Antiproton Accumulator where they are cooled by the process of stochastic cooling [18]. The method of cooling takes place by a process of negative feedback, the transverse and longitudinal motions of the antiprotons are detected by pick-ups positioned around the accumulator and compensating fields are applied at an odd number of quarter wavelengths of a betatron oscillation later. After an initial cooling and before the next bunch from the CPS is injected, a ferrite shutter opens and the antiprotons are moved into the stack, where further cooling takes place. The stack lies parallel to the injection ring inside the accumulator, but the two rings are separated by the mechanical shutter.

The shutter has to move quickly in a high vacuum (the transfer between the injection ring and the stack takes 400 ms), and it is this part of the AA which causes most problems in the stacking rate of antiprotons.

After the antiprotons have been stacked and cooled for a period of a day or so, they are then injected into the CPS at 3.5 GeV/c. Here they are accelerated to 26 GeV/c, and injected into the SPS. There they join an equal number of bunches of protons from the CPS, and together the bunches are accelerated to the final momentum of 273 or 315 GeV/c. The beams are kept as long as possible, but the luminosity falls with a half life of the order of 10 hours due to the particle interactions within the bunches and with residual gas in the vacuum pipe.

2.2 The Central Detector

The central detector is a drift chamber with electronic image readout. It records the drifting electrons caused by the ionisation of a gas due to the charged tracks emanating from a collision. The chamber sits inside a uniform dipole magnetic field of 0.7 Tesla and so from the curvature of each track a momentum can be measured, as well as its initial direction. The chamber is a cylinder of diameter 2.2 m and length 6 m. It is split into six semi-cylindrical segments, two in the middle named the central chambers and two pairs either side named forward chambers. The shell of the chamber is constructed from a honeycomb structure of vetronite strengthened with bars of Stesalit. It is prestressed in order to account for the deformation by the tension of the wires. By this method an accuracy of 0.5 mm can be obtained with a rigid structure containing a minimum of radiation lengths of material. The wires are parallel to the magnetic field and are strung in groups of three planes, two anode planes and a cathode plane. The electric field is 1.5 kV/cm and is kept uniform by a racetrack around the inside of the shell. The racetrack is a series of printed circuit strips which are connected to a chain of resistors acting as voltage dividers, this keeps the field uniform to better than one part in a hundred.

Electrons produced by an ionising track drift across to the anode wires, avalanching in the strong electric field. The maximum drift time in the argon-ethane mixture is 3.6 μs which is smaller than the

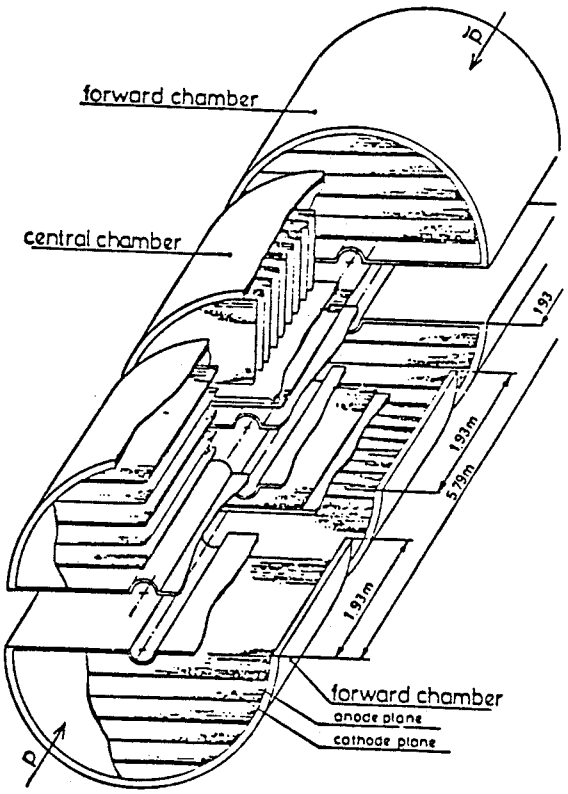

Figure 8: The Central Drift Chamber

proposed 3.8 μs between beam crossings. The anode sense wires are strobed after every 32 ns and the charge measured. There are three readings made at each end of the wire, two are by Fast Analogue to Digital Converters (FADC) and another by a Time to Digital Converter (TDC). The FADC's are of different types, one has a linear response and is used to calculate the coordinate along the wire by charge division, and the other is logarithmic in response and is used to measure total charge deposition on the wire for a calculation of dE/dx. Figure 9 [19] shows the measured dE/dx distribution for tracks in the central detector, there is clear separation at low momentum, followed by the relativistic rise.

The TDC measures the time of arrival of the charge within the 32 ns window. Every 32 ns eight bits of information are written onto a 256 byte RAM, overwriting the oldest byte of information. In this way 8.2 μs of information is stored on each chip, and can be read out if the trigger gives a decision to record an event.

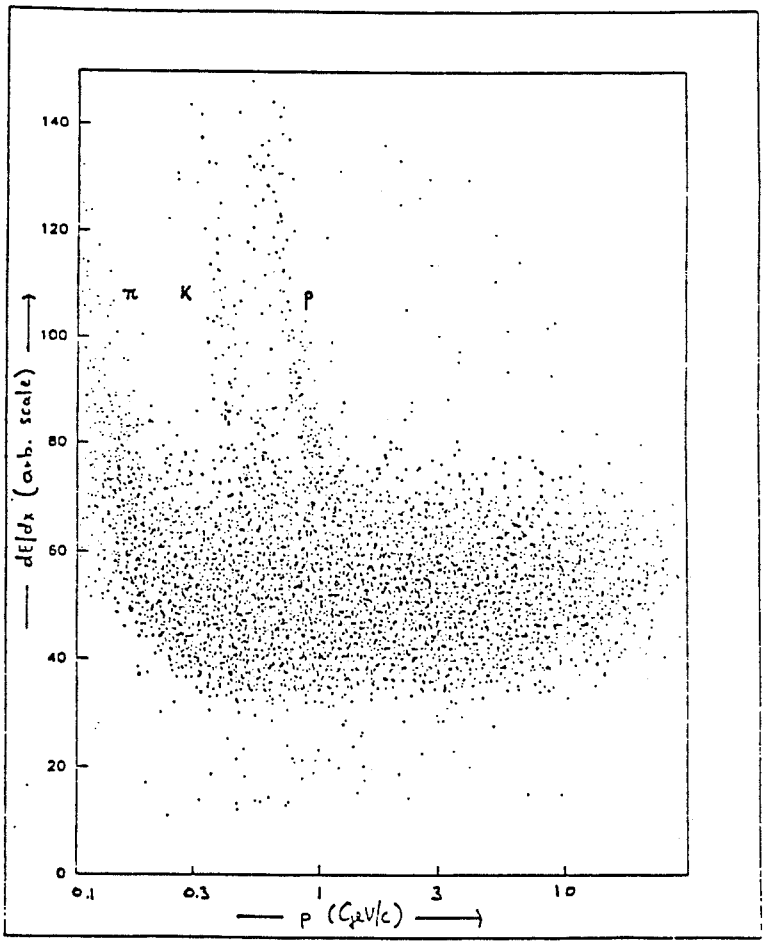

Figure 9: Data showing separation of particle type by dE/dx

The resolution of the chamber is summarised in table 4. For high momentum tracks the resolution is dominated by the measurement error in the track sagitta, for a 1 m track it is approximately

$$\Delta p/p = 0.005p \quad \text{where p is in GeV/c.} \qquad 2.2.1$$

Table 4: Resolution of the central detector

0.1-0.3 mm	along drift direction
20.0 mm	along wire
5.0 mm	in planes of wires perpendicular to wire length

2.3 The Electromagnetic Calorimeter

The electromagnetic calorimeter is designed to measure the energy of electrons and photons created in beam collisions. The calorimeter is made of sheets of lead and scintillator; photons convert to electron-positron pairs in the lead which in turn bremsstrahlung in the high electric field around the lead nuclei. This process produces a shower of photons and electrons crossing the sheets of scintillator. The shower develops as the number of particles increases but then falls off when the mean photon energy falls below the threshold for pair production; subsequently the photons become absorbed by the atomic photo-effect. The typical depth for a shower profile is 20 radiation lengths. The light produced in the scintillator is proportional to the energy of the shower and is converted to an electric current and amplified by photomultipliers (PM's). The PM's must be placed outside the dipole field of the UA1 magnet and due to the limited space conventional light guides cannot be used. Instead the light is transferred by wavelength-shifter bars of acrylic doped with BBQ. The light from the scintillator is absorbed at a wavelength of 420 nm by the BBQ and reemitted above 480 nm, travelling along the bars by internal reflection to the conventional light guides which terminate at the PM's.

The calorimeter is divided into two types; the gondolas covering a polar angle from the beam axis between 90 degrees and 25 degrees and the bouchons covering the angle between 25 degrees and 5 degrees. The gondolas are divided into 48 half annular segments of a lead, scintillator sandwich 26.4 radiation lengths deep. There are 74 pairs of layers of 2 mm sheets of lead and 2 mm Plexipop, and the

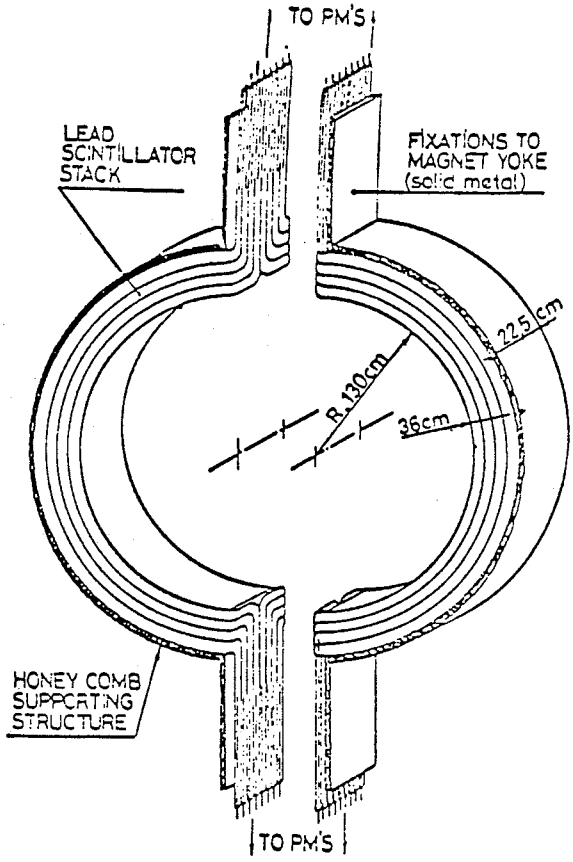

Figure 10: Central Electromagnetic Calorimeter

light is read out from the four corners of the scintillator sheets. The light collected from each corner of the scintillator sheets is summed into four samplings in depth, at intervals of 3.3, 6.6, 9.9 and 6.6 radiation lengths, so that a total of 16 measurements are made per gondola.

The bouchons are divided into 32 radial segments (petals) around the beam line and each petal in depth is a sandwich of 4 mm lead sheets and 6 mm scintillator. Again it is sampled in depth, after intervals of 3.6, 7.2, 8.7 and 7.2 radiation lengths, and the readout is along the outer edge of the petal. In order to reconstruct the shower position and energy a further measurement is made by a position detector placed inbetween the second and third samplings. It consists of a pair of orthogonal planes of proportional tubes. In each quadrant of the bouchons there are 140 horizontal tubes, 1.4 m long and 85 vertical tubes, 3 m in length. The position of a shower is measured by charge division along the

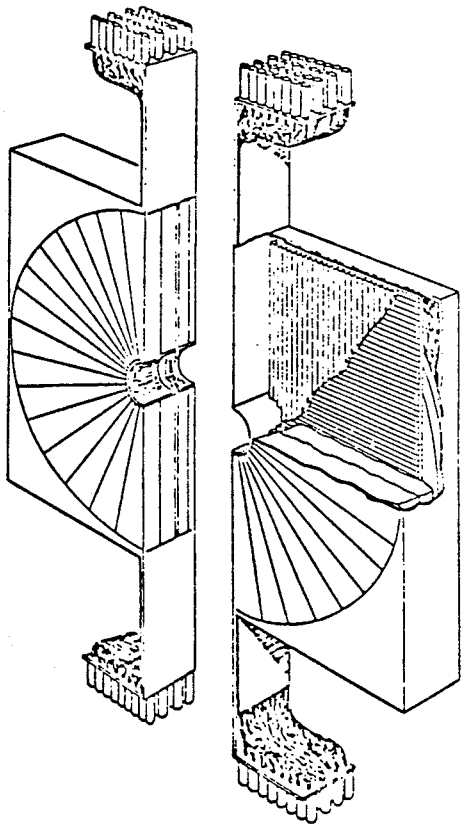

Figure 11: Bouchons and Position Detector

wire, and to resolve ambiguities an estimate of the energy is made from the total charge deposited. The energy resolution of the tubes is

$$\Delta E/E = 170\%/\sqrt{E} \qquad (E \text{ in GeV}), \qquad 2.3.1$$

and the space resolution varies from 1cm at 5 GeV to 0.3 cm at 92 GeV.

In lead, one radiation length is equal to 0.03 hadron absorption lengths and so hadrons can also give rise to showers in the calorimeter. The electrons and photons convert more quickly and one can distinguish between hadrons and electrons by the shower profile in the samplings. By using simple cuts on the profile one can reduce the hadronic background for electromagnetic recognition, for 40 GeV depositions these cuts impose no loss of signal, and at 15 GeV the detection efficiency is around 60%.

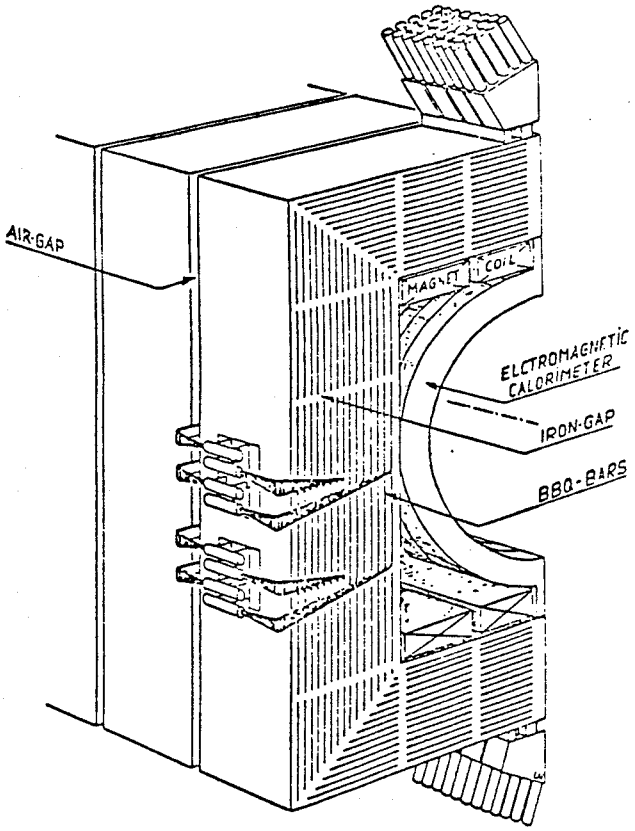

Figure 12: Hadron Calorimeter

Before and after the runs energy resolution is calibrated by beam line tests and irradiation by a 7 Curie Co^{60} source. During the run, it is monitored by laser beams fed to the photomultipliers by optical fibres and cross calibrated with an Am^{241} source. The energy resolution is

$$\Delta E/E = 15\%/\sqrt{E} \qquad (E \text{ in GeV}) \qquad 2.3.2$$

for the gondolas, and

$$\Delta E/E = 20\%/\sqrt{E} \qquad (E \text{ in GeV}) \qquad 2.3.3$$

for the bouchons.

2.4 The Hadron Calorimeter

Behind the electromagnetic calorimeter is the iron return yoke of the dipole magnet which has been calorimeterised by inserting 1cm sheets of plastic scintillator between the 5 cm sheets of iron. This creates a calorimeter which records the energy deposited by hadrons which may have started to cascade in the gondolas. The central part is named the C's and covers the region between 90 and 25 degrees in polar angle (θ). The end-cap calorimetry is similar in construction and covers the polar angle down to 5 degrees around the beam pipe. The readout system is similar to the electromagnetic calorimeter with BBQ readout, but there are only two samplings in depth, and the position resolution is determined by the dimensions of the cell (0.9 m x 0.8 m in the C's; 0.9 m x 0.9 m for $\theta > 15$ degrees and 0.5 m x 0.4 m for $\theta < 15$ degrees in the I's). The energy resolution is

$$\Delta E/E = 80\%/\sqrt{E} \qquad (E \text{ in GeV}). \tag{2.4.1}$$

The nine interaction lengths of material reduces the punch through of hadrons with a transverse energy greater than 10 GeV to below 0.6%. The important features of the hadron calorimeter are that it is used to measure the hadronic component of the energy in jets and it also completes the energy collection in an event so that it is possible to reconstruct a transverse missing energy vector. This vector is derived by converting energy depositions in individual cells into an energy flow vector, $\mathbf{E_i} = \mathbf{n_i}E_i$, where $\mathbf{n_i}$ is the unit vector pointing to the centre of the cell. For relativistic particles and a calorimeter with a perfect response, $\Sigma \mathbf{E_i} = 0$, provided no noninteracting particle is emitted. If noninteracting particles (such as neutrinos) are present, their momentum, $\mathbf{p}_\nu$, is defined by $\mathbf{p}_\nu = -\Sigma \mathbf{E_i}$. Due to the conditions imposed by the collider, it is impossible to measure the component of the missing energy vector along the beam direction and the vector is used only in the two dimensions perpendicular to the beam axis. The resolution of the transverse missing energy vector is measured from minimum bias events, it has a Gaussian shape with a width of $0.4/\sqrt{\Sigma|\mathbf{E_i}|}$, whilst in events with jet triggers this width increases to $0.7/\sqrt{\Sigma|\mathbf{E_i}|}$.

The hadron calorimeter is also used in rejecting cosmic rays in the muon trigger, a check is made for a minimum ionising energy signal in the calorimeter cell between the muon track and the vertex (chapter III).

Each module of the calorimeter was calibrated originally with cosmic and accelerator muons, and with radioactive sources (200 microcurie Ru^{106}). After installation the response of the calorimeter was calibrated with the laser and optical fibre system. There are two nitrogen lasers which pulse light to each scintillator plate, and the response of the PM's are compared to the signals from radioactive sources attached to reference PM's and scintillators situated underneath the experiment which are also fed by the lasers. All subsequent variations in response are monitored using the laser system and accessible stacks are checked for absolute response with sources and cosmic rays. Full details of the installation and monitoring can be found in [20].

2.5 The Muon Chambers

Outside the return yoke of the dipole magnet lie 60 cm of iron hadron absorber, and beyond this stand the muon chambers. There are 34 large drift chambers, covering a total area of 500 m^2 consisting of four pairs of crossed planes, defining two points in space (figure 13). Adjacent planes are needed to resolve a left-right ambiguity as well as eliminating the problem of dead space between chambers. The large distance of 62 cm between the two sets give a long lever-arm which can be used to measure the projected angle of a track back to the vertex, to within 3 mrad at 40 GeV/c. The momentum of the muon is measured from the magnetic curvature of the track in the central detector. This measurement can be improved for hard tracks by using the bending through the magnetic field in the iron yoke, which has been tested for cosmic rays which travel through the detector. The cosmic muon is tracked through the top or side chambers, through the CD and out the other side through another layer of muon chambers. Two momenta are reconstructed, one from the track in the CD and another from the four hits in the muon chambers. After allowances for the energy loss in the iron for a minimum ionising particle, the measured momenta are found to agree to within

$$\Delta p/p = 20\% \,. \qquad 2.5.1$$

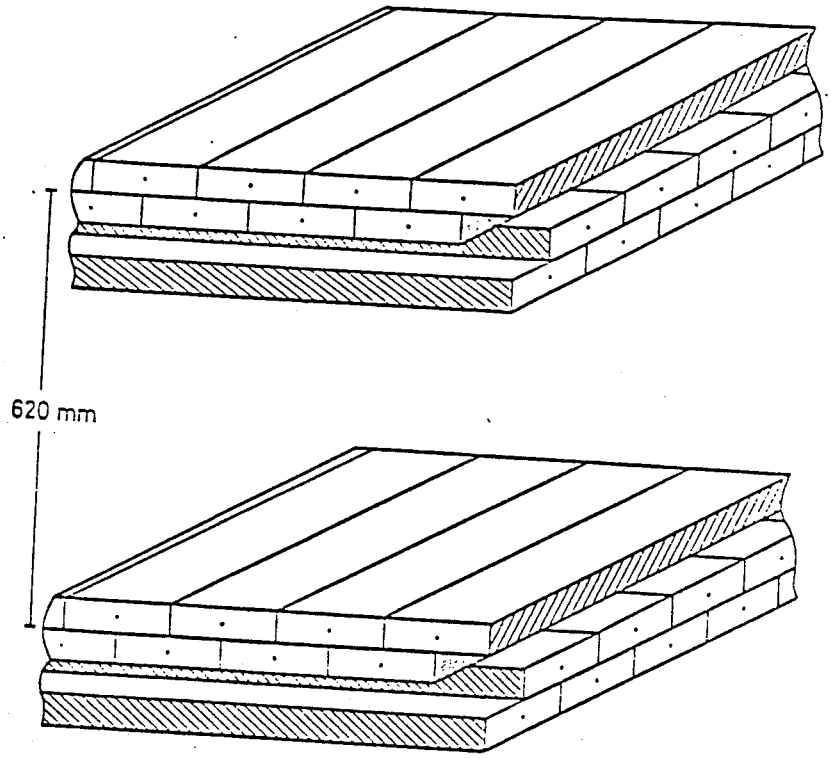

Figure 13: Muon Drift Chambers

The chambers do not cover all of the 4π steradians around the interaction region. If muons are emitted isotropically only 58% are recorded within a rapidity range of $+1.1$ to -1.1. Folding in the distribution arising from a muonic decay of a W boson the W detection efficiency drops to 48%.

The muon trigger is a hard wired processor which compares the hits patterns on the tubes with a set of look-up tables. It selects tracks in the muon chambers which point back to the vertex to within

$$150 \text{ mrad.sin } \theta \qquad 2.5.2$$

where θ is the polar angle from the beam. This algorithm is only valid for hard tracks and the trigger does not become fully efficient until 5 GeV/c. There is also a cut of 1.9 sinθ GeV/c in momentum

which is the energy deposition of a minimum ionising particle traversing the thickness of the nine interaction lengths of iron. In order to be fast, the trigger does not use the drift time information and can reach a decision 1.2 μs after the maximum drift time (1.4 μs).

2.6 The First Level Trigger

The interaction rate for a luminosity of 0.1 $\mu b^{-1}s^{-1}$ is approximately 5 kHz, and the UA1 trigger was designed to reduce this rate by three orders of magnitude to less than the 5 Hz imposed by the speed of the tape drives which record the 120 kbyte events onto tape. In UA1 there are two independent trigger processors, the calorimeter processor and the muon trigger processor. Both are hardwired processors with some level of flexibility due to the inclusion of look up tables stored in Random Access Memory. These are loaded before each shot and can be changed in a matter of minutes to suit beam conditions. The signals from each processor can be taken as separate triggers, or can be combined in the Final Level Trigger Logic to produce trigger combinations such as muon·jet or muon·electron type events. The trigger reaches a decision before the next crossing and so is described as 'dead-time free'. However the reading out of an event from the Data Acquisition System once a trigger has been given incurs a dead-time. This dead-time is normally a few percent during a physics run and is kept below 10% (at all luminosities), but it rises rapidly and non-linearly as a function of luminosity and event length as soon as the event rate reaches the maximum tape writing speed. The slowest part of the readout in 1983 was the central detector which incurred a dead-time of 35 ms to read out all of the digitisings from the 6200 wires. In 1984, the data were doubled buffered, so that two events could be stored at any one time, this decreased the dead-time to 3 ms. The next slowest part is the drift tubes in the bouchon calorimeter which may be buffered before the next run.

The muon trigger will be discussed in the next chapter, and here a summary of the central trigger processor will be given, an excellent description of the building, installation and testing of the trigger can be found in [21]. The trigger can be divided into three stages:

1. Pretrigger, to provide a proton-antiproton interaction trigger, which discriminates against collisions from beam-gas interaction, halo particles near the beam and cosmic rays. This reduces the 130 kHz beam crossing rate to around 3.5 kHz at a luminosity of 0.1 $\mu b^{-1}s^{-1}$, with an efficiency of 96$\pm$2%, for all non-diffractive inelastic interactions using signals from;

    a. the SPS to indicate the timing of the beam crossings

    b. hodoscopes at distances 11m, 6.25 m and 3.8 m either side of the interaction region.

2. Calorimeter Processor, which takes signals from the 2440 PM's on the calorimeter and groups them into 288 trigger channels, digitising the signals with eight bit precision. The signals are converted either to energy or transverse energy with the aid of look up tables stored in RAM. The tables take account of pedestal subtraction and the azimuthal angle of the cell clusters to calculate the transverse energy. The energies are grouped in the following ways;

    a. jet trigger using four electromagnetic and four adjacent hadronic cells;

    b. electron trigger using adjacent pairs of e.m. channels;

    c. electron pair trigger using two adjacent pairs of e.m. channels with a lower threshold than in (b);

    d. total transverse energy trigger where a scalar sum of the individual channels is made;

    e. E_t imbalance trigger (introduced in 1984 run), finding the energy difference in the calorimetry between positive and negative z.

3. Final Level Trigger Logic, where the signals from the two processors are combined and a decision reached as to whether the event should go on for further processing or not. Here the event rate has been reduced to around 2 events per second at 0.1 $\mu b^{-1}s^{-1}$, depending on the constants stored in RAMs in the central trigger processor.

Apart from the calorimeter and muon triggers, a small fraction of cosmic ray and pion triggers are taken for chamber alignment and for background studies for electron identification. The cosmics are triggered by a coincidence between scintillators placed on the top and on the sides of the UA1 magnet, and the calorimeters in the bottom. The pions are triggered by isolated hits in the front stacks of the hadron calorimeter.

2.7 The 168 Emulator Trigger

The 168E is similar to the IBM 168 central processing unit and is programmed by down line loading a compiled module from an IBM computer. Four parallel 168 emulators were used on line in 1983 to monitor the events and extract special events of interest such as good W or Z candidates, which are recognised by large electromagnetic depositions with a pointing track in the central drift chamber. The 168Es are used after the final level logic and so have enough time to access the CD information to construct tracks, hence it is possible to reduce the trigger rate by an order of magnitude. The 168Es act as entirely software triggers, they are extremely flexible but scrupulous and refined monitoring is needed to check the coding. An extra emulator was used to spy on the system, selecting events online to check rejection factors and energy distributions of events. From the data of the 1983 run, where all events flagged by the emulators were also recorded on normal tape, one can calculate the efficiency of the emulators against malfunction. It was found [22] that of the 2,420,000 events written to 2200 tapes, 500 events spread over six of the raw data tapes had errors due to failures in the emulators. This is an error occurrence of one for every 0.27% tapes, or 0.021% events written to tape, but no significant bias was found in any important channel.

Table 5: Triggers in the 168E for 1984

Electron (350 ms)
Calorimeter cell energy reconstruction, identification of electrons above some E_t threshold cut (8-10 GeV), isolation check in space and in the hadron calorimeter energy deposition.

Jet (350 + 40 ms)
Jet identification using a UA1 type algorithm on the calorimetry.

Transverse energy (350 ms)
Total transverse energy calculation from cell energy list.

Missing energy (350 ms)
Total transverse vector energy imbalance.

Background (350 + 10 ms)
'Pion' identification by threshold cut (8 GeV E_t) in the hadronic energy, and isolation in the electromagnetic cell nearby.

Muon (10 + 150 ms)
Muon track reconstruction in the muon chamber, and a track in a road in the central detector between the hit in the muon chambers and vertex.

As the luminosity increases the thresholds on the calorimetry trigger are increased, and the acceptance of the muon trigger decreased, but above $0.2\,\mu b^{-1}s^{-1}$, these thresholds became unacceptable and so in 1984 five 168Es were used in an active role to reject events from the two hardwired processors. Figure 14 shows the layout of the emulator system in 1984 which was used to actively reject events.

With an input rate of 10 Hz from the trigger processor, each emulator had 500 ms to analyse events in parallel using a program which looked for the six types of trigger listed in table 5. In the 1984 run this second level trigger rejected around 60% of events, and diverted 10% of the remaining events onto the special tape for express line analysis.

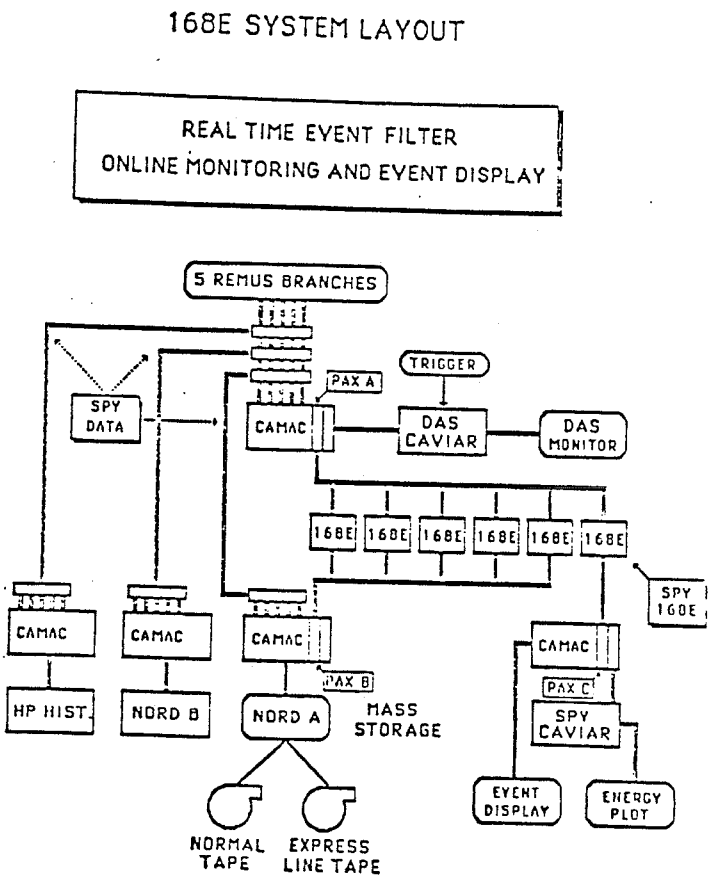

Figure 14: 168E system Layout

2.8 Data Processing Chain

UA1 has many unique features, one of which is the large amount of data stored in the vaults at CERN. The data written to tape during the runs is processed through several stages, and there follows a brief outline of this complex processing chain which is relevant to the analysis in this thesis.

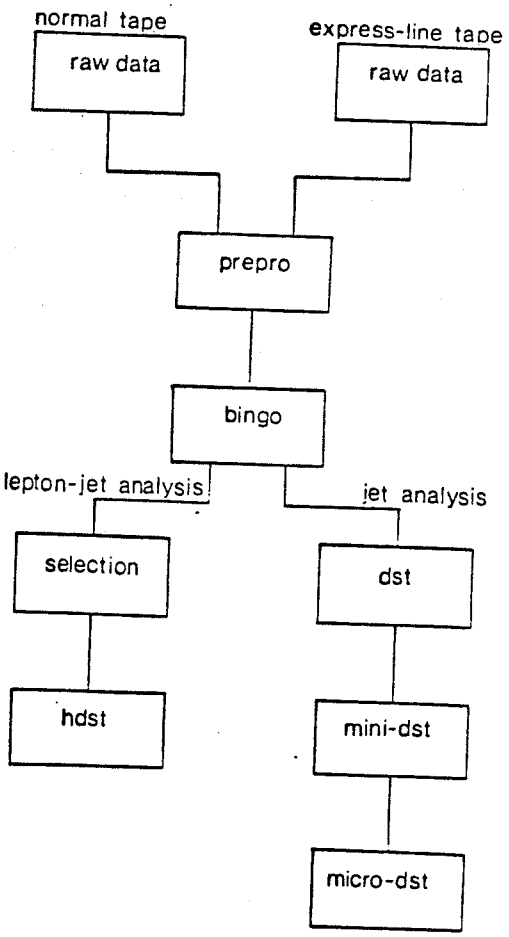

Figure 15: Data Processing Chain

During the run the Raw Data is written onto two separate streams, normal tapes and express line tapes. The express line data set contains a copy of the events with special triggers selected by the 168Es and is processed immediately during the run. This makes it possible to access interesting events, such as W's, Z's or missing energy events, for preliminary investigation. Care is taken to avoid the duplication of processing of the express line data by the inclusion of a bit in each event to indicate whether it is in the express line data sample or only in the normal sample. The processing of the express line data also helps check the apparatus and can identify problems in the experiment within 24 hours of data being written. The first processing program (PREPRO) has three main functions;

1. it orders the data into HYDRA [23] format, a CERN memory management system;

2. removes pedestals and applies calibration constants in the calorimetry and for the central detector drift time measurements;

3. removes the unnecessary zeroes from data channels which have not detected particles in the event.

At this stage of processing, there are around 1,000 events on a standard 6250 b.p.i. tape.

Next is the BINGO stage which essentially reconstructs the tracks through the whole detector. Final calibration of the measurements are applied and track finding in the drift chambers is performed. BINGO also looks for correlations between the parts of the detector, such as tracks pointing to the calorimeter depositions and muon tracks. This stage is CPU intensive, taking around 15 CPU seconds per event (IBM 168 units), and so only selections of events reach this stage, such as express data, or those flagged by programs which recognise special events at the PREPRO stage on the normal tapes. The extra information of the tracks also means an increase in event length, reducing the number of events per tape to around 500. The events can now be scanned on the MEGATEK facility, which is described below in chapter V. BINGO is usually followed by SELECTION, which adds results from lepton identification, jet reconstruction, and calculations of the missing energy in events.

Data analysis requires the study of predefined features of the data, and many computer jobs can be submitted which differ only in the investigation of certain quantities. It is also clear that it is difficult for laboratories outside CERN to import large numbers of tapes to participate in the UA1 processing and analysis. These reasons have lead to several further processing levels, where data not wanted are removed, and results of lepton or jet identification packages added. For jet analysis (chapter V) a special package was developed [24] to study large amounts of data, concatenating the data to 6000 events per tape on DST's. In order to reduce the numbers of tapes still further, mini-DST's and even micro-DST's were created for the 1982 and 1983 runs. These tapes contain the results of the UA1 jet algorithm, and remove some track information, saving CPU time and numbers of tapes. Lepton identification requires access to information at the BINGO level and as a result a different type of tape was created. These are known as HYDRA data summary tapes (HDST's) and can contain around 4000 events per tape.

The processing programs form the bulk of the 250,000 lines of FORTRAN written by members of UA1, and a large fraction of the CPU time available on the CERN computers. As the data increases from each run, attempts have been made to speed up the processing chain and explore new computing systems, however details of these are beyond the scope of this thesis.

3. THE FIRST LEVEL MUON TRIGGER

The UA1 trigger was discussed in general in chapter II. The fundamental problem which it was designed to solve is to select the most important events from the beam crossings which occur at a rate of 130 kHz. It accomplishes this by taking events which are of special interest, characterised by large energy depositions in the calorimetry or lepton signatures. Of all the known leptons, the muons leave perhaps the most unambiguous signature, as the other charged leptons can be faked by combinations of neutral and charged pions, and the neutral leptons (neutrinos) leave only a missing energy vector which is difficult to find reliably within the short time available for triggering. In the final analysis the signature of the muon as seen by the detector is as follows;

1. a track in the outer drift chambers, pointing back to the vertex;

2. a small ($\approx$0.8 GeV) energy deposition in any hadronic calorimeter cell backstacks between the muon track and vertex;

3. and a track in the central drift chamber.

This information is used in the first and second level triggers. Points (1) and (2) are used in the first level trigger, which gave one million triggers out of the 2.5 million events recorded on tape during the 1983 run [25]. All triggered events are passed to the second level trigger in the 168 emulators (described in chapter II), where tracks are reconstructed in the muon drift tubes on-line, to create external points. From each external point a road is taken in the central drift chamber to the origin (figure 16) and the tracks reconstructed inside the road. The event is selected if a track is reconstructed which passes close to the origin with a momentum greater than approximately 3 GeV/c. This chapter describes the first level trigger which is required to be reliable and to give no deadtime.

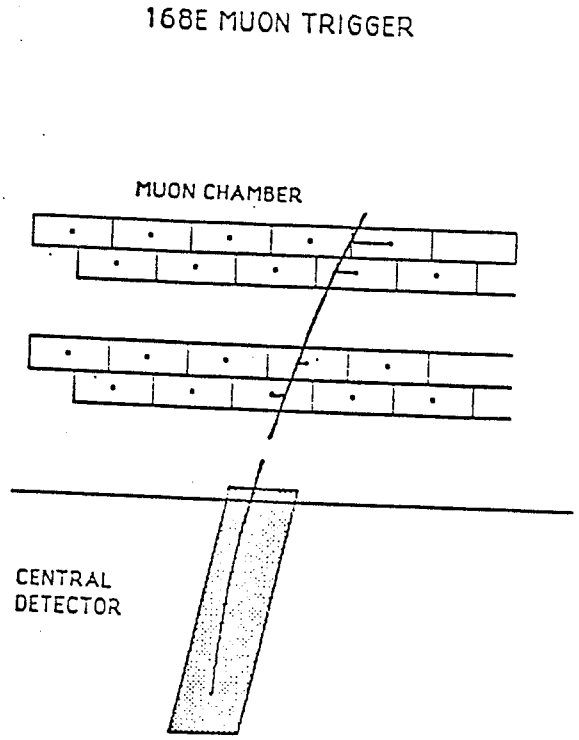

Figure 16: 168E muon trigger

3.1 The Trigger Hardware

The first level muon trigger searches for tracks in the two projections in the plane of the chamber, and then looks at the signals in the hadron calorimeter cells in line between the track in the muon chamber and the vertex. The muon chambers are situated outside the calorimetry and iron as shown in figure 17 (where the top and bottom chambers have been excluded for clarity), and are constructed from drift tubes 15 cm wide, containing a central anode wire at 3 kV and two field shaping cathodes at -5 kV and -7 kV. There are 5832 such tubes which the trigger uses to construct tracks.

The tubes are grouped into 1540 units of ten tubes across the four layers, each unit overlapping with its neighbour (figure 18). The signals of hit or no-hit are treated as binary digits, and each unit of

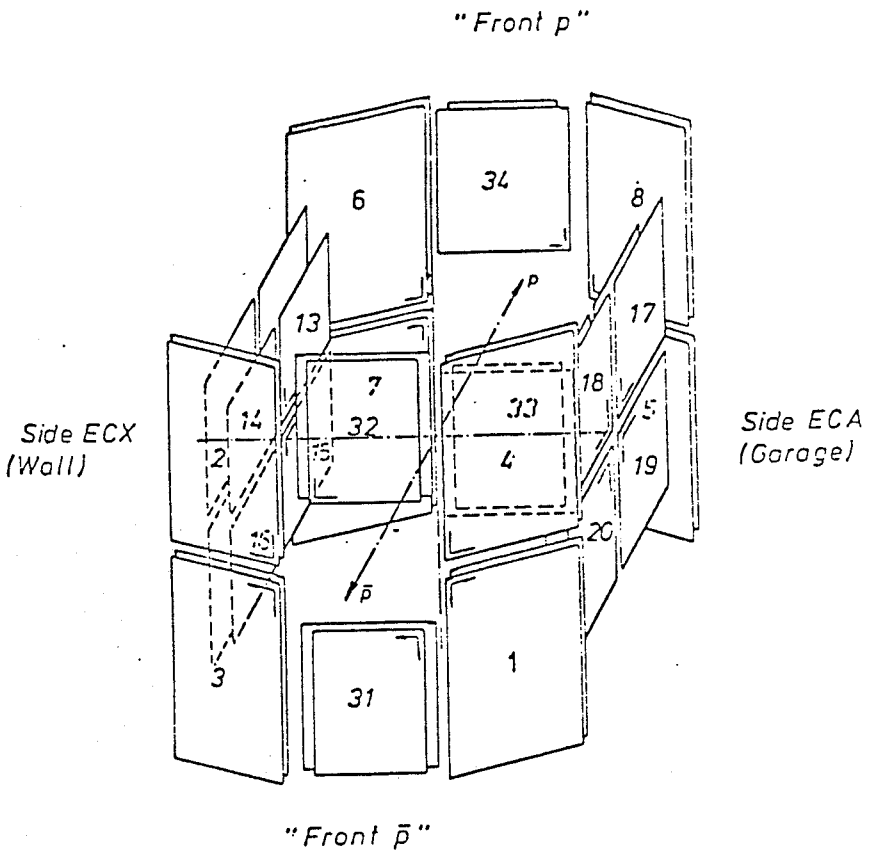

Figure 17: Perspective view of the Muon Chambers

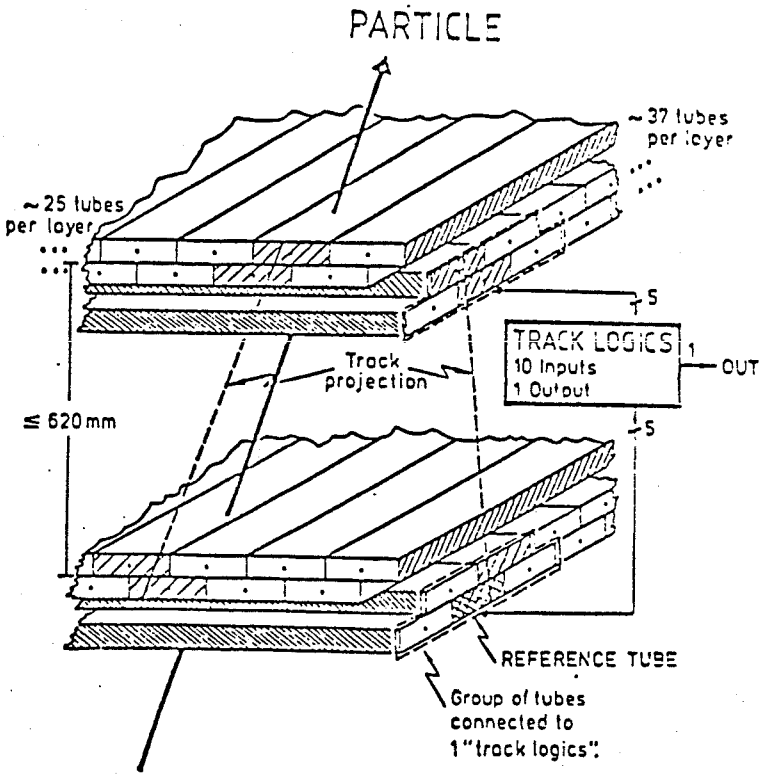

Figure 18: Trigger module

ten tubes produces a binary number between 0 and 1023. This number is used as an address to a look-up table held in RAM, there are 1540 such 1 kbit rams, one for each of the trigger units. If the memory location contains a 1 then the result is no track found, a 0 represents a track in that projection.

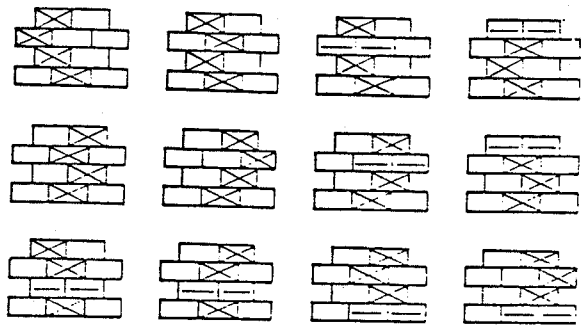

Figure 19: Examples of tracks accepted by the trigger

Examples of the tracks accepted by one type of filling in the 1 kbit RAMS are shown in figure 19. The twelve sketches show the ten tubes in the projection along the wire. An empty tube signifies no requirement for the trigger, a cross is a required hit, and a dash is a required 'no hit'. Due to the dead zones between tubes (6.7% of the tube width) one has to accept tracks which hit only three planes of tubes, requiring that there be no hit in two adjacent tubes in the fourth layer.

The memory fillings are loaded by program, and the angular acceptance can be changed to suit the luminosity of the run. During the 1984 run there were five possible trigger fillings ready for loading. Although there are over 1500 memory chips in the trigger, due to the symmetry of the experiment and the angular coverage of the 15 cm tubes, only sixty distinct fillings have to be generated, but there is still the requirement of addressing the correct chip with its filling.

The trigger combines the possible tracks in each projection to find candidate space tracks, this is done in hardwired logic circuits which is fast, but difficult to change. During the 2 μs proceeding the

beam crossing, the 396 signals from the backstacks of the hadron calorimeter cells are discriminated and passed to the muon trigger via the hadron calorimeter junction box. The discriminators consist of LeCroy QT100C hybrid circuits which digitise the signals and compare them with a threshold stored in RAM, which is typically of the order of a few counts. The candidate muon tracks are put in coincidence with the signals from any cells between the track and the vertex. Again the geometry of the experiment is 'hardwired' into the junction box, requiring substantial checking of the lines by hardware and software.

Beneath the dipole magnet the space limits the muon chambers to a single projection. The other coordinate is measured by the time difference between the signal arriving at the ends of the wire; the trigger does not have access to this information and so only one projection is used for a muon track candidate.

This completes the basic description of the hardware trigger. The trigger also produces more information than just 'hit' or 'no-hit', there is also a dimuon trigger bit, as well as information about the status of the electronic components such as which cards are on, status of power supplies, type of trigger in use etc.. This information is written to tape, so that jobs can be run to check the hardware within a few hours of data being written. This data is also monitored by M6800 microprocessors which give in real-time an indication of any problems to the physicists during operation. During the runs it was found that the most sensitive quantities to monitor were the rates from individual trigger units. These rates are compared with those from previous shots and are used to show symptoms of noisy or dead channels.

3.2 Trigger Efficiency in 1983

For the selection of W candidates in the 1983 run all of the events recorded on tape were analysed to find muons above 5 GeV/c in the central chambers, irrespective of the presence of a muon trigger. This sample was used to find the efficiency of the trigger [26]. The selection was as follows (χ^2's are defined in Appendix A):

1. P_t of the muon greater than 5 GeV/c.

2. A $\chi^2_{\mu-CD}$ of less than 15 for the difference in angle and position between the track in the muon chamber and the extrapolation of the track in the central drift chamber.

3. Quality cuts on the track in the central drift chamber; namely length in the xy plane > 40 cm, and $f(\chi^2_{xy}) < 6$ and $\chi^2_Z/N < 9$ respectively.

4. The track in the muon chamber must be in either the top, side or bottom chambers.

This sample produced the first evidence of the muonic decay of a W boson on mass-shell [25]. To obtain an unbiased estimate of the muon trigger efficiency, events were selected which had another trigger (jet, electron or a large total transverse energy). This sample contained 616 events which should have fired the trigger. We define the trigger efficiency, ε, as

$$\varepsilon = \frac{N_\mu}{N_\mu + \bar{N}_\mu} \qquad 3.2.1$$

where N_μ are identified muons with a muon trigger and $\bar{N}_\mu$ are the muons without a muon trigger. This efficiency is only for tracks which are found later in the processing chain, it does not include the inefficiencies from dead chambers. The global efficiency for the trigger was found to be $60 \pm 2\%$ (statistical errors). Table 6 summarises the efficiency of the trigger by module and for ranges of muon transverse momentum.

The efficiencies are lower than one would expect, and are independent of momentum. The efficiency is worst for the bottom chambers (21-24 and 26-29). These chambers are only five tubes wide and are placed between the rails on which the UA1 experiment moves from the experimental area to the garage (figure 20).

The energies in the hadron calorimeter cells crossed by the muons were also investigated. 5.7% of the events with a muon trigger had no energy deposition in the calorimeter cell which was crossed by the muon, but for the events with no muon trigger bit, 13.3% of the muons had no energy deposition.

Table 6: Efficiency of the trigger in 1983 run

area	chambers	efficiency (%)	statistical error (%)
TOP	9-12	56	3
SIDE	13-20	54	5
BOTTOM	25,30	86	3
BOTTOM	21-24,26-29	17	4

P_t (GeV/c)	efficiency (%)	statistical error (%)
> 5	60	2
> 10	66	5
> 15	58	9
> 20	57	10

This indicated either a problem in the hadron calorimeter junction box or that the wrong cells were being taken in coincidence with the trigger units. A useful variable proved to be $\sin\theta$, where θ is the angle between the beam axis and the line joining the muon track to the vertex. In figure 21 the efficiency can be seen to be roughly linear with $\sin\theta$, indicating that there is an underestimate of the size of the cone at large $\sin\theta$.

We also looked at the distribution of the efficiency over the length of the collider run, but no time variation of the efficiency was found. Whatever was going wrong persisted throughout the whole of the 1983 data taking period.

Some time after this work, and after a detailed investigation into the trigger, each of these problems were understood and corrected. The problems with the small bottom chambers were found to be an error in the cabling of the chambers in the area, which had existed since installation. The

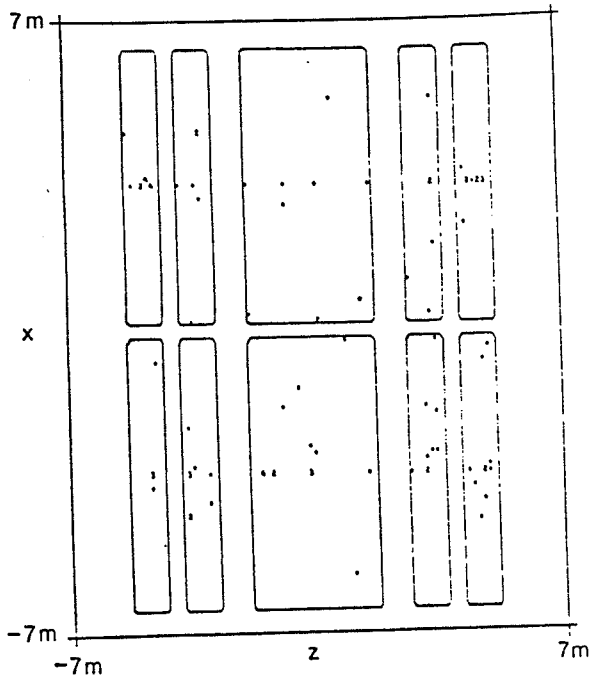

Figure 20: Positions of tracks with no trigger in the bottom chamber

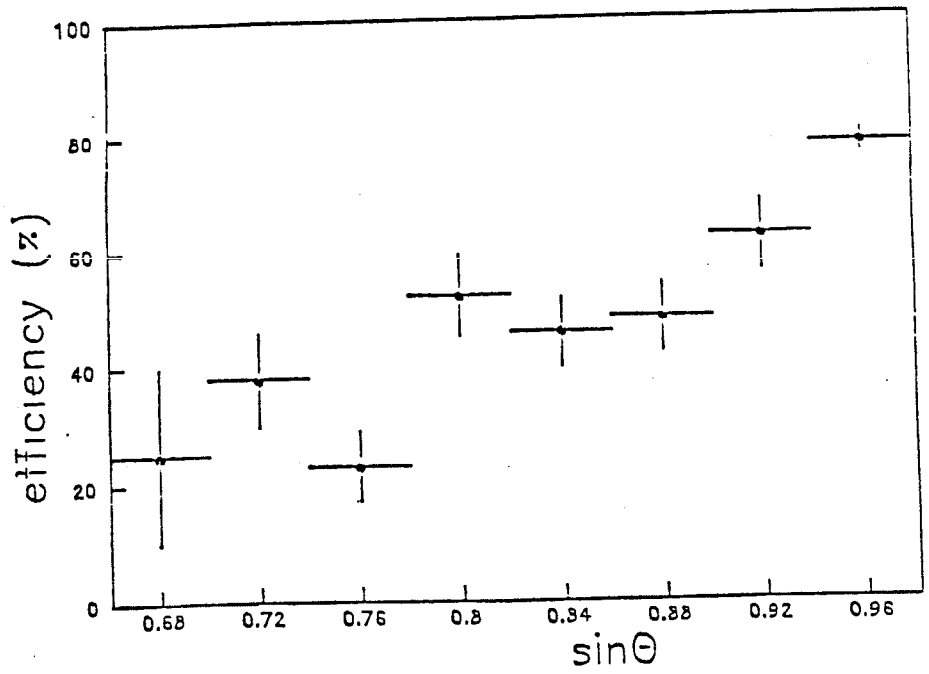

Figure 21: Efficiency versus sinθ

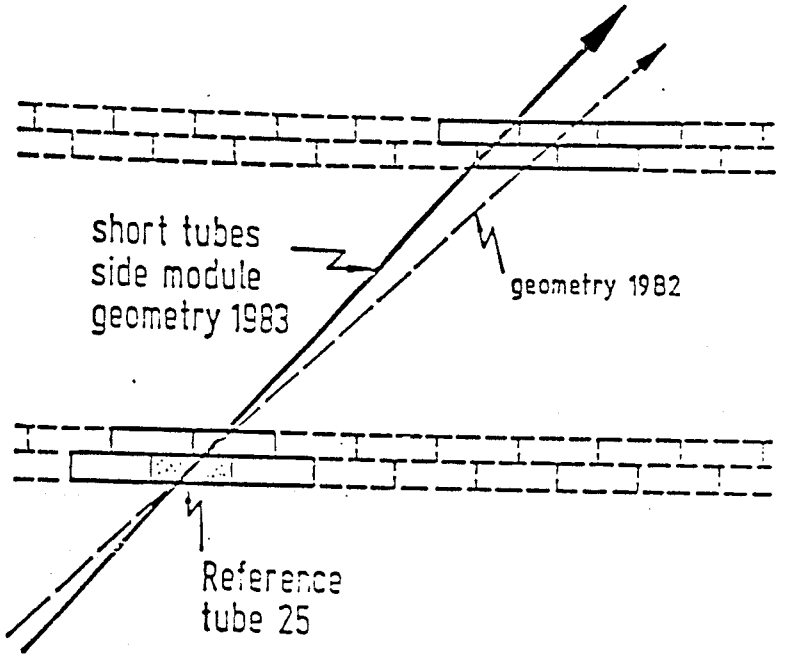

Figure 22: Comparison of the 1982 & 1983 geometry

inefficiency from the hadron calorimeter and the linearity in $\sin\theta$ was understood after further work with Monte Carlo programs at Aachen, where the original trigger and chambers were designed and made. Between the 1982 and 1983 runs the chambers were moved outwards from the vertex to allow for the introduction of extra absorbing iron. This changed the optimum choice of the groupings of the trigger units, although the printed router boards controlling the tube groupings had been left with the old configuration (figure 22). It was this effective contraction of the cone size with $\sin\theta$ which had led to the linearity of the efficiency with this variable. For the 1984 run new router boards were printed and exchanged for the old ones, and the hadron calorimeter junction box rewired.

3.3 Proposed Improvements to the Muon Trigger

The muon trigger was operational from the start of the 1983 run, but from the previous section it can be seen that it was not at optimum efficiency. In a note at the end of the 1983 run several improvements were proposed [27]:

- When a tube is dead, it gives a 'hit' signal which although safe can lead to multiple triggers in a region where full track reconstruction is a priori impossible. As only three hits are required to form a cone then by forcing the dead tubes to 'no hit', the local trigger efficiency does not drop to zero but remains at 70%.
- In 1983 the communication between the trigger and the user was via a Motorola 6800 microprocessor. By upgrading this to a new 68000 series microprocessor, it was hoped to increase the speed and versatility of checking and testing the hardware.
- The original construction of the trigger had envisaged facilities to check the status of the cards in the fast trigger crates and data on the interconnecting address lines. Due to lack of time this had not been fully implemented in the 1983 run, but it was hoped to be ready for 1984. An added complication was that this information had to be double buffered.
- Due to the improvements in the Antiproton Accumulator, it was known that the luminosities in the 1984 run would be higher than in 1983. The trigger rate from the muons would therefore have to be reduced to keep the overall deadtime of the experiment small. This was possible with the design of extra logic units (extension cards) which could take the decisions of the trigger and fold in a predefined region of acceptance in each module. This also meant that as the luminosity fell during a shot it would be easy to increase the acceptance of the trigger.
- Later in the year [28] additional chambers were to be added to increase the muon acceptance in the forward region, requiring extra trigger electronics, and their incorporation into the software.

All of these improvements were implemented before the 1984 run. The muon chambers and associated trigger had been designed and built in Aachen in Germany, and it was decided that the electronics and chamber construction work should be done there. The author was responsible for the replacement of the old microprocessor with the new MC68010 and so a summary of this work will follow.

3.4 An Interface to the Fast Trigger

The nature of a trigger needs it to read in a large number of signals (in this case 6,124), process them in parallel and output one bit of information. These are very different requirements for loading the trigger fillings; each memory chip needs to be accessed separately from the few lines between the trigger and input processor containing the fillings.

In figure 23 we show the connections in the muon trigger. Before 1983 the trigger was accessed via a FORTRAN program at the NORD data acquisition computer. The program accessed a slow CAMAC link to a microprocessor, which gave commands to the sequencer, which sent signals to the fast trigger bus linking the crates. The sequencer was designed and built at CERN and contained 16 instructions burnt into two PROM chips, and these offer the (restricted) communication with the trigger. For the simplest command, to write to a chip, one needs to execute 1043 of these sequences, and due to the inflexibility of the program in the old processor a large fraction these commands had to be sent from the FORTRAN program separately. A versatile system became possible after the release of the MC68010 micro which is faster, and has a greater memory addressing range than the MC6800. This enabled the final version of the system to be run in the microprocessor, rather than via the slow link.

The Motorola 68010 chip became available in 1982, and Data-Sud-Systemes tendered a design for UA1 and manufactured a board to incorporate the CPU into a VME module, CPUA1. VME (Versa

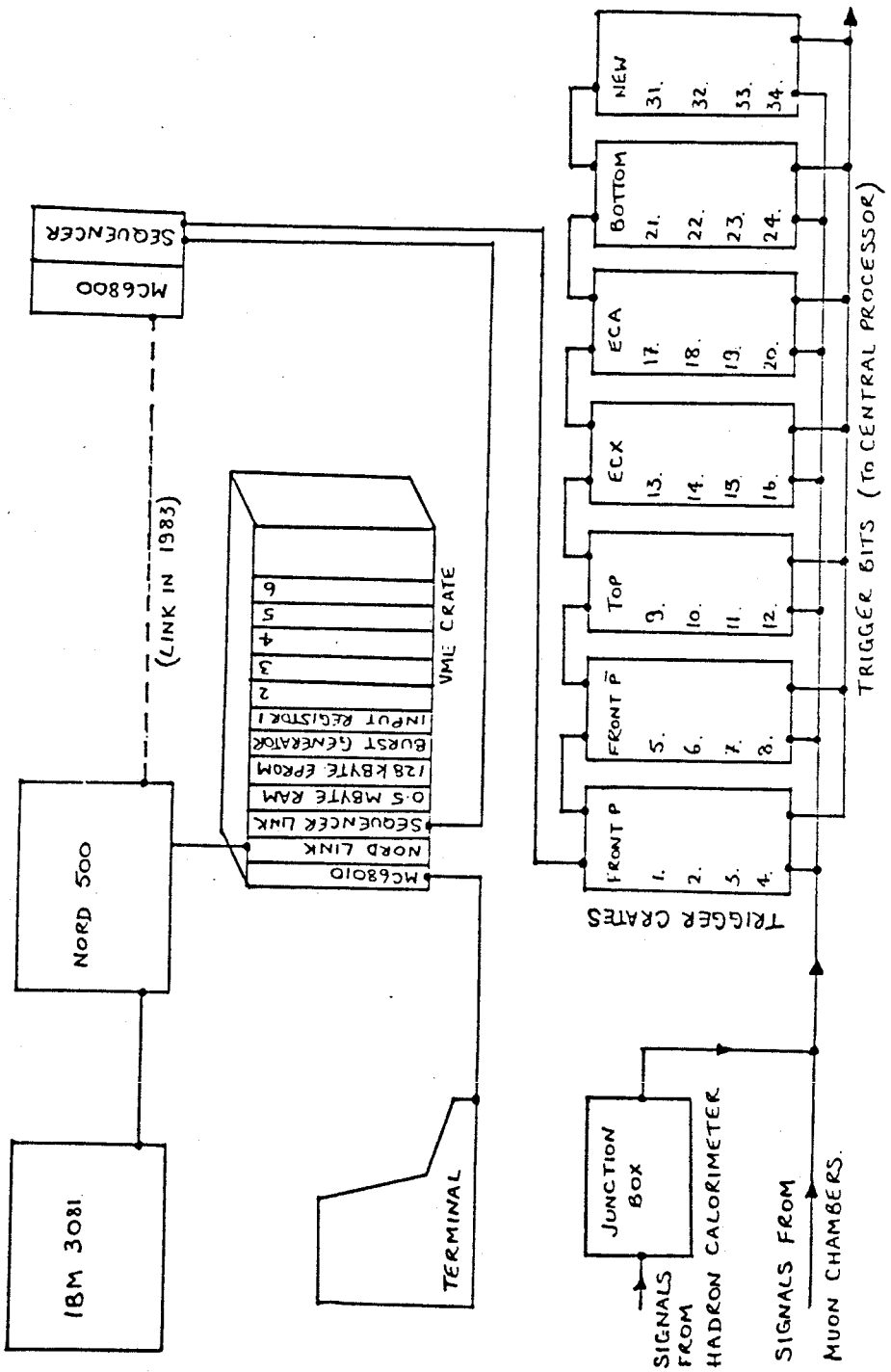

Figure 23: The Muon Trigger Layout

Module Europa) is a European industrial standard for crate electronics, replacing the CAMAC system which is generally not used outside research laboratories. The first prototypes arrived in the spring of 1984, one of which was used for the muon trigger. In May a plan of the program to run on the micro was written [29] describing the function of the CPU and the user requirements. It was decided to use the new program (named VMEFT) either from a terminal connected to the CPU, or from a program at the NORD. There were no high-level language compilers available at the time so the language to be used had to be 68000 assembler. Programs written in assembler language are generally faster and smaller due to the overheads introduced with a compiler, however the programs are more difficult to write and to debug.

3.5 Commands in VMEFT

As it stood, CPUA1 contained little backup software. A basic monitor (CPUA1MON) had been written by members of UA1 [30] for handling input/output, error exceptions and to run programs. VMEFT had to contain its own command interpreter, hexadecimal conversion and file management system. The final manual for the commands written and implemented in the program by the author appears in Appendix B, the commands fall into five categories;

1. commands associated with the CPUA1, initialising micro, returning to CPUA1MON;
2. accessing the hardware for test purposes;
3. commands used by people on shift to load and verify memory fillings;
4. file handling commands, such as creating, appending, renaming, deleting files;
5. commands for the execution of a list of commands in a file, with conditional branching.

The final category was found necessary just before the beginning of the 1984 run, when it was realised that the link between the VME crate and the NORD would not be ready in time. By having a facility

to execute a list of commands in a file, one could produce macro files for people on shift to load, change and check the trigger, automatically logging the information in a file for later study. During its development, VMEFT was used extensively to test the extra pieces of equipment which had been constructed at Aachen and brought to CERN for installation. The main problems encountered were associated with the timing of the equipment, or occasional failure of the one of the few thousands of chips incorporated within the trigger. As the hardware and software were being developed and tested simultaneously it was possible to change the original program design to suit the needs of the hardware.

By the time of the run in September 1984, the system was operational and ready for data-taking, the versatility was proved to be necessary with the high luminosities encountered, and the methods for testing the memories for hardware faults proved to be invaluable.

3.6 Origin of the Trigger Background

There are six categories of background important for the muons in $\bar{p}p$ interactions;

1. Amplifier Oscillations
2. Beam-Halo
3. Leakage of hadronic showers
4. Punchthrough of hadrons
5. Cosmic Rays
6. Decays in flight of $\pi^{\pm}$'s and $K^{\pm}$'s

These sources of background may be partially removed by scanning on the MEGATEK by physicists, but the trigger is used to remove part of the background arising from points (1) to (3) before sending the events to the second level trigger. These three forms of background occur at a much higher rate

than the rate of muons from minimum bias data (at the level of one per million beam crossings). Punchthrough from hard hadrons (>2 GeV/c) is small, the probability of a hadron penetrating the nine interaction lengths of iron is 0.0001 $\sin\theta$ in the central region. Cosmic rays form the greater of the dimuon trigger rate, which is of the order of 10^{-7} of the first level single trigger rate. Such events can be removed by scanning; their rate is reduced by the momentum cut from the 35 m of concrete above the experiment, and the time window of $\approx$200 ns per beam crossing imposed by the trigger timing. Kinks are from the muonic decay of pions and kaons in flight from the vertex. They form a large part of any muon data sample and are removed by tight quality cuts on the track in the central detector and tight matching cuts between the tracks in the muon and central chambers. The contribution of kinks in the final W sample was $<10\%$ for the 1983 run, and 12% in the dimuon sample. A more detailed explanation of this type of background is given below in chapter VI.

Amplifier oscillations occur most frequently at the beginning of a shot, when the powerload in the experimental region is at its greatest. They arise due to a design fault in the muon chamber readout system. The time constant of the amplifiers (60 MHz) is close to the time for a signal to propagate along the wires in the chambers (6 m). Any power surges in the supply to the experiment cause spikes in the voltage for which the muon chamber amplifiers and cables provide a positive feedback loop. Oscillations in the chambers are recognised immediately on shift, as the large amount of data cause overwrites in the data acquisition system. They are cured by switching the amplifiers off and on for one second.

Beam halo events arise from stray beam particles interacting with material around the beam pipe. Muons from these interactions travel parallel to the beam along LSS5 and are scattered by the shielding iron and magnets near the experiment and can strike the forward muon chambers giving first level triggers. From test data taken during the 1984 run we are able to locate the source of the beam halo. Figures 24 and 25 show the extrapolation of the track in the muon chambers for such events to the point of closest approach to the beam [31].

The x,z projection of the 'vertices' in figure 24 shows broad objects at 6 m from the vertex along the x axis, these are the positions of the compensating magnets. More 'vertices' are observed at positive

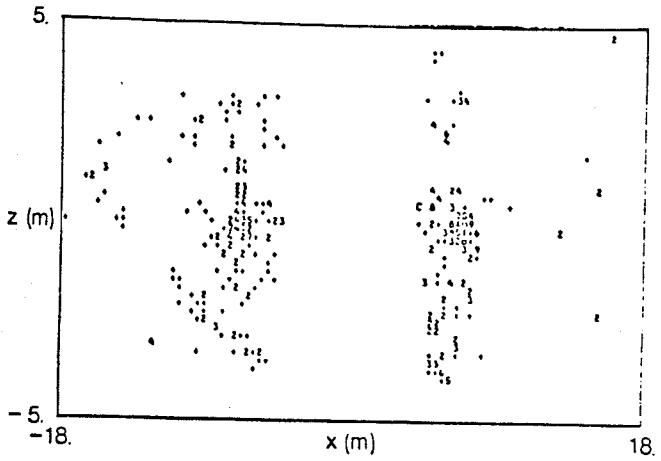

Figure 24: Origin of Beam-Halo, x,z projection

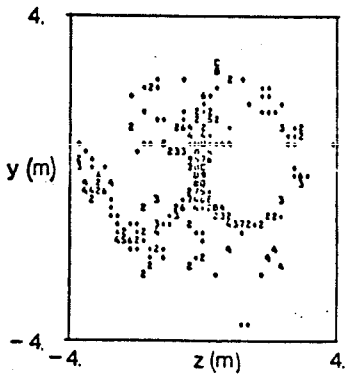

Figure 25: Origin of Beam-Halo, y,z projection

x as the proton bunches have a higher density than the antiproton bunches. Figure 25 is the end elevation, it is interesting to note that the radius of the SPS tunnel at 2.8 m and its flat floor, are clearly visible. Plots such as these help define the position of the scattering material, and justify placing the extra iron inside the beam tunnel to shield the experiment.

The effect of this background is to produce tracks which do not point to the vertex, in figure 26 the angle between the track vector and a line pointing to the centre of the UA1 coordinate system is resolved in the vertical and horizontal directions. The majority of the tracks are not pointing to the vertex, but are at an angle of > 400 mrad from the line to the vertex. Figure 27 shows the regions of the chambers excluded in the trigger when the data shown in figure 28 was taken. There is an improvement in the signal to noise ratio, with little loss of useful data.

Leakage, where a hadron shower is not fully contained in the iron, mainly occurs in a 10 cm gap between the two halves of the magnet return yoke in the vertical medial plane. The only place where muon chambers sit directly behind the gap are again in the forward regions, where the trigger fillings of two of the reference cones in the vertical projection were set to give no trigger. Later in the run, these gaps were plugged with extra iron, so that the trigger fillings could be replaced with the active fillings.

3.7 Trigger Efficiency in 1984

The effects of the improvements to the trigger can be clearly seen in the 1984 data. We use the express line data which has been fully processed to search for muons in events with or without a trigger from the muon trigger processor. Figure 29 shows the muon p_t spectrum for these events, the cut at 8 GeV/c is for single muon events.

The trigger acceptance was increased by using the signals from the extension cards in coincidence with jet or electron triggers. The new triggers from the final level logic are listed in table 7. The extension cards made it possible to use different acceptances for the trigger bits 9, 10, 15, 16, 17 and 18. The larger acceptances were obtained by including more of the tubes in the forward region, close to the beam pipe where the background was higher.

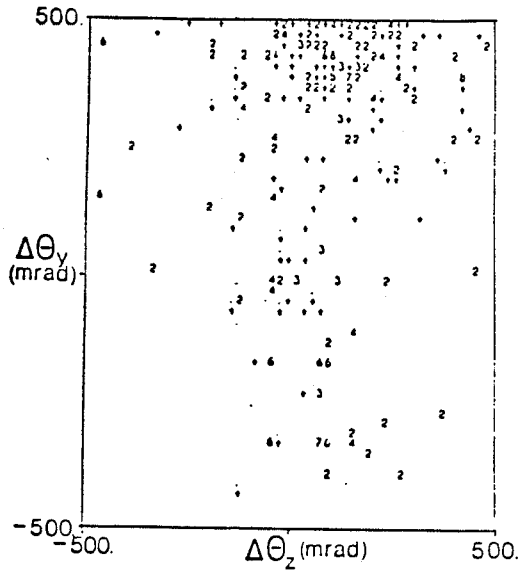

Figure 26: Projected angular differences in forward modules

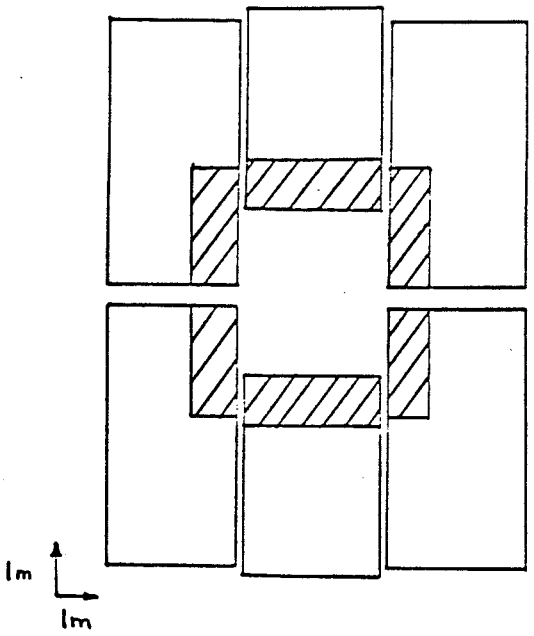

Figure 27: Veto zones in forward modules

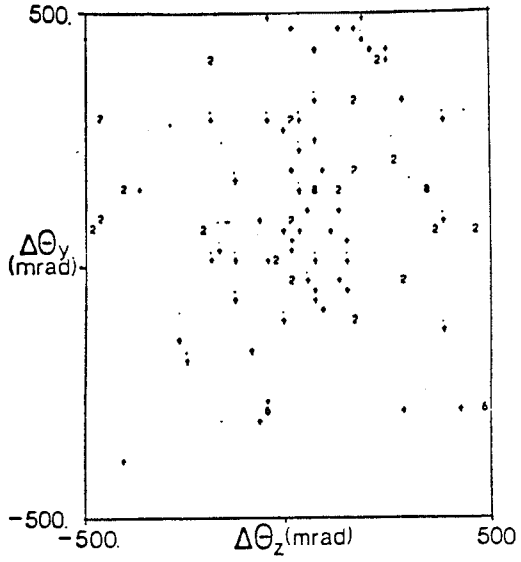

Figure 28: As figure 26 after veto zones applied

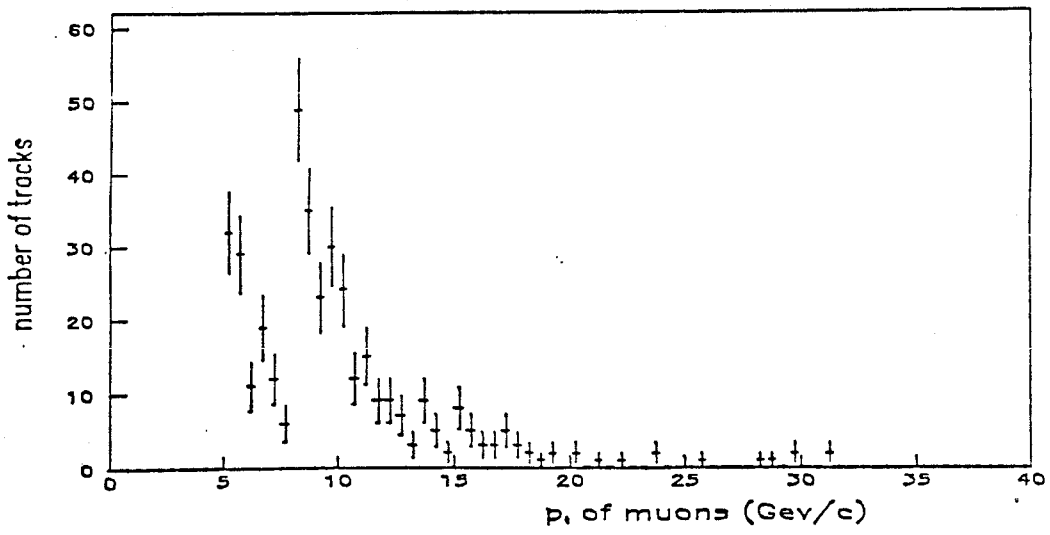

Figure 29: P_t spectrum of the 1984 express line sample

Following the same procedure described in section 5.2 for the 1983 data, we are left with 397 muons, of which all but seven have muon triggers. This gives an inclusive trigger efficiency of 98%.

Table 7: Trigger Bits from the Central Trigger Processor in 1984

bit	type	thresholds
1.	1 electron	10 GeV
2.	1 electron	10 GeV
3.	1 jet	25 GeV
4.	2 jets	15 GeV
5.	sum transverse energy	80 GeV
6.	2 electrons	6 GeV
7.	electron.diffractive $+x$	-
8.	electron.diffractive $-x$	-
9.	1 muon	2 GeV/c
10.	2 muon	2 GeV/c
11.	cosmic	-
12.	free	
13.	(E_t imbalance).(1 jet)	17 GeV, 15 GeV
14.	(E_t imbalance).(1 jet)	17 GeV, 15 GeV
15.	(1 muon).(1 jet)	2 GeV/c, 10 GeV
16.	(1 muon).(1 jet)	2 GeV/c, 15 GeV
17.	(1 muon).(1 electron)	2 GeV/c, 8 GeV
18.	(1 muon).(1 electron)	2 GeV/c, 10 GeV
19.	pion (C frontstack)	8 GeV
20.	pedestal monitor	-
21.	1 electron (check)	10 GeV
22.	1 electron (check)	10 GeV
23.	minimum bias	-

The seven muons have been scanned, and all were found to have hits in the hadronic cells which were crossed by the muon. Two of the muons are in the same event, where two muon chamber tracks (from the same particle) have been associated to separate tracks in a jet. The events with a reconstructed muon but no muon trigger fall into three groups;

a. track not pointing to vertex;

b. dead tube not firing;

c. track close to edge of chamber in bottom chamber.

Table 8: Muons with no trigger in 1984 run

run	event	module	P_t	$\sin\theta$	reason for failing
9475	1127	25	27.09	0.999	a
11696	1281	26	8.32	0.810	b
12159	725	11	1.98	0.921	b
12327	224	12	5.62	0.875	b
13188	985	26	3.86	0.836	c
13188	985	26	7.85	0.764	c
12090	201	9	8.68	0.752	b

key

a track not pointing to vertex
b tube did not fire
c hit near edge of chamber 26

The track which does not point to the vertex is from leakage of a muon through a gap in the iron, it does not point to the vertex and would not have passed scanning requirements (figure 30).

Group (b) result from muons passing through the inactive regions between tubes. The tracks close to the edge of chamber 26 are an indication that the trigger fillings will have to be changed before the next run for this reference tube. The tracks are scattered randomly about the chambers, and the efficiency appears roughly independent of track momentum, although the statistics are low. It is important to note that the efficiency is independent of $\sin\theta$, indicating that the new groupings of the trigger units have been optimised. We can therefore say that the work on the muon trigger upgrade has increased the trigger efficiency from 60% to 98%.

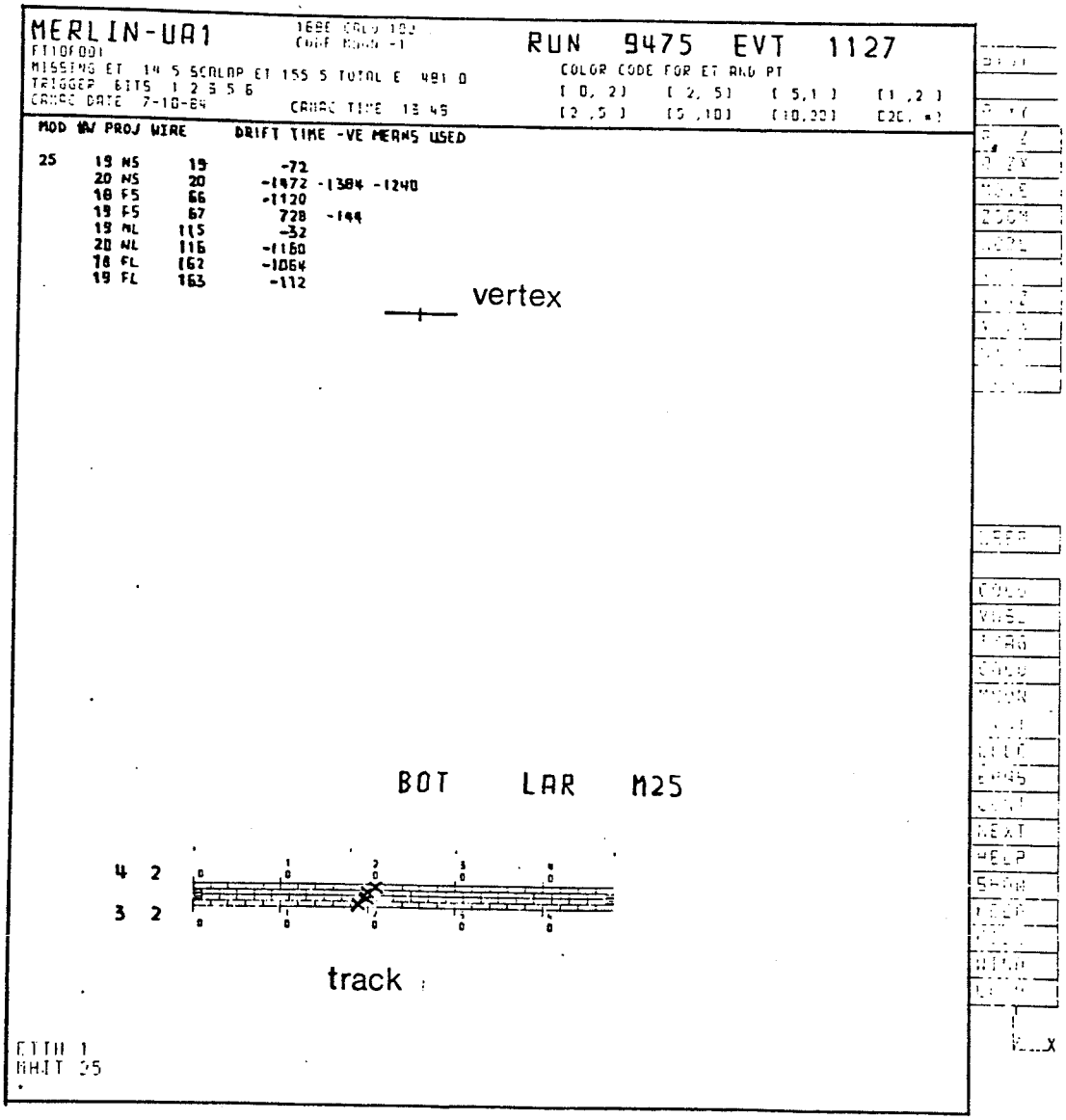

Figure 30: Track which does not point to the vertex

3.8 Further Developments of the Trigger System

The muon trigger has been shown to detect muons reliably, but these muons are not always associated with the interaction vertex. The next stages planned for the trigger are to increase the monitoring facilities of the trigger, now that a FORTRAN compiler is available on the CPUA1 extra coding can be written and changed more easily. It is hoped to control VMEFT via a FORTRAN program from either the NORD or another microprocessor which starts complex testing procedures to analyse any discrepancies found on shift. When one finds an error in the reading back of a filling, it can be due to a memory chip failure or a problem in the communication to the chip. Until now, the diagnosis is left to people who have had experience in the building of the hardware, but it is possible to write an algorithm to do this, speeding up the process of repair. It is also known that the memory fillings do not yet have optimum efficiency, and it is hoped that they can be improved after Monte Carlo studies.

4. THE MUON HARDWARE UPGRADE

The evidence of the production of the IVBs from their decay into leptons has shown the importance of the detection and measurement of high momentum electrons and muons in UA1. Leptons with lower momenta are important for the validation of physics associated with Drell-Yan and heavy flavour decays, they are also important in verifying any current theories which predict new particles that decay to quarks and leptons. Therefore a detector such as UA1 requires efficient lepton detection over the whole of the momentum spectrum. This is not possible for low energy electrons (below 8 GeV) because there is a large background from jets which fragment to neutrals and a single charged track. Muons can be identified down to 3 GeV/c because of the nine interaction lengths of iron between the vertex and the chambers. However the background from muon decays in flight of charged pions and kaons restricts one to a momentum above 5 GeV/c. The momentum resolution is limited by the measurement of the track sagitta in the central drift chamber, resulting in large errors for tracks which have a high momentum or travel parallel to the magnetic field in the central drift chamber. At the end of the 1983 run it was decided to increase the muon detection (to increase the acceptance for low p_t leptons) and improve the muon momentum resolution (to supplement the electron identification at high momentum). This was to be achieved by extending the area covered by the existing type of muon drift chamber, and also by placing new chambers between the existing muon chambers and the calorimeters. This chapter is concerned with the development of the new chambers.

4.1 Extra Muon Detection in UA1

The error for muon momenta measurements in the 1983 run was greatest for tracks in the horizontal plane of the experiment, where they are parallel both to the wires in the drift chamber and to the dipole field. After the run in 1983 it was proposed [32] to magnetise the extra absorbing iron to 1.2 Tesla and to instrument it with streamer chambers. The shields at the sides are three 20 cm sheets of steel plate separated by two 4 cm gaps, with a shield at the top of 40 cm of iron (figure 31). For a

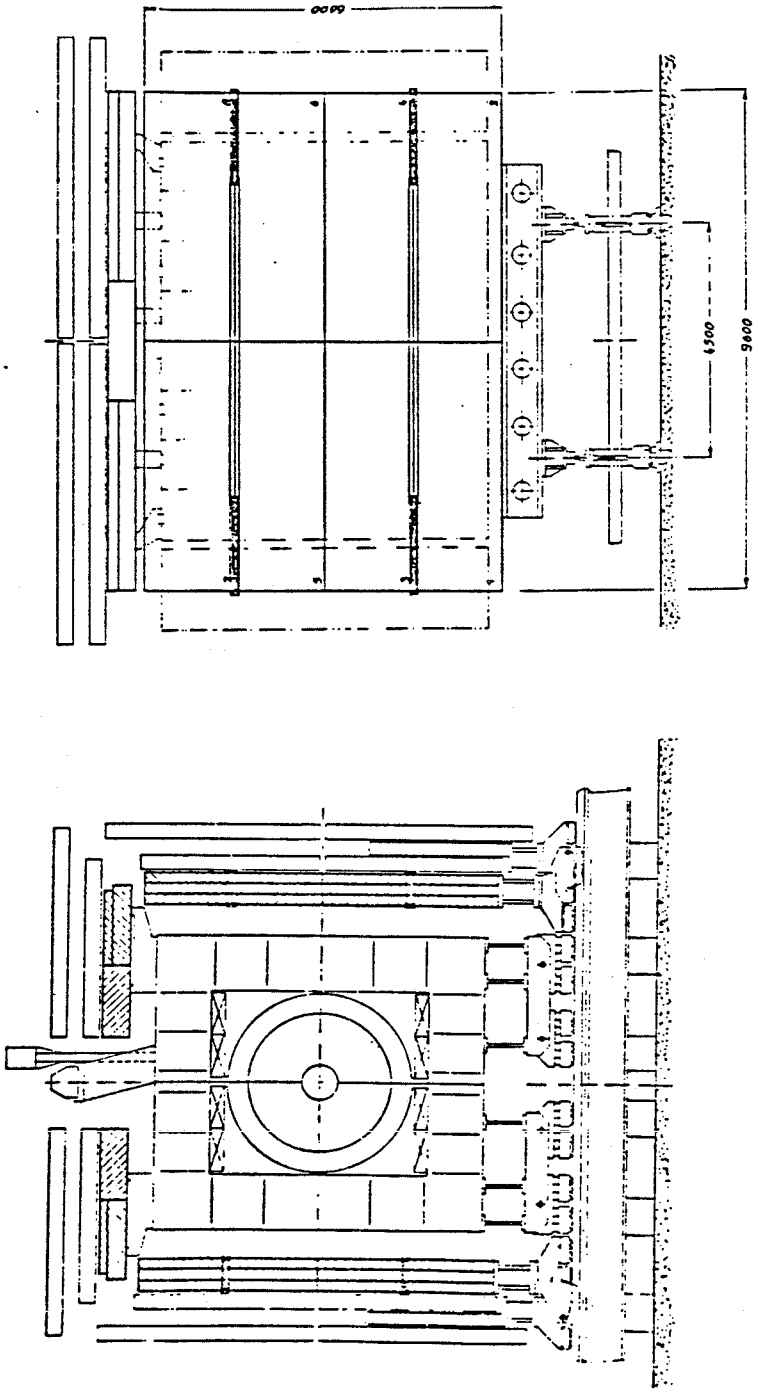

Figure 31: Section and elevation view of top and side muon shields

horizontal track in the central drift chamber, only the direction of the track is measured reliably. Using this information and the direction of the track in the muon chamber, the momentum resolution is [33]

$$\Delta p/p = 0.014p \text{ (units of GeV/c).} \qquad 4.1.1$$

By measuring three extra points on the track with detectors inside the iron slots to an accuracy of 0.5 mm, the resolution improves to

$$\Delta p/p = 0.010p \text{ (units of GeV/c).} \qquad 4.1.2$$

The extra information for the tracks which penetrate the hadron calorimeter will also help in the rejection of background from decays of $\pi^{\pm}$'s and $K^{\pm}$'s inside the central detector, (as described in the last chapter). Over 870 m^2 of detection were proposed and later, extra detection was placed in the forward region and underneath the dipole magnet, increasing the area to 1600 m^2. The requirements of such a detector were that it should be able to operate in the limited space between the iron plates and be possible to produce quickly and cheaply in bulk. The choice of chamber was a type of plastic streamer tube with analogue strip readout, called Iarocci tubes. These tubes had been developed for use in the Mont Blanc proton decay experiment [34-36], but it was necessary to investigate their properties under the conditions imposed by the collider. A complete description of the apparatus and tests is being prepared [37]. The author was involved in the track reconstruction in these chambers from cosmic and beam-line tests at CERN, and a description of that work follows.

4.2 Construction and Operation of Iarocci Tubes

Iarocci tubes are single wire chambers operated in a limited streamer mode. They consist of a 1 cm square extruded PVC tube with a 0.1 mm diameter silver coated Be-Cu wire running along its length (figure 32). The PVC tubes are constructed from a profile with 9 mm spacing and 1 mm wall thickness, and a 1 mm thick cover. Originally, the inside of the profile was coated with a graphite

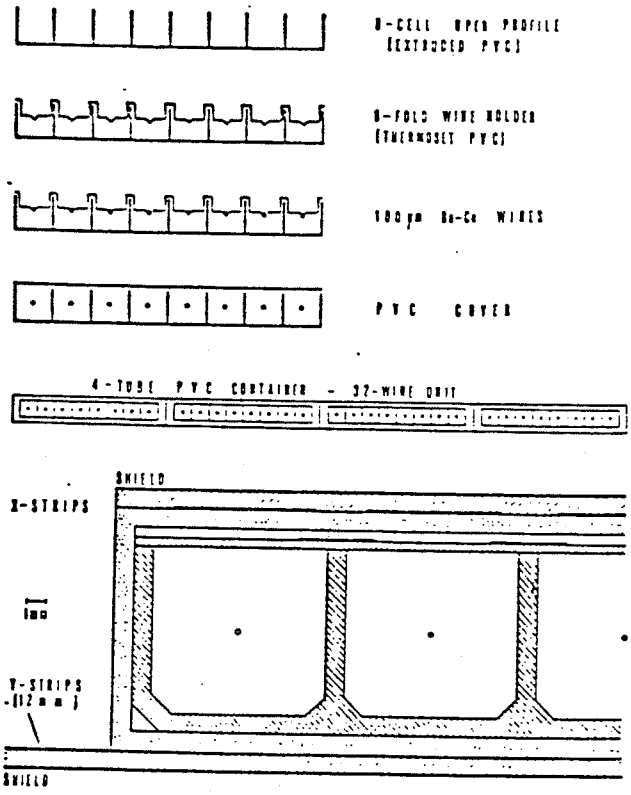

Figure 32: Iarocci tube Cross-section

varnish, and the tests were used to investigate the optimum thickness of the varnish for the chambers. In the first tests the cover and profile had resistivities, $\rho \approx 0.2$ MΩ/cm², and later this was changed to 3-10 MΩ/cm² for the cover and < 1 kΩ/cm². for the profile. It was found that the uniformity of the graphite on the covers was difficult to control (bearing in mind that over 22 km of PVC strip was required), and during the final production of the tubes this problem led to the decision to use tubes with no graphite varnish.

Under operation the wire is kept at a potential of + 4.2 kV with respect to the grounded graphite cover, and a 1:3 gas mixture of argon : isobutane passes through the tubes. Readout is achieved with cathode strips placed adjacent to the covers and perpendicular to the wires. The strips are made from 1 mm thick PVC sheets, which have been double faced with aluminium foil and machined on one side to remove 2 mm of foil every 12.7 mm. During operation, they are kept at a virtual ground with respect to the wires.

Particles travelling through the chamber cause ionisation, producing a negative cloud of electrons moving towards the wire and a positive cloud of ions moving towards the profile. The electrons and ions which recombine radiate photons which give rise to further ionisation. The final result is a streamer from the electrical avalanche through the gas which is discharged when it reaches the graphite coating on the cover. The charge deposited by the streamer leaks away across the cover and the change in the ambient electric field induces a charge on the strips outside the tube. It is this charge which is measured as a potential difference across a capacitor connected between the strip and ground.

The STAR [38] readout system was developed specifically for the UA1 experiment. It fulfills the needs of being easy to produce in bulk and is not expensive as it multiplexes each group of 32 channels into an eight bit ADC on a board connected directly to the strips. The calibration of each integrated signal is controlled by a seven bit DAC which is set by pulsing a reference voltage to the input stage of each channel (figure 33). The gain per card was set manually to 100 fCoul/count, and the individual channel gains were set on-line via a 6800 CAMAC microprocessor. The maximum difference between the settings of separate channels was 2%. The cross-talk between channels was found by applying a test voltage to a single channel. A cross-talk of 7% was measured which was found to be significant in the following analysis.

4.3 Methods to Find the Charge Centroid.

The shape of the charge distribution found on the strips depends on

- the strip pitch, w;
- the strip width, t;
- and the resistivity of the cover.

From early tests, the charge was found to be distributed over three to five strips with a shape close to a Gaussian. An exact calculation of the distribution is heavily dependent on the tube geometry, and so a Gaussian distribution was used to investigate how different algorithms biassed the

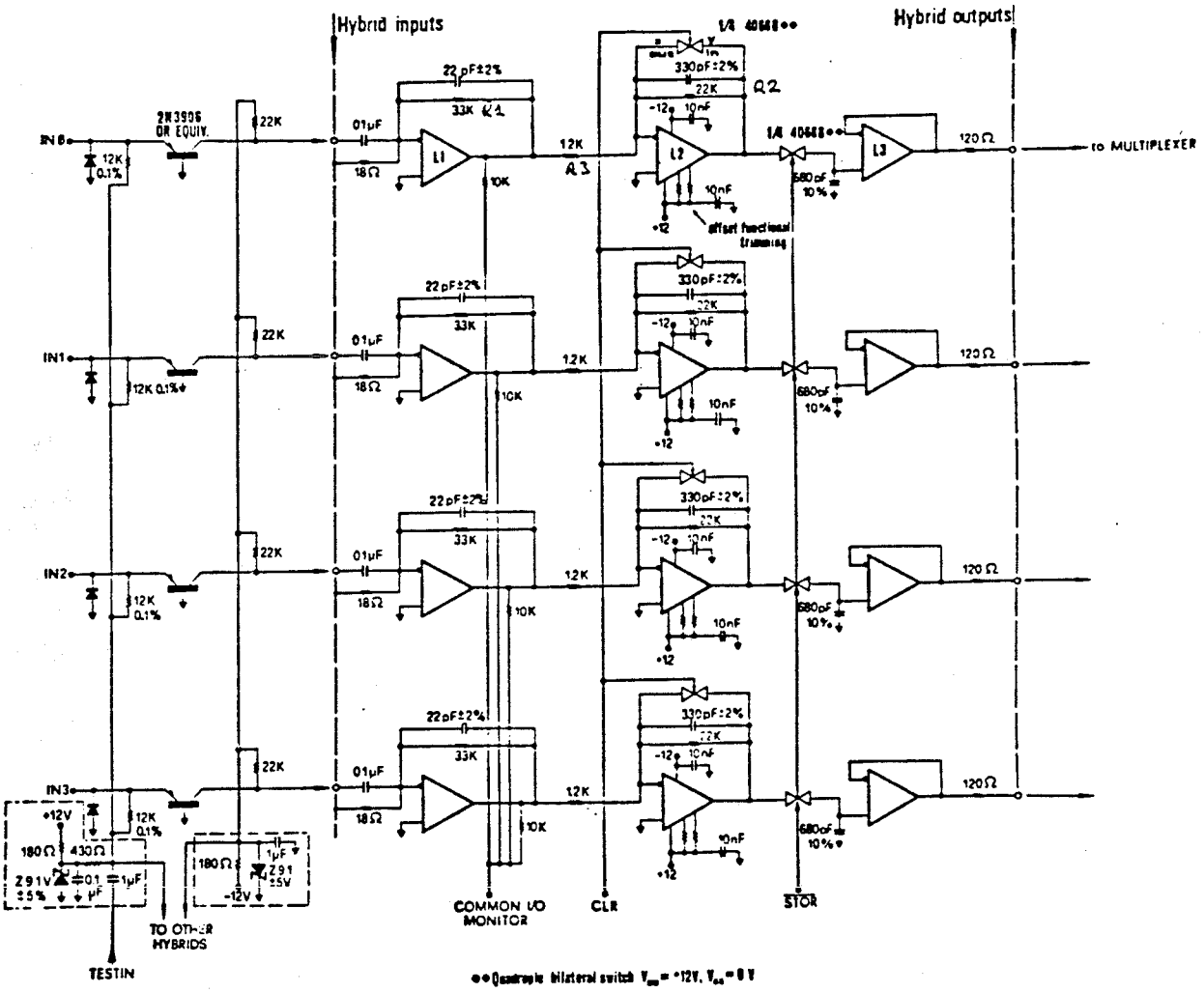

Figure 33: Front end of STAR readout electronics

reconstruction of the centroid of the charge. Two types of simple algorithm were chosen to find the centroid of the charges, by its centre of gravity (COG), and a Gaussian fit. These algorithms have the advantage of being versatile and easy to use. The width and gap spacing of the strips was defined before the tests, and so the only control over the width of the charge distribution was the thickness of the graphite coating.

The simulation program deposited a Gaussian spread charge on five adjacent strips, where the charge on the nth strip is;

$$C_n = A\int_{nw-t/2}^{nw+t/2} \exp-[(x-x_0)^2/d^2]\,dx, \qquad 4.3.1$$

where A is the amplitude of the Gaussian, centred at x_0, and with a spread, d. If we define $\mathrm{erf}(x) = {}_0\int^x \exp(-x^2)dx$, then 4.3.1 reduces to

$$C_n = Ad[\mathrm{erf}\{(nw+s/2-x_0)/d\} - \mathrm{erf}\{nw-s/2-x_0)/d\}]. \qquad 4.3.2$$

We can then attempt to reconstruct the original charge centroid with the centre of gravity (COG) and Gaussian fits, for various values of t/d. The COG fit calculates the centroid position x_R,

$$x_R = \Sigma_i x_i(C_i-b)/\Sigma(C_i-b) \qquad 4.3.3$$

with a width, σ, defined by

$$\sigma^2 = (N-1)^{-1}\Sigma_i[x_i(C_i-b)/\Sigma(C_i-b) - x_R]^2. \qquad 4.3.4$$

Here x_i is the centre of the i'th strip, b the charge from background noise, and the summations are implied over N strips with $C_i > b$. For the Monte Carlo studies the value of b was taken as 1% of the total charge collected on the strips. The Gaussian fit assumes a charge distribution like

$$C_i = A\exp-\{(x_i-x_R)^2/d^2\}. \qquad 4.3.5$$

Taking logs, one obtains a quadratic in x, from which it is possible to calculate A, x_R, and d by a least squares method, for a minimum of three strips with non-zero charge. The method of this fit is described in Appendix C.

4.4 Efficiencies of the Methods

In the original tests with the low resistivity covers, the charge distribution covered three to five strips. This observation can be used to find limits on the ratio between the strip width (t) and the effective width of the streamer (d). The simple Monte Carlo described in the previous section was used to generate streamers evenly across the width of the strip. Figure 34 shows the average, minimum and maximum numbers of strips with a charge above 1% of the total collected charge as functions of t/d. Streamers which have centroids near the strip edge deposit charge on one less strip than the streamers which are centred near the middle of the strip. This plot implies that the data can be simulated by a ratio of t/d between 0.35 and 0.95.

The cross-talk of 7% was then added into the simulation, and the resulting numbers of strips with at least 1% of the total collected charge are shown in figure 35. The ratio of t/d is now bound between 0.7 and 1.35. Using these limits it is possible to use the Monte Carlo to investigate the properties of the reconstruction algorithms. In figures 36 and 37 the residuals for various values of t/d are presented for the COG and Gaussian reconstruction algorithms. The curves show that the algorithms introduce a systematic error which arises from the small gap between the strips. The systematic error depends not only on the algorithm, but also on the ratio of t/d. For the COG method, the maximum residual is 700 μm, and for the Gaussian method it is 55 μm. The residual for the Gaussian reconstruction algorithm is biassed because the original charge distribution was assumed to be Gaussian. The experimental residuals may be much higher. In order to obtain a resolution of below 500 μm, it is obvious that this systematic effect must be taken into account in the final reconstruction algorithm.

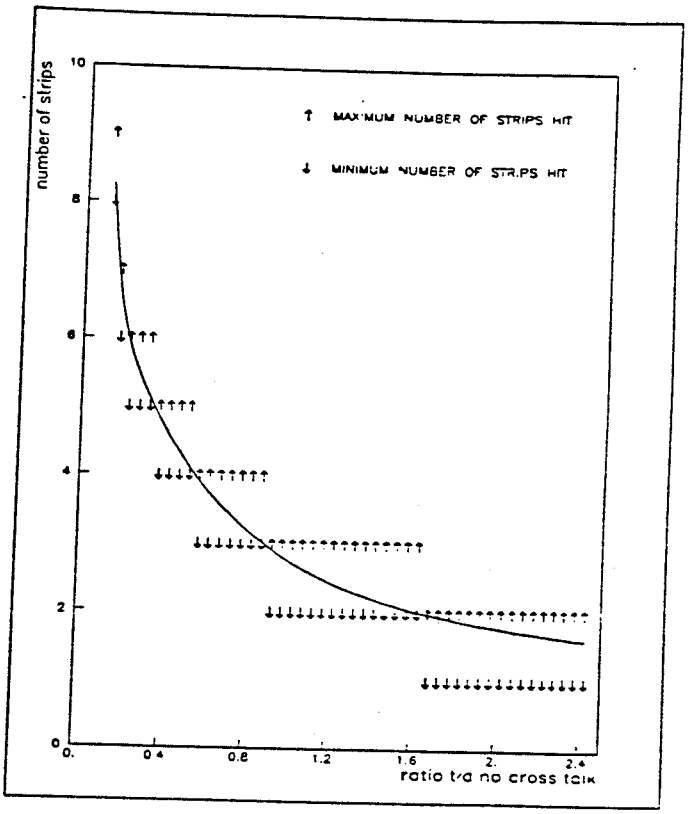

Figure 34: Strips used in the reconstruction, no cross-talk

4.5 Testing the Iarocci Tubes

Over 27,000 cathode strip channels were proposed for the UA1 experiment requiring 31,744 wires, and these all had to be constructed and installed within a year. The individual parts were made externally and the final tubes assembled at CERN. The 'assembly line' at CERN required its own quality monitoring, which was done by comparing prototypes from CERN and Padova in tests using a collimated radioactive source, cosmic rays as well as beam tests at the SPS.

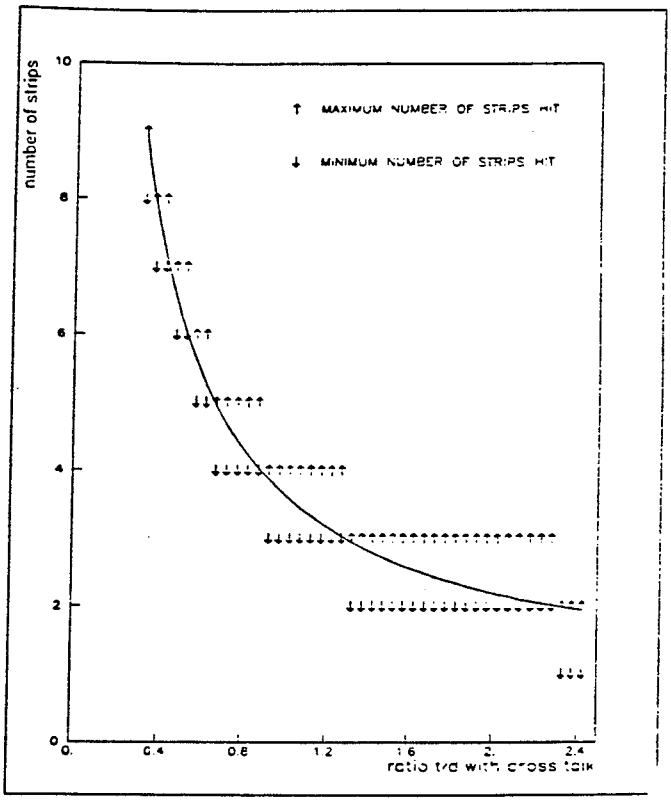

Figure 35: Strips used in the reconstruction, with cross-talk

4.5.1 X-Ray Tests

In these tests a 2 mm hole was drilled in the profile of the tube on the side opposite to the cathode strips and covered with a Fe^{55} radioactive source. The source emits 5.9 kV X-rays which ionize gas molecules and the electrons avalanche in the high electric field near the wire. The streamer from the avalanche is similar to a charged particle passing through the tube, but the ionized electrons are not collimated and so the streamers could discharge on the profile and not on the cover. By moving the position of the source across the strips one could obtain an upper limit for the resolution of the system. For these tests, the final STAR readout system was not yet available and so the signal from each strip was integrated using a high bandwidth amplifier (LRS 3344) and ADC (LRS 2249A). The

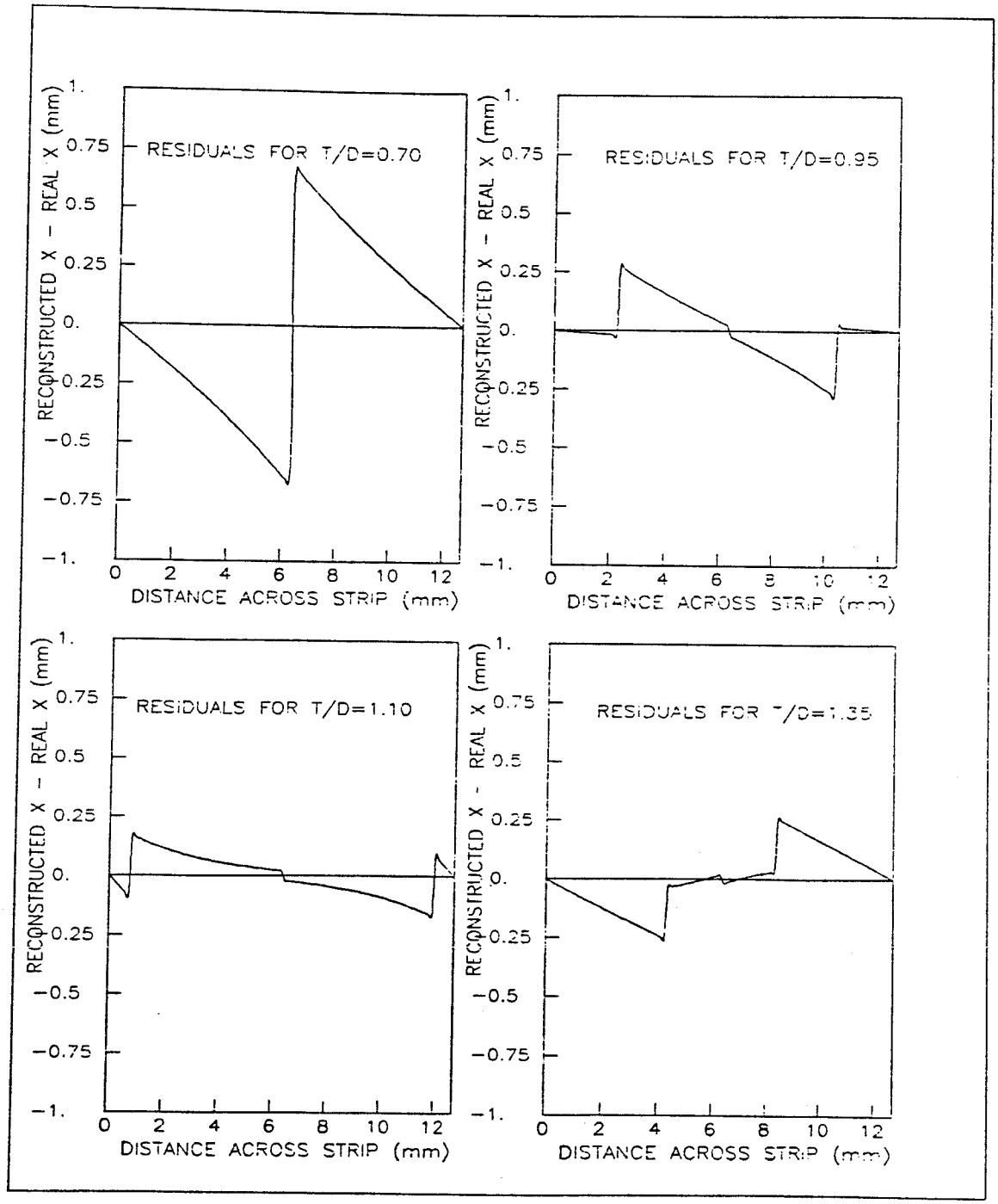

Figure 36: Residuals seen in the Monte Carlo simulation (COG)

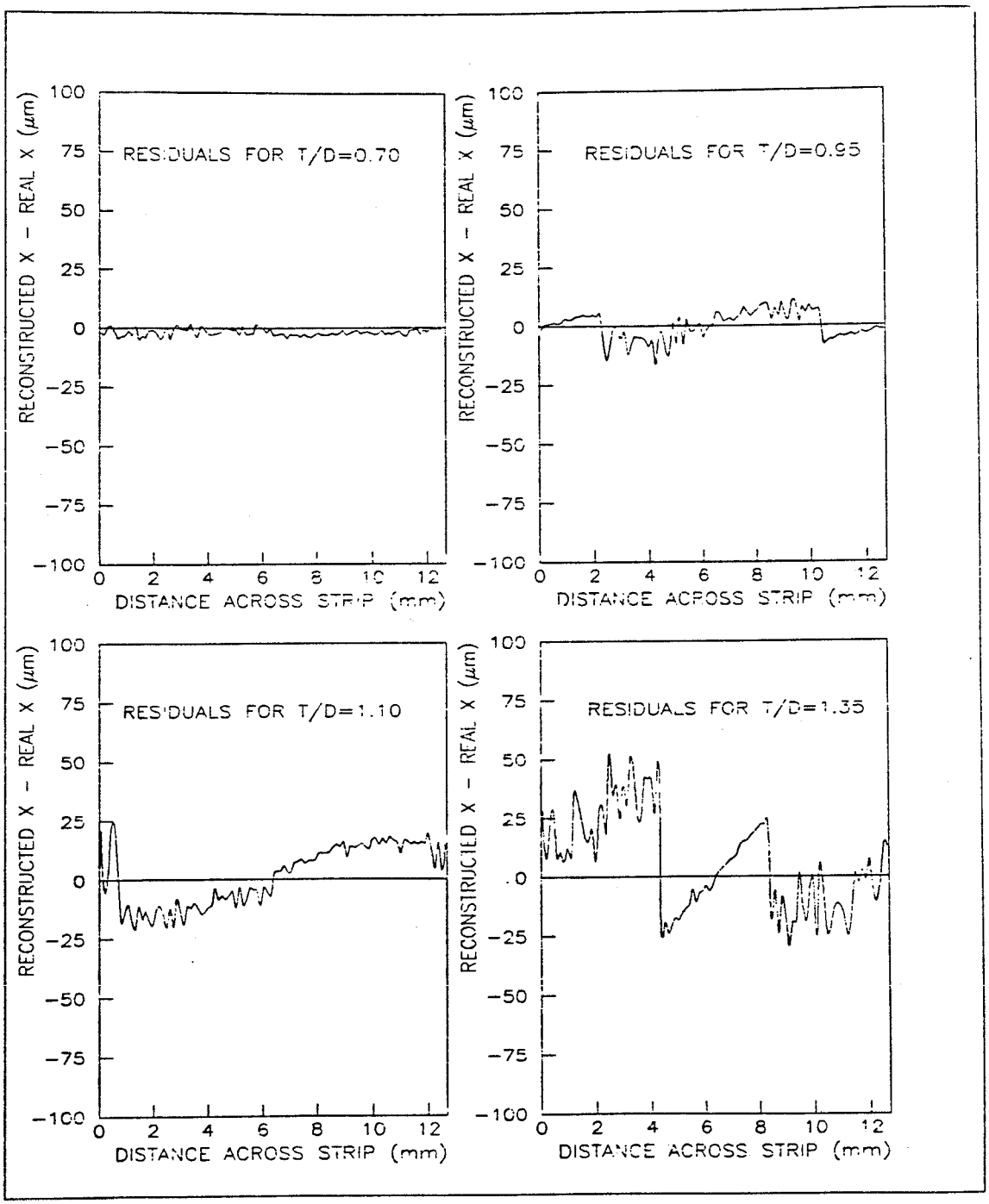

Figure 37: Residuals seen in the Monte Carlo simulation (Gaussian)

system was read out using a CAVIAR MC6800 based microprocessor, written to floppy disk and then transferred to the CERN IBM for analysis.

Figure 38 shows the residuals obtained from the two algorithms during a test of an early prototype. Work done both in Padova [39] and at CERN suggested that a resolution of around 0.5 mm was possible.

4.5.2 Cosmic Tests

A disadvantage in using a source was that the signal was not produced by the same process as with a charged particle, so a bench test using cosmic ray muons was set up at CERN. A small 31 cm drift chamber (a prototype for the UA1 central detector) located the direction of the muon accurately so that one could extrapolate its position to the plane of the strips. A schematic drawing of the layout is shown in figure 39, with a diagram of the electronics of the printed circuit board in figure 40. Again, the final STAR readout system was not yet available and so the strip signals were integrated using a high bandwidth amplifier (LRS 3344) and ADC (LRS 2249A). The drift times from the 31 cm chamber were read out to TDC's via a CAMAC crate and written to floppy disk with the data from the ADC's by a CAVIAR minicomputer. From there the data was transferred to the CERN IBM where it could be analysed. An example of the analysis program showing 12 strip readout and the reconstructed track is in figure 41. To fit the resolution for the strips one demands a knowledge of the residuals of the track in the drift chamber for each wire, $(\xi_i - \xi_0)$ and their average error, σ_i^2. A cut of $(0.5\text{ mm})^2$ was placed on the value of χ^2 of the track where

$$\chi^2 = (N-2)^{-1}\Sigma(\xi_i - \xi_0)^2/\sigma_i^2 \qquad 4.5.1$$

and a fiducial cut was applied to exclude hits near the edges of the strips. The final resolution obtained for the tubes was

$$\sigma = 1.6\text{ mm} \pm 0.1\text{ mm (stat.)} \pm 1.1\text{ mm (syst.)} \qquad 4.5.2$$

The systematic error had two independent contributions.

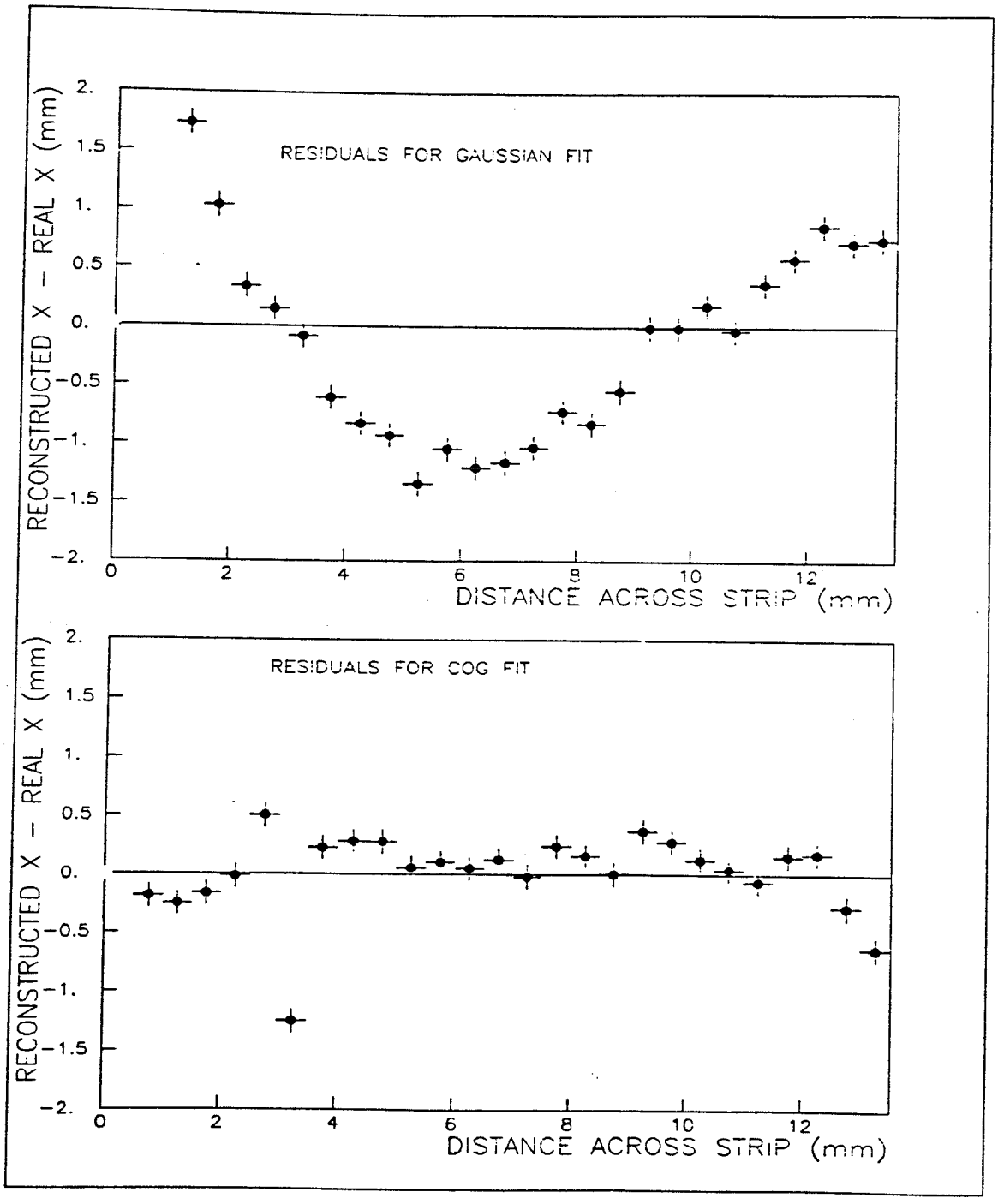

Figure 38: Residuals in X-ray tests on early prototype

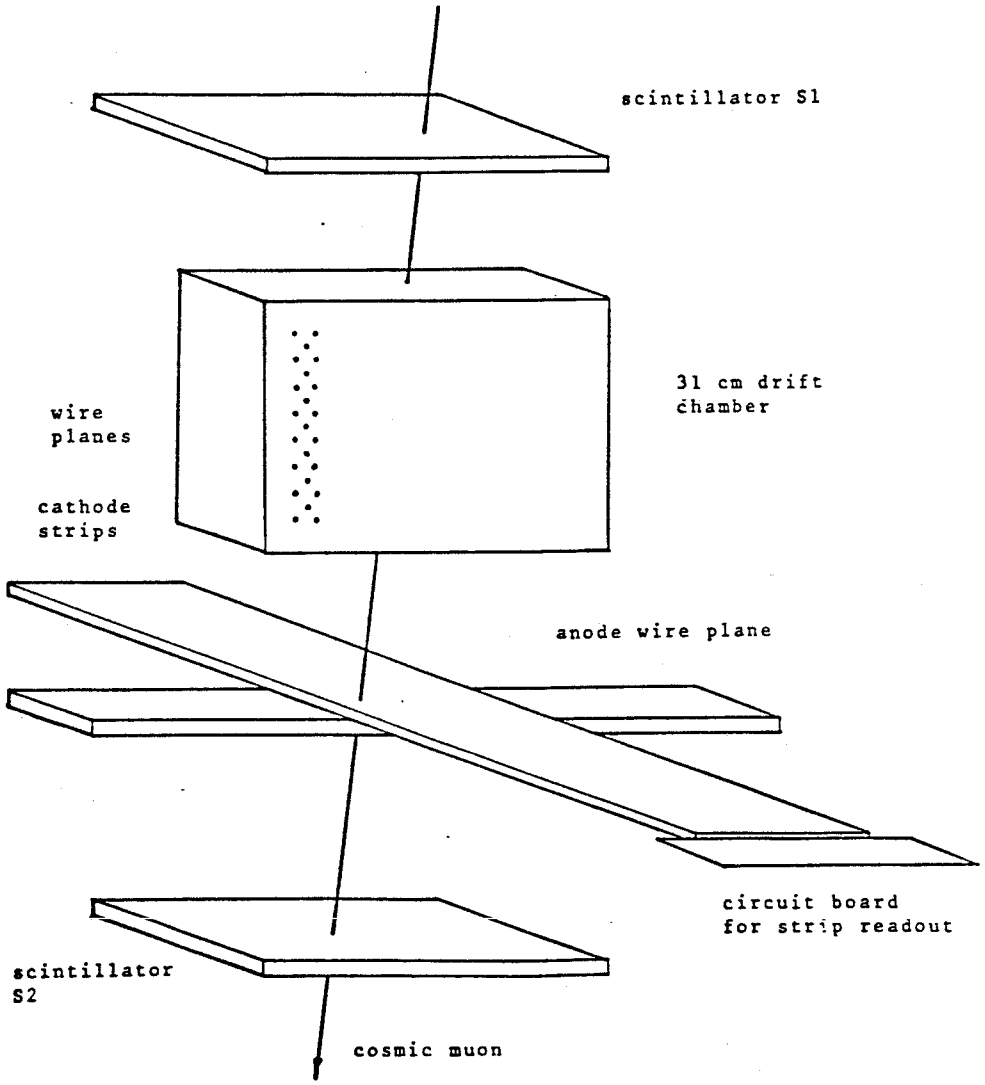

Figure 39: Set-up of the Cosmic Tests

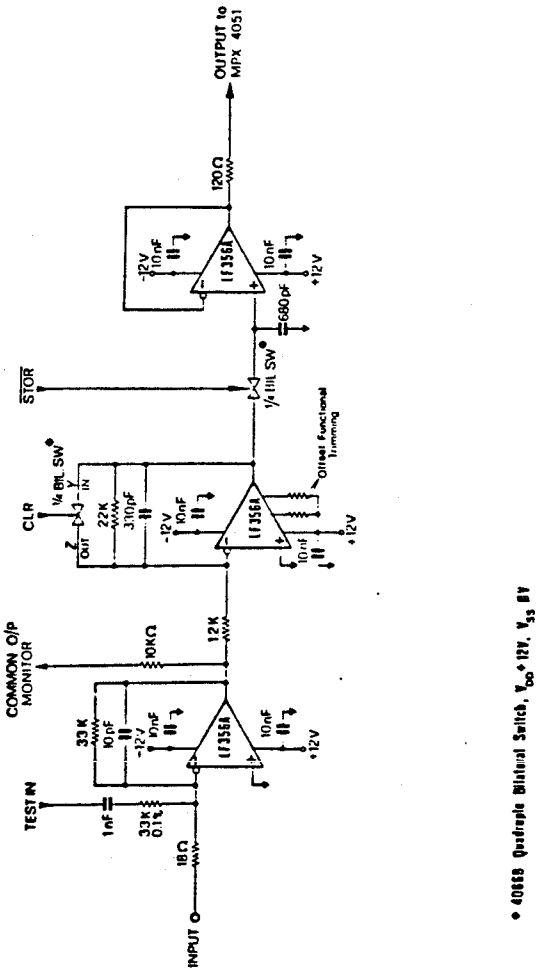

Figure 40: Readout electronics for the Cosmic Tests

- The average projected error of the track in the 31 cm chamber to the plane in the Iarocci tubes was 0.4 mm.
- Only one coordinate was measured on the track in the 31 cm chamber, and the wires in the chamber were not exactly parallel to the cathode strips, resulting in a estimated systematic contribution of 1.0 mm to the resolution.

Hence the derived resolution for the Iarocci tubes was consistent with 0.5 mm.

4.5.3 Beam Tests

For these tests, the muons had an angular spread of only 10 mrad, and so the 1.0 mm systematic error which arose in the cosmic tests was removed. The beam set up was similar to that for the cosmic tests except that there were six multiwire proportional chambers in addition to the 31 cm chamber. The prototypes of the STAR readout system were now available, and so were used instead of the high bandwidth amplifier and ADC.

The STAR card had a longer response time than the previous tests because it used a LF356 operational amplifier, and this gave a much broader charge distribution on the strips. In order to reduce this width the cover resistivity was increased to 3-10 $M\Omega/cm^2$. This change produced a broad background under the primary charge distribution from the image charge reflected by the profile. This was minimised by decreasing the resistivity of the cover to as low as possible, $< 1\ k\Omega/cm^2$.

The uniformity of the cover resistivity at this high value was found difficult to control to within a factor of 2. The charge distributions were very sensitive to these fluctuations and so the following tests used two types of cover, two chambers with the high resistance and two with infinite resistance.

The average charge distributions for the new system are shown in table 9. Tubes 1 and 2 have the high resistivity graphite coating on the cover, and the covers on tubes 3 and 4 have no graphite varnish. The distributions are narrower, and only 2 strips have charge depositions 50% of the time for the high resistivity covers, and 80% of the time for the infinite resistivity covers. This makes it impossible to use the Gaussian algorithm to reconstruct the centroid position. Figure 42 shows the

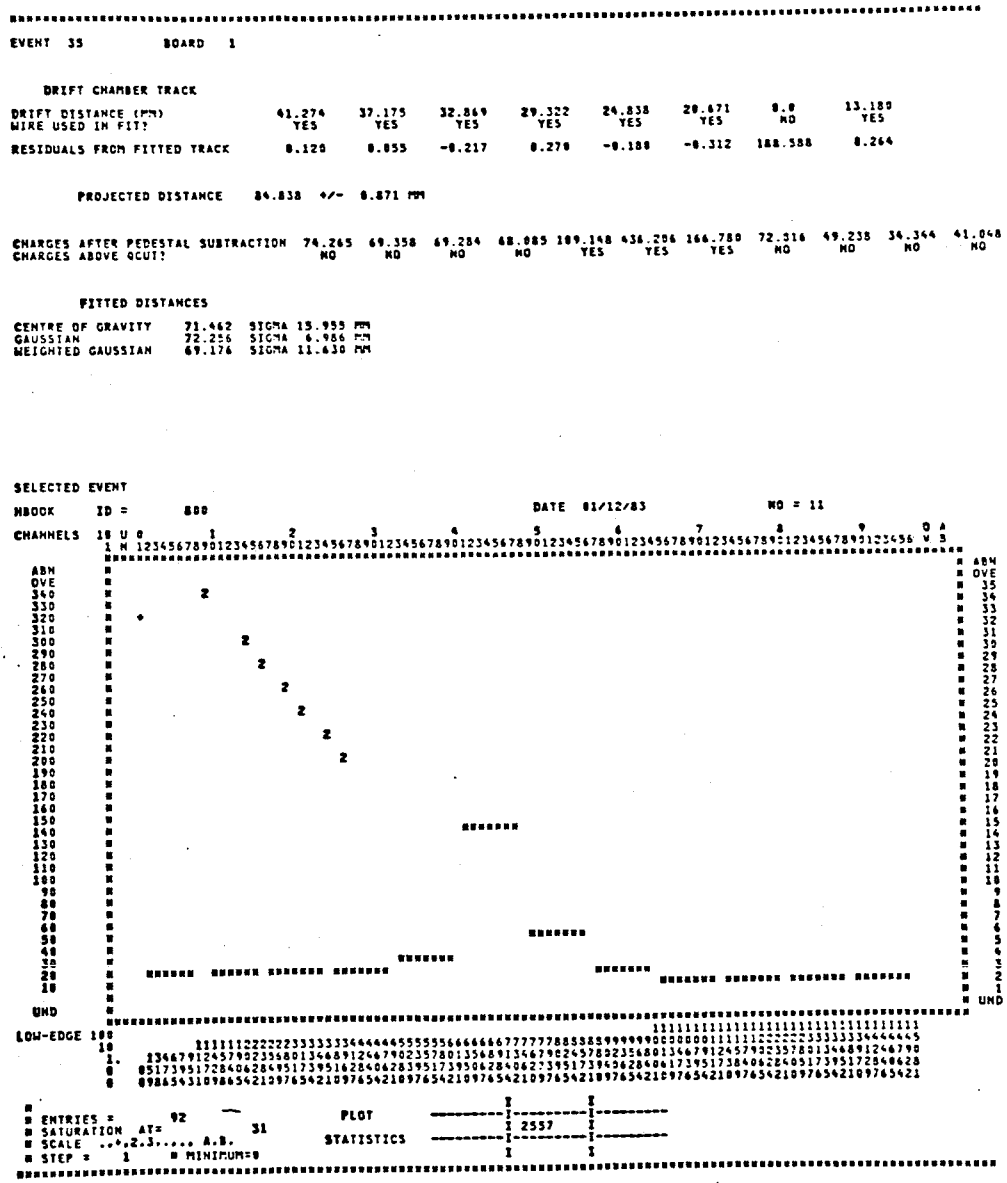

Figure 41: Example of Off-line Display for the Cosmic Tests

Table 9: Average Charge Distributions from the Beam Tests

Tube number	highest charge $\langle q_1 \rangle$ (pCoul)	secondary charge $\langle q_2 \rangle$ (pCoul)	$\langle q_1 \rangle / \langle Q_{total} \rangle$
1	7.7	0.6	0.87
2	4.8	0.6	0.80
3	6.4	0.3	0.91
4	6.2	0.4	0.90

difference between the reconstructed position on the board using the track in the drift and wire chambers and the COG fit, against the distance across the strip for the four chambers. It is possible to see two structures in the residuals; the large structure from the systematic error from the algorithm, and the spread from the resolution of the Iarocci chamber and extrapolated track fit.

Figure 43 shows the systematic error as a function of the distance across the modulo of the strip width, the end points of this plot correspond to the middle of the strip. A fit of ax^5+bx^3+cx+d is overlaid on these plots, and it can be seen that the systematic error is well parameterised by this function. Figure 44 shows the residuals for the strips after the fitted systematic error has been subtracted. The residuals have a Gaussian shape with long tails. If the tails are removed the widths for the four boards are 350, 360, 370, and 380 μm. Including the tails, they are 400, 410, 420, and 440 μm. Removing the average quadratic contribution from the extrapolated track (150 μm) we can conclude that a resolution of 400 μm can be achieved for tubes with or without a graphite coated cover.

4.6 Subsequent Developments and Conclusions

Since the original tests described in this chapter, the Iarocci tubes have been installed in the UA1 experiment and have collected data from the 1984 and 1985 runs. Unfortunately there were problems

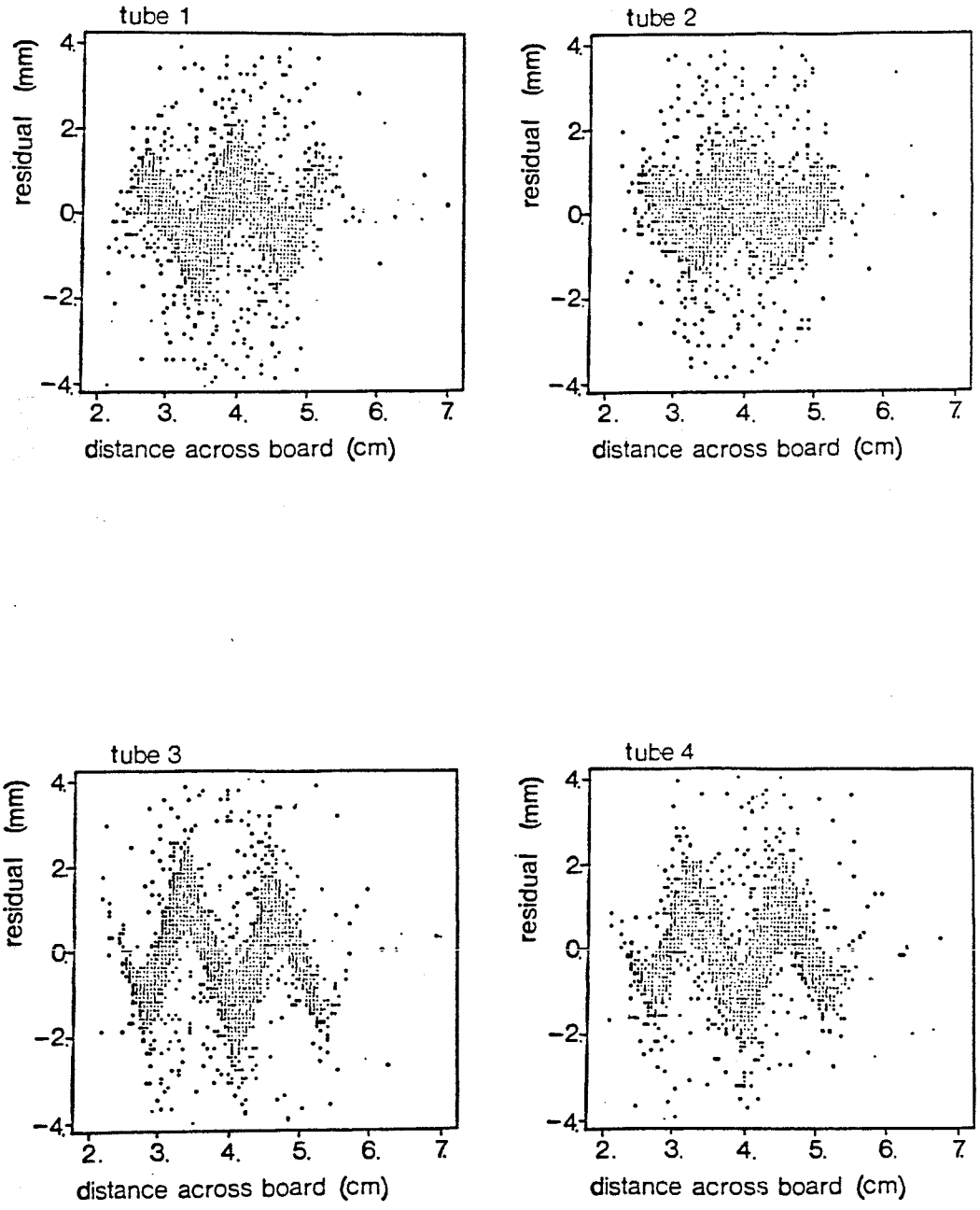

Figure 42: Residuals for the four chambers in the Beam Tests

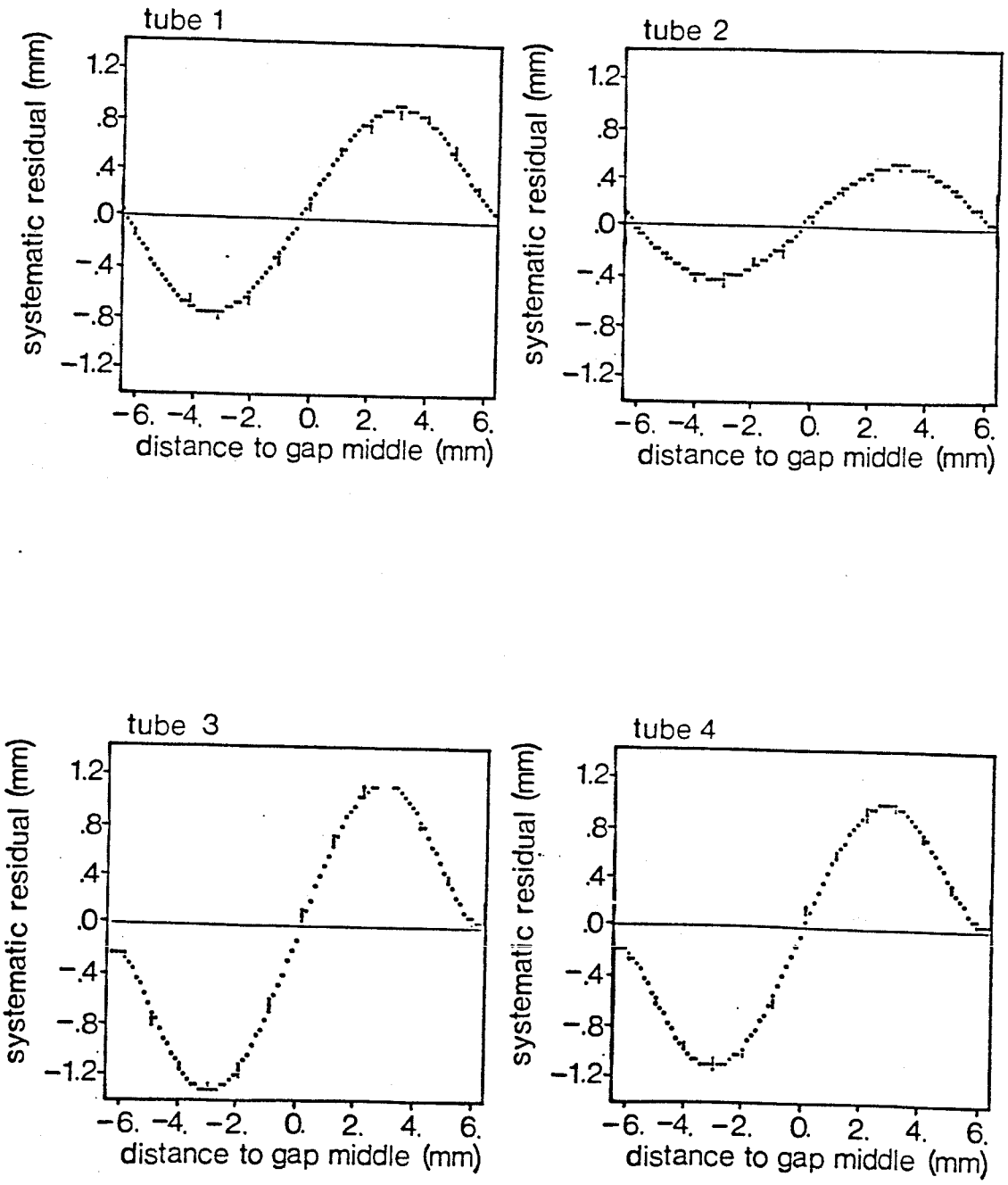

Figure 43: Residuals of the chambers against modulo strip width

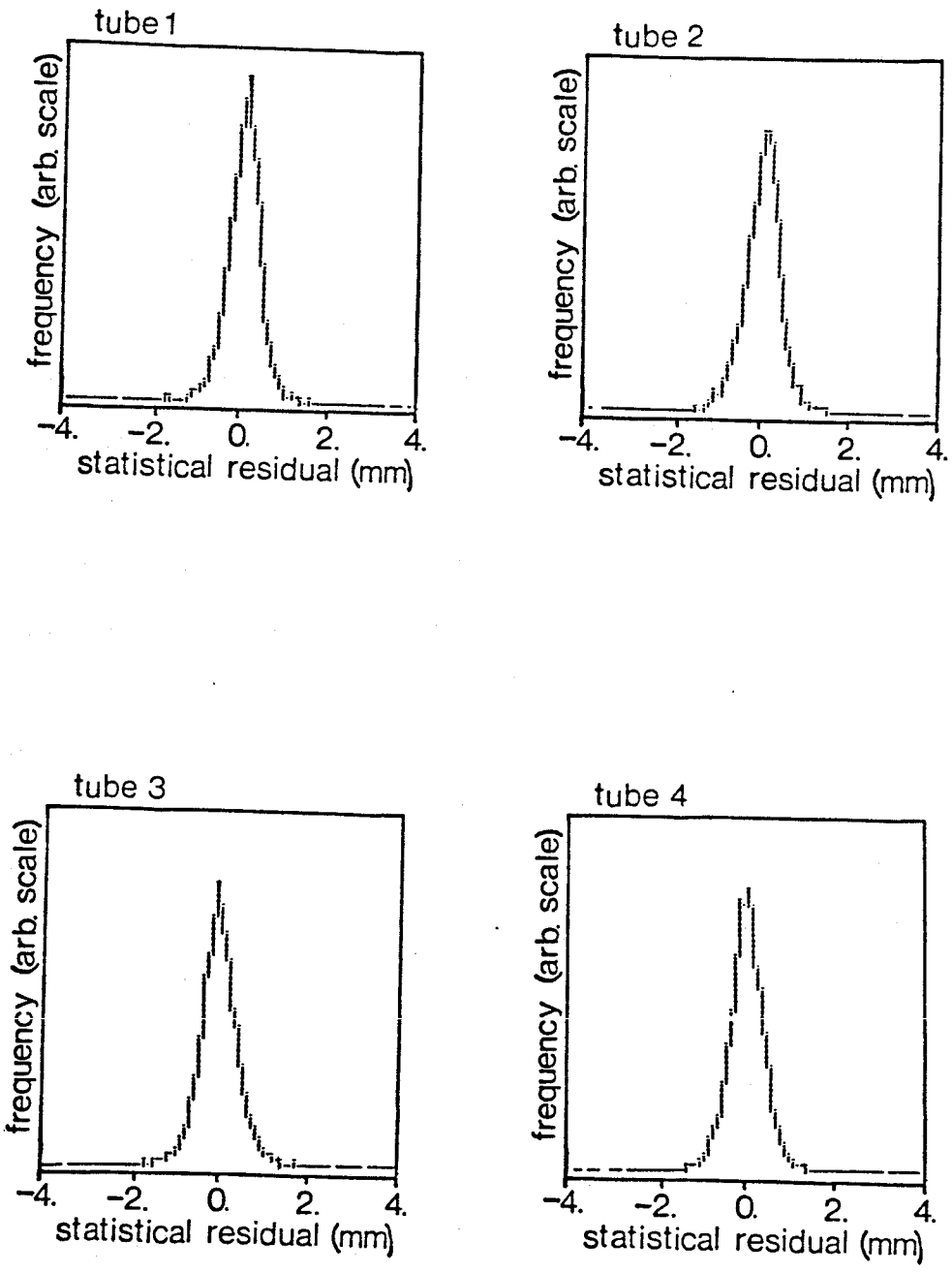

Figure 44: Final Residuals after removal of systematic error

during the 1984 run which has made it impossible to use the detectors in the muon track reconstruction. These problems were from gas leaks in the chambers, and also the difficulty found in mapping the magnetic field inside the iron. However the information from the detectors has been used during scanning on the MEGATEK interactive facility to validate the presence of muons. After more work on the Iarocci chambers, and careful measurements of the magnetic fields in the iron walls, it is hoped that the 1985 data will be more useful. The new chambers will improve the momentum resolution and also reject some of the background in the muon analysis from decays in flight of $\pi^{\pm}$'s and $K^{\pm}$'s.

It is planned to combine the information from the Iarocci tubes and the outer drift chambers in the first level trigger (described in the previous chapter). In order to give a signal to the trigger in the short time available between beam crossings, one would be forced to use the hits on the wires rather than the digitised charges on the strips from the multiplexed ADC. The wires can be read out in groups of 32, so that coincidences between planes would define the muon position to an area of $(32\ \mathrm{cm})^2$ in space. One possible way to use these signals would be to put them in coincidence with candidate tracks from the outer muon drift chambers. This is similar to the present use of the signals from the backstacks of the hadron calorimeter but the Iarocci signals define a smaller area in space and so would give a finer pointing requirement to the trigger, and be better in resolving ambiguities from multiple hits in the outer chambers.

Iarocci tubes have the advantage of being an economical way to instrument large areas of a detector with reasonable resolution. This chapter has discussed the author's work on the preliminary investigations of these tubes for UA1. Their resolution is found to be dominated by systematic effects arising from the chamber geometry, which has been reproduced in simple Monte Carlos. This systematic error, of the order of several hundred microns, can be parameterised and in the final system cosmic ray data will be used to map the error as a function of chamber position.

5. JET ANALYSIS

Jets were first seen in electron-positron collisions when the energy of an outgoing fermion exceeded about 7 GeV [40], by contrast measurements at the ISR at $\sqrt{s}$ = 63 GeV did not show convincing evidence for simple jets. In hadron collisions the colliding particles are a conglomerate of quarks and gluons (called partons) amongst which the energy of the beam is shared. It was only at the higher energies met at the collider ($\sqrt{s}$ = 546 GeV) that the first simple jet-like structures were observed from hadron colliders [41]. These jets are mainly the result of the fragmentation of partons from hard QCD processes, but it is possible to see jets from quarks which originate from the decay of bound states, such as the IVBs, or heavy quark-antiquark systems. The cross-section for the production of these resonances is always small, and contributes a negligible fraction of the jet data presented in this chapter.

Once the visual recognition of jets has been established, one needs an algorithm to analyse the large amount of data. The border-line between an obvious jet with a high transverse energy and a weak correlation of a random fluctuation of particles in space is not well defined, and at low energies, (below around 8 GeV) the definition of a jet will depend heavily on parameters in an algorithm. The UA1 jet algorithm described below, has been checked by visual scanning of selected events on the MEGATEK offline display and also compared to an independent algorithm [42]. It appears to produce unambiguous results for jets above 10 GeV in transverse energy.

5.1 The UA1 Jet Algorithm

The coordinate system used in jet finding is not (x,y,z) space because the distribution of tracks with respect to polar angle is not flat for minimum bias data. Instead the variables which are chosen are the angle, ϕ, around the beam, and the rapidity,

$$y = 0.5 \ln\{(E+p_\ell)/(E-p_\ell)\}, \qquad 5.1.1$$

where E is the energy of the particle and p_ℓ its momentum component along the beam-axis. In the limit of massless particles this reduces to the pseudo-rapidity,

$$\eta = -\ln\{\tan(\theta/2)\}. \qquad 5.1.2$$

Differences in η and ϕ are invariant under boosts along the beam axis, and the distributions of tracks in these quantities are flat in the central region of the detector. One can then say that deviations from the flat background in these variables must be due to something other than phase space.

The jet algorithm is used to find jets with either the calorimeter data or the tracks in the central detector. Both methods are based on the same concepts but a fundamental difference between them is that the central detector records charged particles only, whereas the calorimeters will also find neutrals. As most tracks are pions then one would expect a neutral/charge fraction of 0.5 from a simple counting rule. By using the information of the charged momenta in the CD and the total energy in the calorimetry it has been found [42] that the value is much larger, nearer 1.5, in disagreement with most current fragmentation models (the most recent measurement is 1.22 [43]). The measured value may be high due to a bias in the jet trigger, which only uses the information from the calorimeter.

The jet algorithm in the calorimeters first orders the 462 cells in the C's, I's, gondolas and bouchons into decreasing magnitude of transverse energy, E_t. Cells above 2.5 GeV in E_t are added vectorially to those which are closest in (η,ϕ) space to form clusters, if

$$R < 1, \text{ where } R^2 = (\Delta\eta)^2 + (\Delta\phi)^2. \qquad 5.1.3$$

If there are no clusters within $R < 1$ then a new cluster is initiated. Cells with an E_t below 2.5 GeV are finally added to the nearest cluster in (η,ϕ) space if they have a value of R less than 1 with respect to that jet. The cut at $R = 1$ is justified by the plot in figure 45, this range of R corresponds to the limit of correlation. This cut also differentiates between tracks from the beam fragments and the jet, because at large rapidities $\Delta\eta \approx p_t^j/p_t^b$, where p_t^j and p_t^b are the components of the track momentum between the jet and beam respectively.

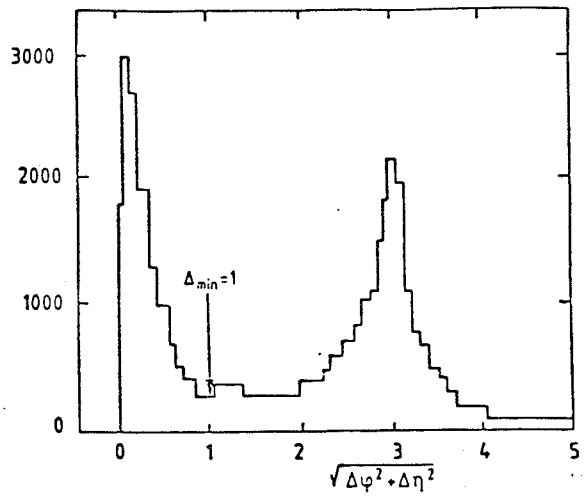

Figure 45: Distribution of Cells (E_t > 2.5) in R

The algorithm in the central detector works in the same way, taking tracks instead of cells. However instead of a cut of E_t > 2.5 GeV, a transverse momentum cut of p_t > 1.5 GeV/c is used. Examples of jets found in the detector by the algorithm are shown in figure 46.

5.2 Single Jets, A Test of the Algorithm

Continuing from some earlier work [44] with data taken in late 1982, it appeared that the jet algorithm was finding events with single jets. Collider jets usually arise by the scattering of partons from a hadron. Although the longitudinal fraction of momentum of a parton can vary greatly, the vector sum of the transverse momentum of partons should be small in events with two or more jets. This means that in multi-jet events, the transverse momentum of the jets should be balanced in the laboratory frame.

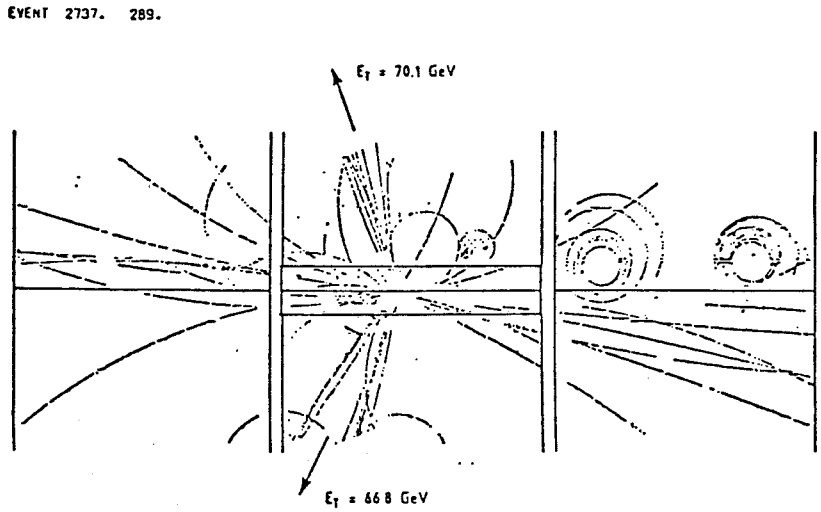

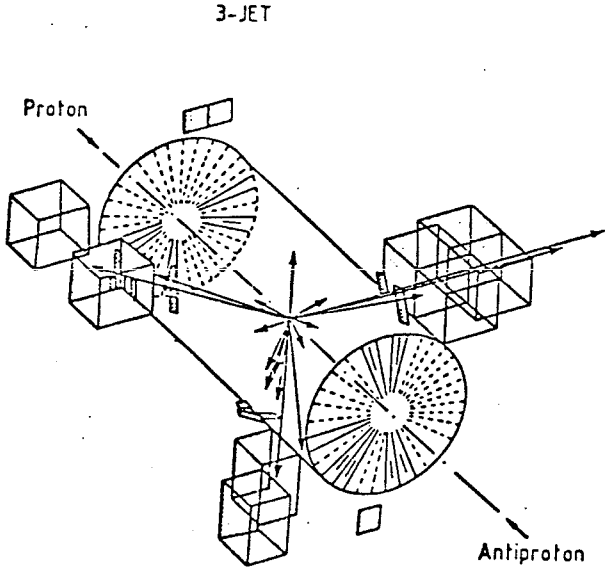

Figure 46: Examples of jet events in UA1

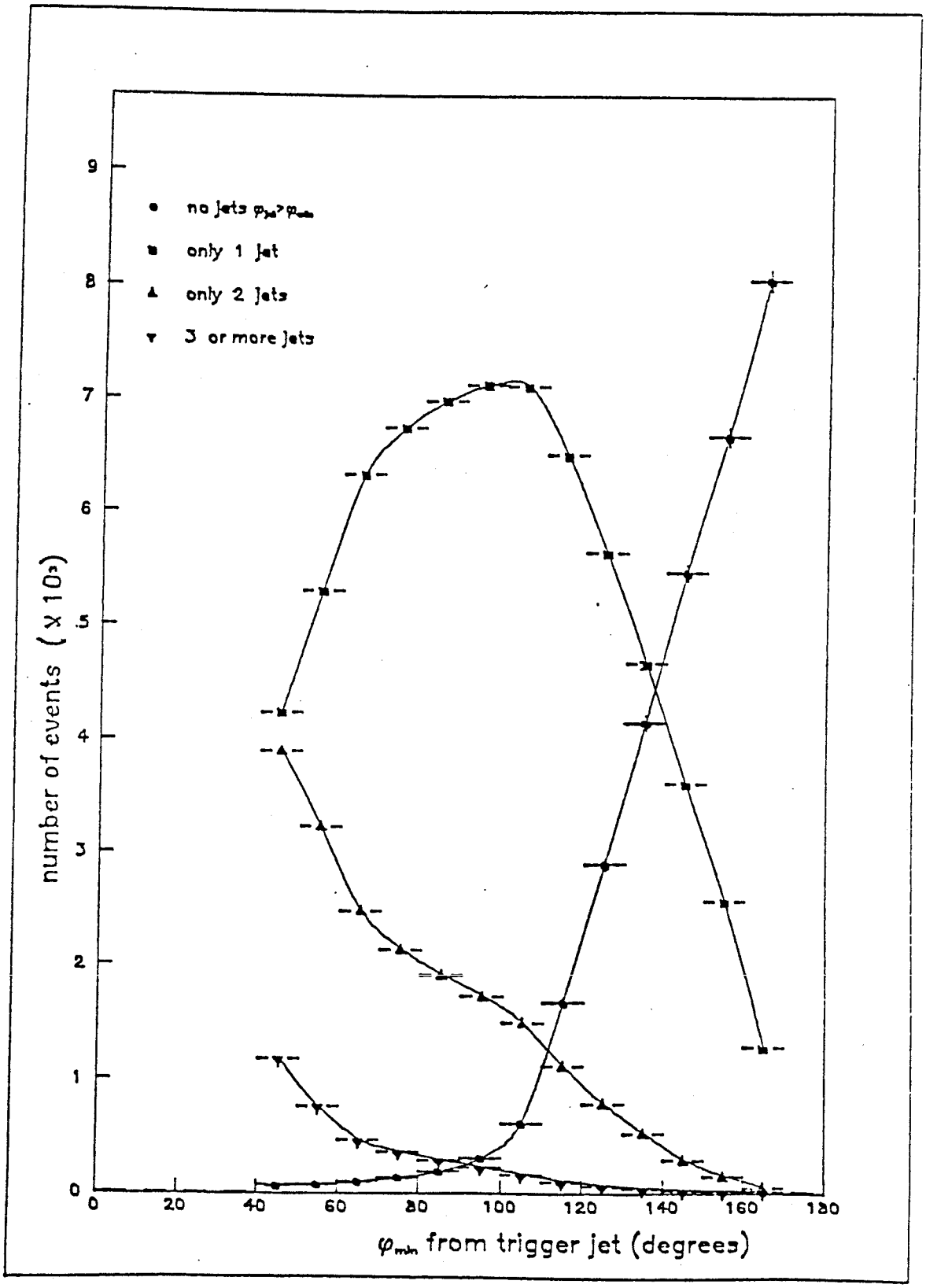

Figure 47: Number of jets opposite largest jet

In figure 47 we show the number of events where there are 0, 1, 2, 3 or more jets at an angle greater than ϕ_{min} away from the trigger jet. A large fraction of the events are simple two-jet events, and the number of events with no jets in the opposite direction increases rapidly as the wedge in ϕ is decreased. The number of events with single jets is not zero when the wedge is large ($\cong$60 degrees), implying that these single jet events are accounting for 3% of all jet events. These single jet events cannot be explained by simple parton scattering but may be due to either inefficiencies in the jet algorithm, experimental bias or conceivably due to physics processes which have a smaller cross-section than the strong interaction.

The method adopted to investigate single jet events was to apply fiducial cuts to events until one was left with a reasonable number which could be scanned on the MEGATEK. The cuts applied are in table 10.

Table 10: Cuts for the jet selection

(1)	Only one jet reconstructed by the algorithm ($E_t > 5$ Gev).	
(2)	Jet $E_t > 30$ GeV.	
(3)	$\|\phi\| < 75$ degrees or $\|\phi\| > 105$ degrees .	
(4)	$\|\eta\| < 0.5$	
(5)	$\frac{\|EM - HA\|}{\|EM + HA\|} < 0.8$	EM electromagnetic energy in jet HA hadronic energy in jet

Cut (1) selects all events with only one jet in the event. Cut (2) selects events with a reasonable transverse energy, this helps to rule out events where one jet of a two jet system has been lost down the beam pipe. Cut (3) rules out cases where a jet or part of a jet was lost in the vertical region where there is a gap in the gondolas and C's for readout cables. Cut (4) combined with cut (2) gives a strong

indication that the jet has not been lost in the beam pipe. A jet in the pipe which would balance a jet with an E_t of 30 GeV at 90 degrees would need over 340 GeV of energy if it were not to strike any part of the bouchons. However the available energy per parton cannot be greater than 270 GeV. Finally cut (5) is one which removes hits in the hadron calorimeter which arise from cosmic rays, or more likely, halo particles which arise from beam-pipe interactions further down the tunnel, and travel in a direction which is parallel to the pipe. This cut also removes an ambiguity in the gondolas arising when there are multiple hits in one gondola and the readouts from the four PM's are insufficient to calculate the x,y,z and energy for each hit.

Although the above (5) represent the final cuts imposed on the data each cut was arrived at by different methods as they represent different limitations of the acceptance of the apparatus. Using a loose selection from the 21 nb^{-1} data sample from the 1982 run, the number of events left after each cut is listed in table 11.

These events were then traced back to the processed tapes and copied to the CERN MERLIN VAX computer in order to see them on MEGATEK display. The following was found for each event:

1. run 2689 event 399

   A cosmic muon which struck a BBQ light guide causing a large apparent energy in the gondolas.

2. run 2691 event 324

   A clear two jet event where the second jet was in the bouchons but not found in the algorithm due to a dead wire in the position detector in the bouchons.

3. run 2844 event 1056

   The energy of the single jet was overestimated due to multiple hits in the gondolas, hence bad energy reconstruction.

4. run 3582 event 121

Table 11: Numbers of events passing cuts

Total number in sample	44232
Number with at least one jet	40427
No other jet E_t > 5 GeV	3096
Single jet with E_t > 30 GeV	296
ϕ not within 15 degrees of vertical	273
$\|\eta\|$ < 0.5	95
$\|(EM-HA)/(EM+HA)\|$ < 0.8	8

Table 12: Event Summary

run	event	missing energy			jet vector			
		E_t	ϕ	η	E_t	ϕ	η	$\frac{\|EM-HA\|}{\|EM+HA\|}$
2689	399	31.1	110	−0.50	32.7	−72	0.12	0.02
2691	324	11.3	147	1.49	34.0	−22	0.47	−0.01
2844	1056	19.3	−19	2.65	31.7	−159	0.21	0.70
3582	121	25.8	−38	1.31	34.6	141	−0.14	−0.09
3775	634	12.8	−140	2.88	30.6	18	−0.03	−0.05
3883	736	15.8	−141	2.05	31.8	18	0.08	0.70
3890	1240	22.1	10	2.50	30.6	−158	0.09	0.73
4071	1205	17.7	−165	2.26	31.5	10	0.05	−0.01

Similar to (1) but a noisy wire in the position detector had resulted in a bad reconstruction of position and energy.

5. run 3775 event 634

   A potential mono-jet were it not for the fact that the central detector was not working fully.

6. run 3843 event 736

   Similar to (3)

7. run 3890 event 1240

   A dead PM in the gondolas had led to bad energy reconstruction for the jet in the algorithm.

8. run 4071 event 1205

   Similar to (1) except that a track in the central detector passes close to the edge of the bouchons and probably goes through a gap so that no energy was deposited in the scintillator.

From the results of jets being lost in the bouchons it was found that the jet algorithm substantiates the hit in a bouchon with a coincident hit in the position detector. However a noisy wire can give bad reconstruction as in (4) where the hit in the bouchon has been ignored by the jet algorithm. The coding in the position detector reconstruction program was therefore altered to accommodate for isolated wires.

The event which was a potential mono-jet was hampered with a dead region in the CD. The middle bottom (MB) chamber was off for the run 3775 and so no conclusion can be drawn, although it would be consistent with

$$W \rightarrow \tau + \bar{\nu}_{\tau}$$

followed by

$$\tau \rightarrow \text{hadron jet} + \nu_{\tau}. \qquad 5.2.1$$

From this study of single jets in the 1982 data we conclude that the large number of events with only one jet can be explained by the acceptance of the detector. The one event found which cannot be explained by this is consistent with the standard model, it may be the tau decay of the W. The jet algorithm appears to be well understood, and software cuts can be used to select a good jet sample.

5.3 Investigating Properties of the String Model

In chapter I we discussed two models for jet fragmentation, the string model and the Independent Fragmentation (IF) model. The models differ in the number of tracks one would expect to find between the jets and the beam fragments. Unfortunately at the time of this analysis there are no Monte Carlos available containing the string model. However we are able to put a limit on the excess of tracks by studying the data. To find the track densities near a jet, jets are reconstructed in the central detector and the track density is found in a slice of ϕ near the jet. This is compared to a background density assumed to come from fragments from the beam by finding the density of tracks at a different ϕ from the jet. As the jets cover a cone of order unity in R one needs to be at a large angle to the jet axis for a background estimate. A value of 90 degrees was chosen ($R = 1.57$) measured from the jet towards the side where the acceptance corrections in the drift chamber were closest to unity. As the wires lie along the z-axis in the central detector, the track acceptance in ϕ varies like figure 48 and so this was corrected for both angle and p_t. The variation with rapidity can be seen in figure 49 and is taken as constant over the central rapidity range of the detector ($|\eta| < 2$). The track acceptances were obtained from track distributions in jet events for different track p_t's and are normalised by assuming perfect track reconstruction in the best parts of the detector.

From the express line data from 1983 we have a total of 256 jets with an E_t above 35 GeV/c, and 192 jets with an E_t above 50 GeV/c in the rapidity range of ± 1.5. Figure 50 shows the density of tracks in rapidity in the small 10 degree slice of ϕ near the jet. To highlight any asymmetry the distributions have been folded so that a negative rapidity difference indicates that the track is on the side of the jet which is closest to the beam. Figure 51 shows the density of tracks away from the jet

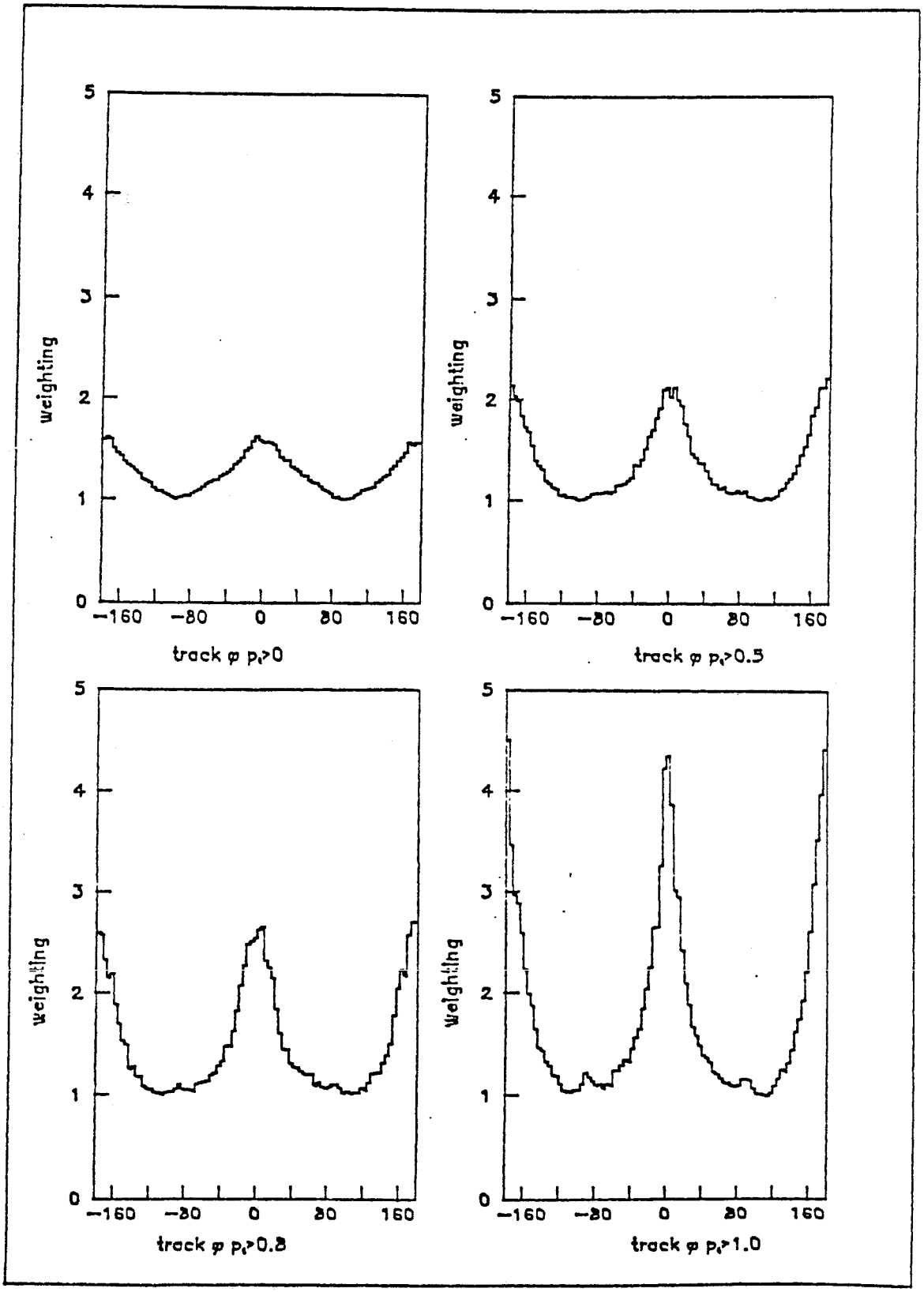

Figure 48: Central Detector Acceptance in ϕ

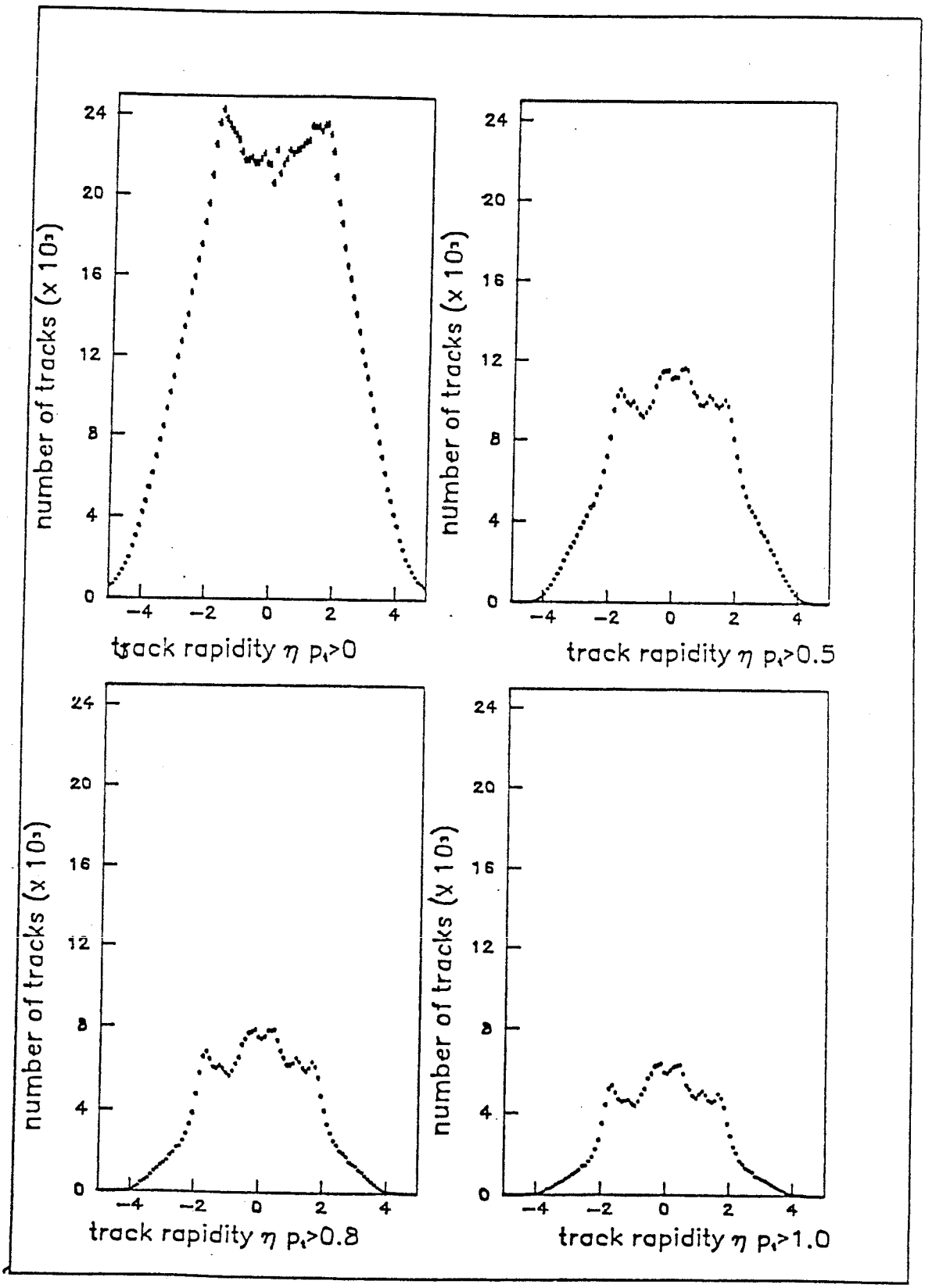

Figure 49: Rapidity Distribution in the Central Detector

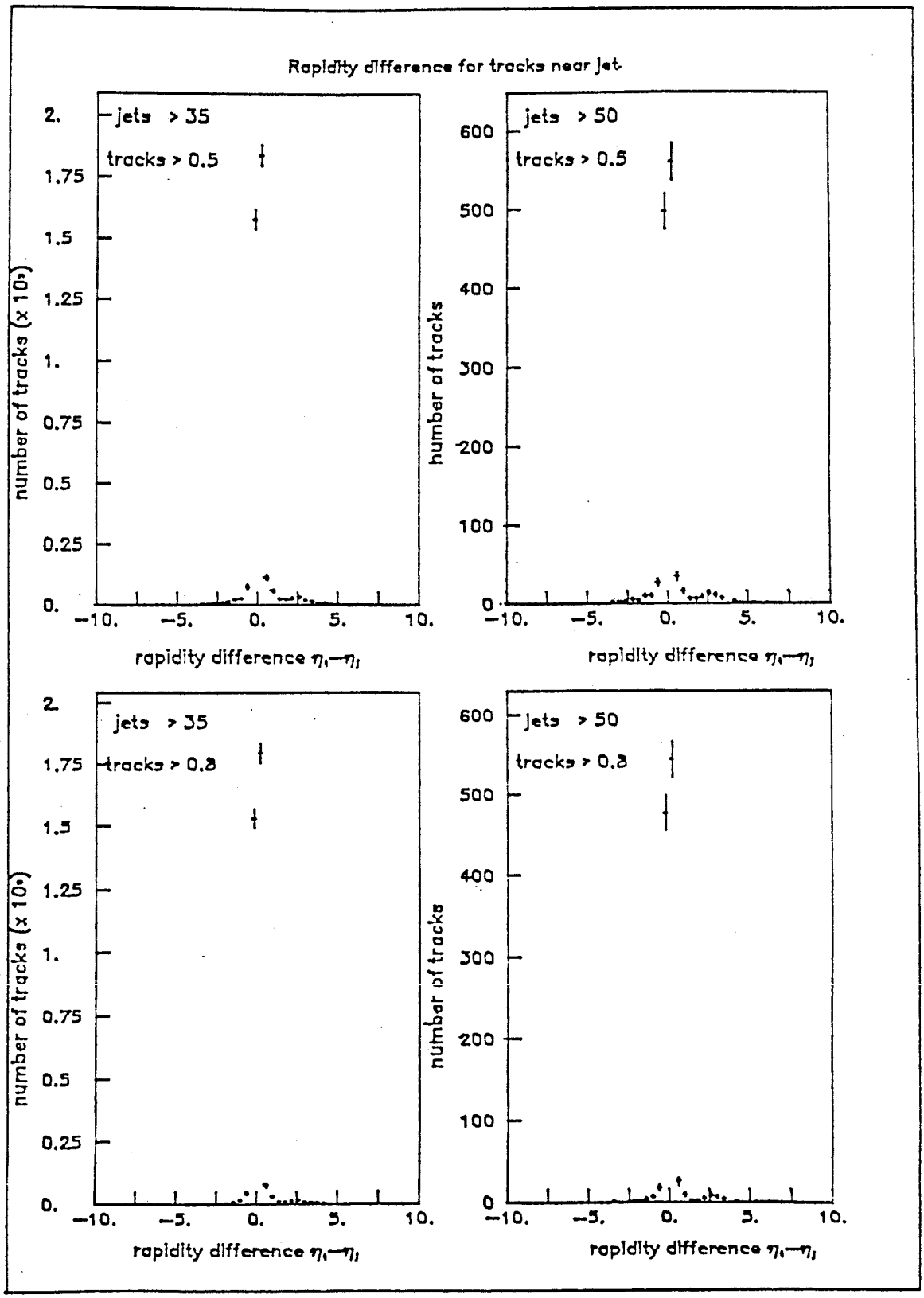

Figure 50: Distribution of tracks near jets

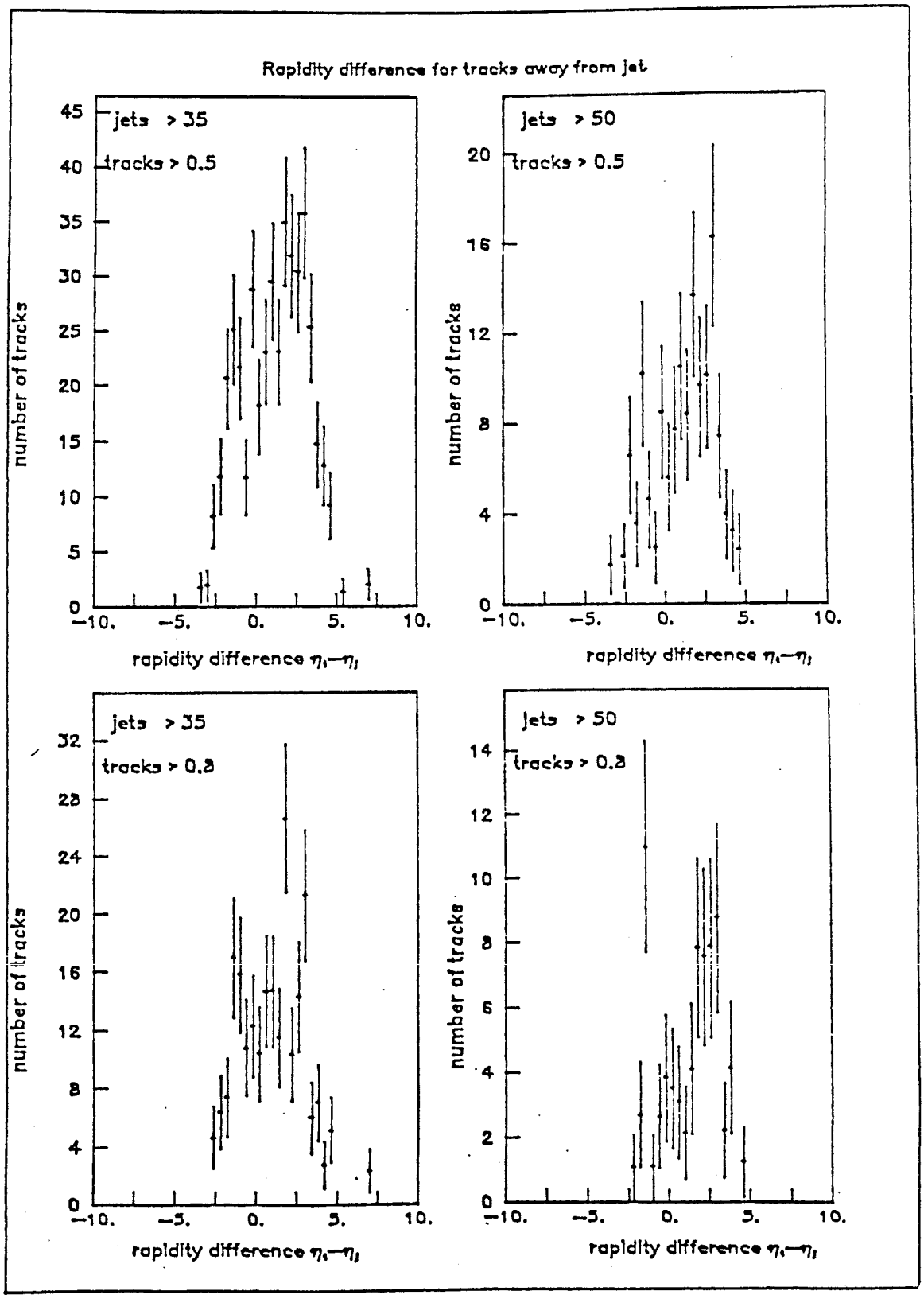

Figure 51: Distribution of tracks away from jets

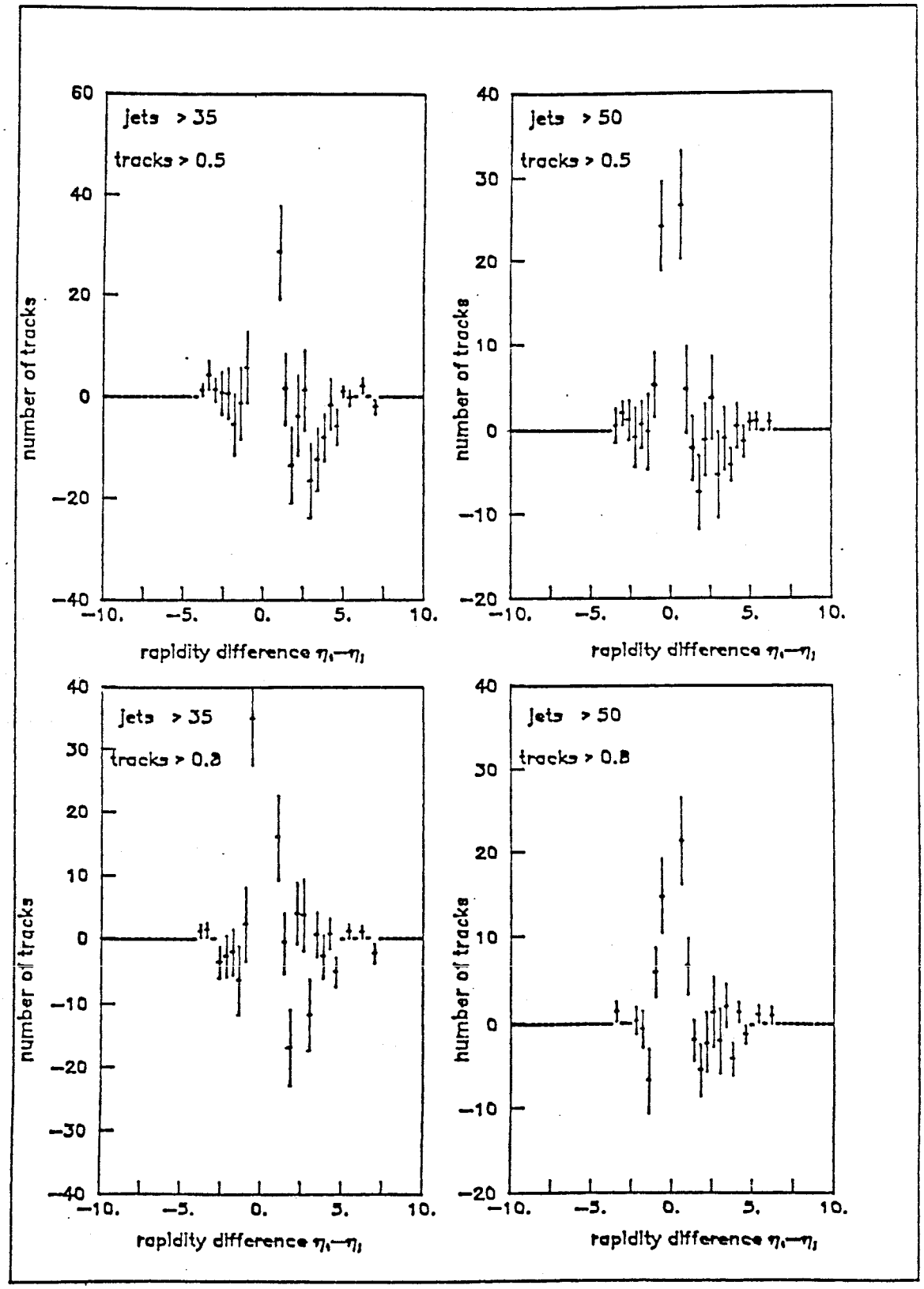

Figure 52: Difference between figures 50 and 51

axis for the same events which appear in figure 50, and figure 52 show the difference between figures 50 and 51. With the four groups of cuts on track p_t and jet E_t, one can see that the width of the jet is near 1.5 to 2.0 in R, consistent with R < 1, and the edge of the jet is well defined. The numbers of tracks per unit of rapidity per jet are presented in table 13.

Table 13: Track Densities near Jets

min jet E_t	35.	50.	35.	50.
min track p_t	0.5	0.5	0.8	0.8
density in jet	8.62	3.57	8.30	3.49
($dn/d\eta$ per jet)	±0.15	±0.11	±0.14	±0.11
density near jet	8.8	11.	−20.	1.7
($dn/d\eta$ per 1000 jets)	±22.	±19.	±12	±6.5

The densities inside the jets are for tracks with a rapidity difference of less than 0.8 and a ϕ of less than 10 degrees from the jet, and the densities near the jets are for tracks with a rapidity difference of between 2.0 and 3.2 from the jet in the direction closest to the beam. One can see that the jets above 35 GeV have 2.4 more tracks inside the jet than those at 50 GeV. For the lowest threshold ($E_t^{jet} > 35$ GeV, $p_t^{track} > 0.5$ GeV/c) the excess of tracks between the jet and the beam is less than 1.5×10^{-4} tracks per jet per unit rapidity per radian (2 s.d) at 2.8 units of rapidity from the jet, and is consistent with zero. Recent work has enabled the use of a Monte Carlo based on the string model [49], and it is hoped that this will be used to compare to the experimental value obtained in this study.

5.4 Shapes of Jets

Once the presence of jets has been accepted then there are many properties which can be investigated, especially within a hybrid detector such as UA1. Following from the idea of the distribution of tracks within jets, is the concept that the distribution of tracks can possess some shape with respect to the jet axis. Up until now the jets been considered to be symmetrical about the jet axis, but it easy to imagine the case where two jets close in (η,ϕ) have not been separated by the algorithm. This case may arise, for instance, from final state gluon bremsstrahlung. Another case where the jet shape may be important is in jets containing heavy quarks, these types of jets are expected to be broader due to the mass of the decaying particle.

5.5 A Shape Algorithm

The shape of the jet can be seen by taking a transverse section through the calorimeter jet axis and seeing where the tracks in the central drift chamber intersect the plane. Working in the usual (η,ϕ) space, it is possible to find the major and minor axes for the distribution of the tracks around the axis, as well as the angle α of the major axis to the UA1 coordinate system. To calculate these quantities, we define the angle θ_i between the plane containing the jet and the beam, and the plane containing the jet and the i'th track. In (η,ϕ) space this is simply $\theta_i = \tan^{-1}\{(\phi_j-\phi_t)/(\eta_j-\eta_t)\}$. The angle α is defined by maximising the value of

$$\Sigma w_i^2\cos^2(\theta_i+\alpha)-\Sigma w_i^2\sin^2(\theta_i+\alpha), \qquad 5.5.1$$

with respect to α. The value of w_i is a weighting parameter containing some information about the importance of the track, like p_t or distance in R from the jet, and is investigated in the next section.

It is easy to show that α is defined by equation 5.5.1 and is equal to

$$\frac{\sin 2\alpha}{\cos 2\alpha} = \frac{-\Sigma w_i^2\sin 2\theta_i}{\Sigma w_i^2\cos 2\theta_i}, \qquad 5.5.2$$

and the magnitudes of the major and minor axes with respect to α are

$$\Sigma w_i^2 \cos^2(\theta_i + \alpha) \text{ and } \Sigma w_i^2 \sin^2(\theta_i + \alpha). \qquad 5.5.3$$

For a data sample, the 1983 express line data was taken and the jets in the calorimetry were reconstructed using the standard UA1 algorithm. Events were taken when they had only 2 jets above 20 GeV transverse energy in the rapidity range of ± 1.5. Due to the restrictions of the coverage of the calorimetry and the central detector, the events were rejected if either jet was within 22.5 degrees in ϕ of either the vertical or horizontal planes. The distribution of tracks in R around each of these jets is shown in figure 53, which can be compared to figure 45.

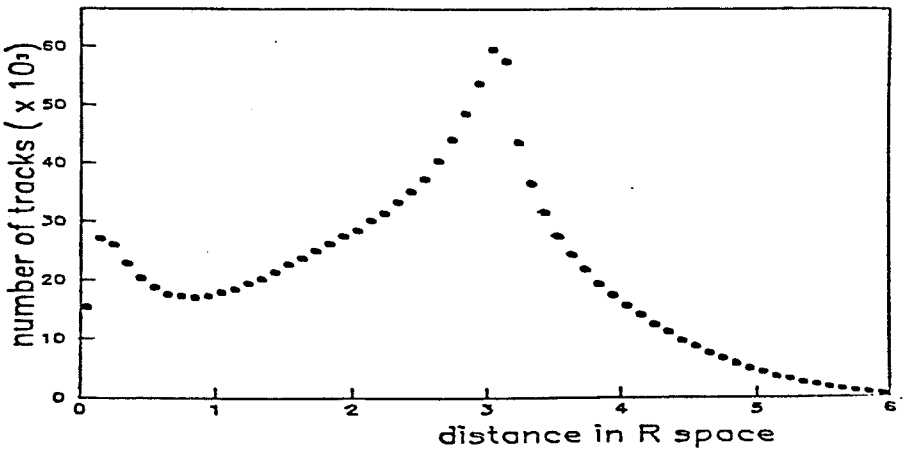

Figure 53: Distance of tracks in R from jet (no p_t cut)

The linear rise of the track density to $\pi/2$ with gradual fall off can be explained by the presence of a uniform background of tracks belonging to the rest of the event. The distribution of a uniform set of tracks in (η,ϕ) space is shown in Figure 54 which is simply the Jacobian for Cylindrical Phase Space (CPS) in R, i.e. for $R \leq \pi$ the density, f(R) is

$$f(R) = 2\pi R \qquad 5.5.4$$

and for $R > \pi$

$$f(R) = 4R \arcsin(\pi/R) . \qquad 5.5.5$$

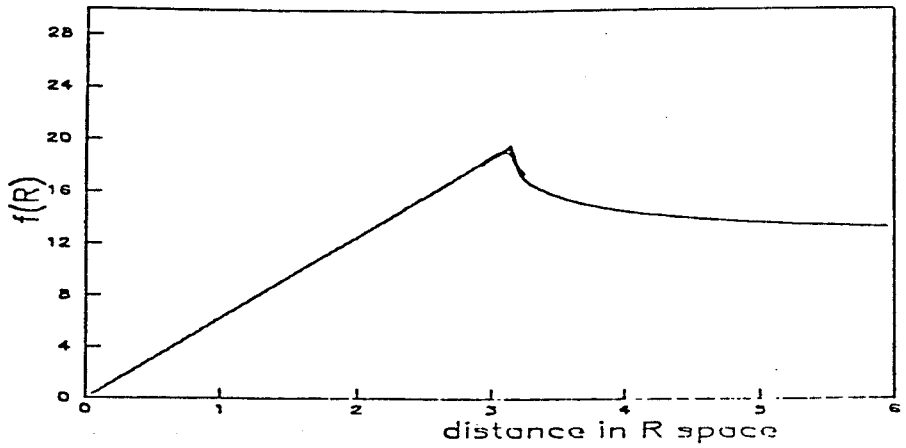

Figure 54: Jacobian for CPS in R

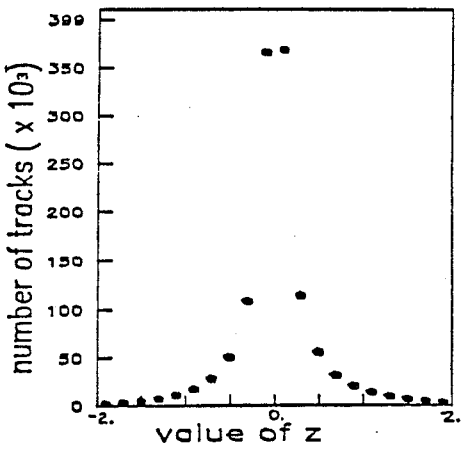

Figure 55: Fraction of longitudinal momentum of track in jet

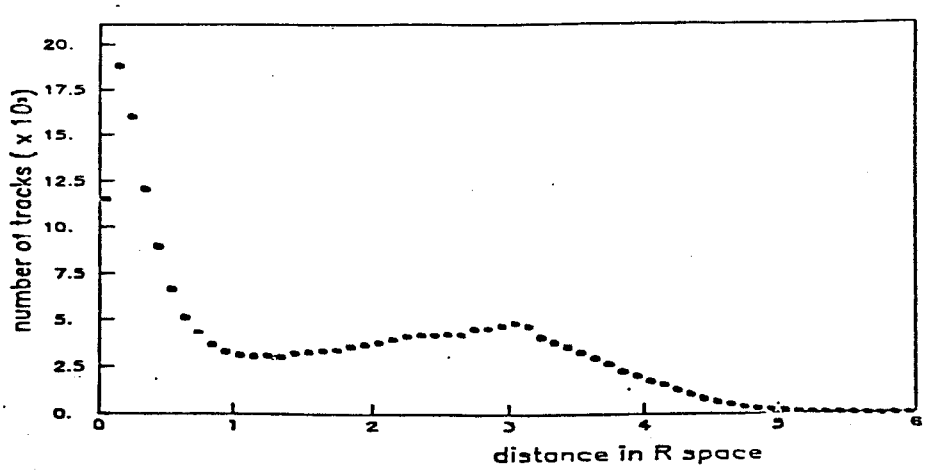

Figure 56: Final ΔR distribution

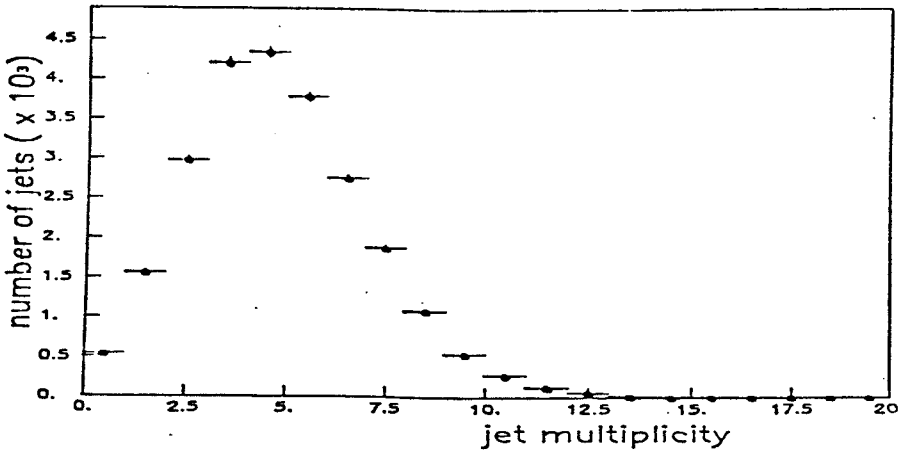

Figure 57: Distribution of charged track multiplicity in jets

In order to remove the CPS a cut was introduced in z, the tracks longitudinal momentum fraction of the jet at 0.05 (figure 55), giving the R distribution in figure 56.

The resulting track multiplicity for jets is shown in figure 57, on which a cut of 4 was placed, because the shape parameter is obviously not meaningful for jets with a low multiplicity. These cuts reduce the 1983 data sample to 4534 events, the invariant mass of the two jets can be seen in figure 58.

5.6 Results from the Shape Algorithm

The algorithm was run using three different types of values for w_i in equation 5.5.1.

a. Distance in (η,ϕ) space, R, between the track and jet.

b. Ratio of the track p_t and jet E_t, multiplied by R.

c. Momentum of the track multiplied by the sine of the angle between the jet and the track.

The resulting spectra of α are shown in figure 59. The peaks in α for (b) and (c) arise from the basic shape of jets in CPS space when using these variables. They can be attributed to the variables not being Lorentz covariant, whereas R is approximately covariant over large ranges in (η,ϕ) spacc. This effect forced the choice of the first weighting parameter, R, for the following analysis.

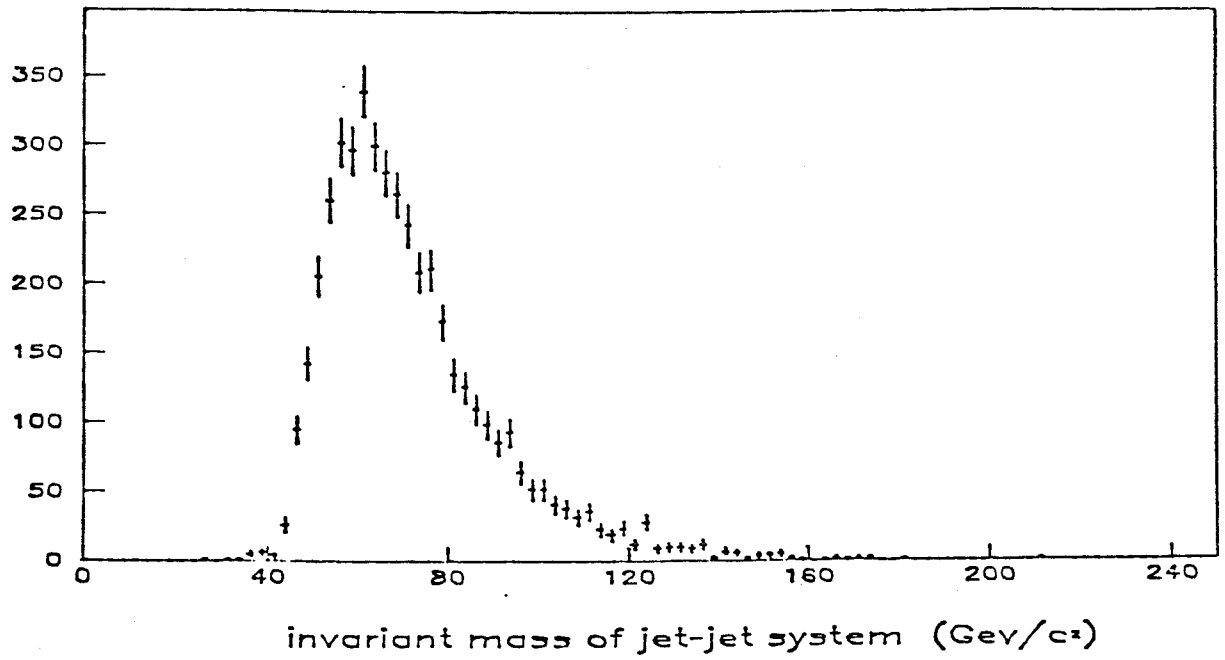

Figure 58: Invariant mass of the two jet events in selected sample

The distribution of α is uncorrelated in the jet transverse energy, rapidity, ϕ and multiplicity, as indicated in the plots in figure 60. The effect of the shape algorithm can be seen by the comparing the plots in 61. These show the tracks around the jet axis in the plane transverse to the jet axis in real space. The projections of these plots are shown in figure 62.

There is a slight excess of tracks on the right hand side of these plots as the jets all have positive rapidity, indicating that there is still a small contribution from beam fragments in the jets. This excess does not have a large affect on the value of α, the R.M.S. of the track distributions along the two axes parallel and perpendicular to the beam in the central region agree well, being 0.307 and 0.306. In figure 61 the tracks have been rotated by the angle α for each event so that the jets all have the widest dimension in the horizontal direction. Here the R.M.S. are different, as expected, being 0.387 and 0.196, indicating that not all jets are symmetric. One can now look at the magnitudes of the major and

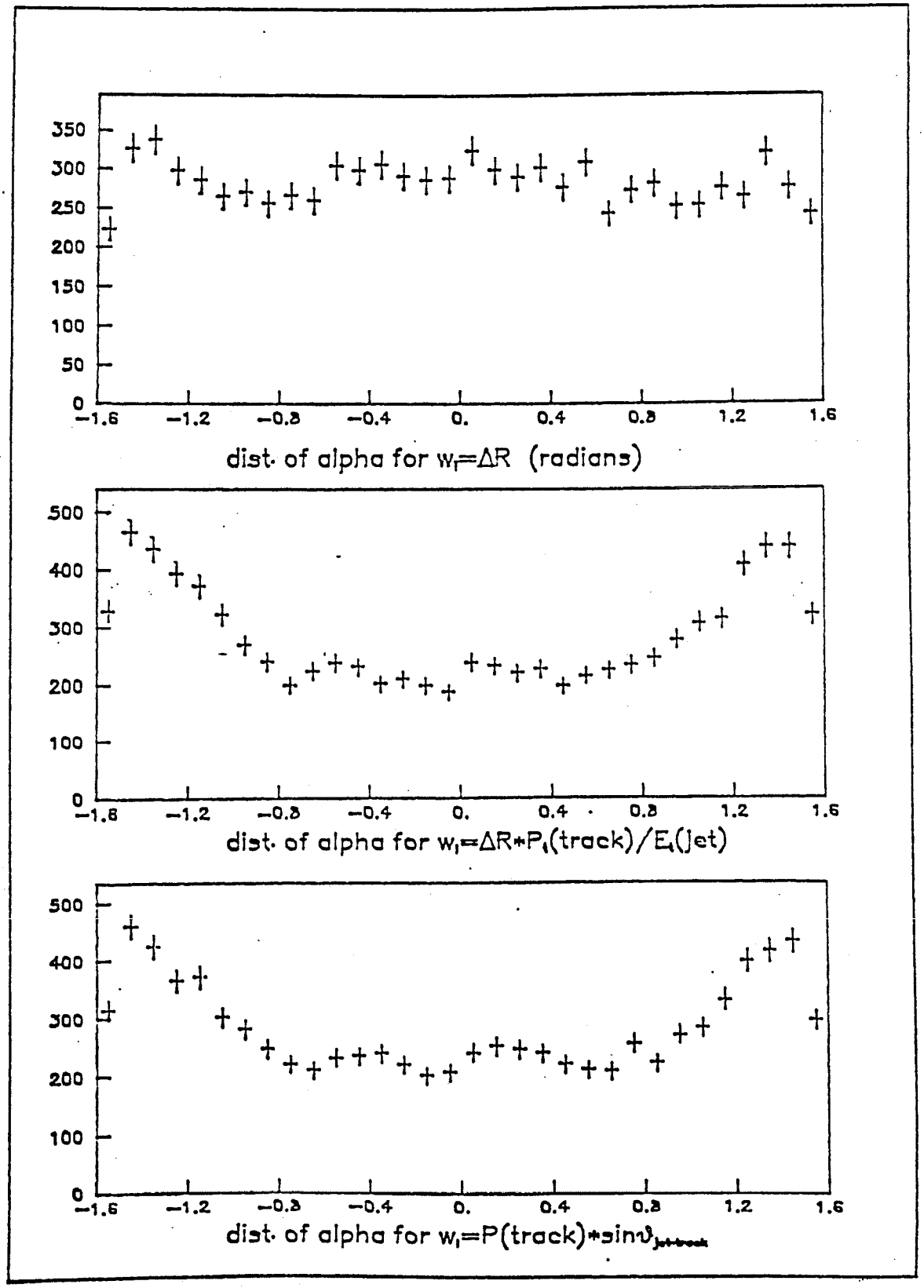

Figure 59: Distributions of α

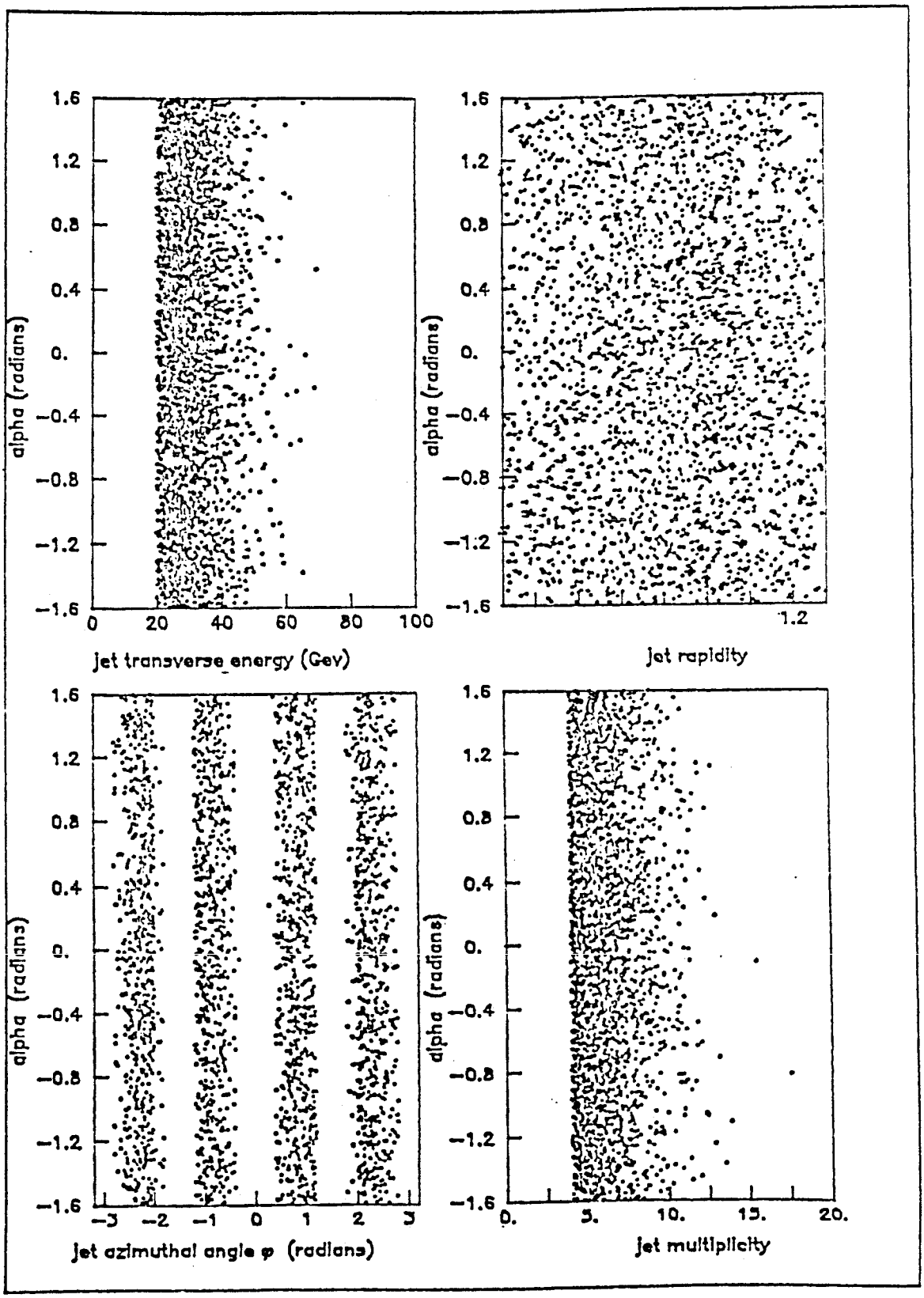

Figure 60: Variation of α with jet quantities

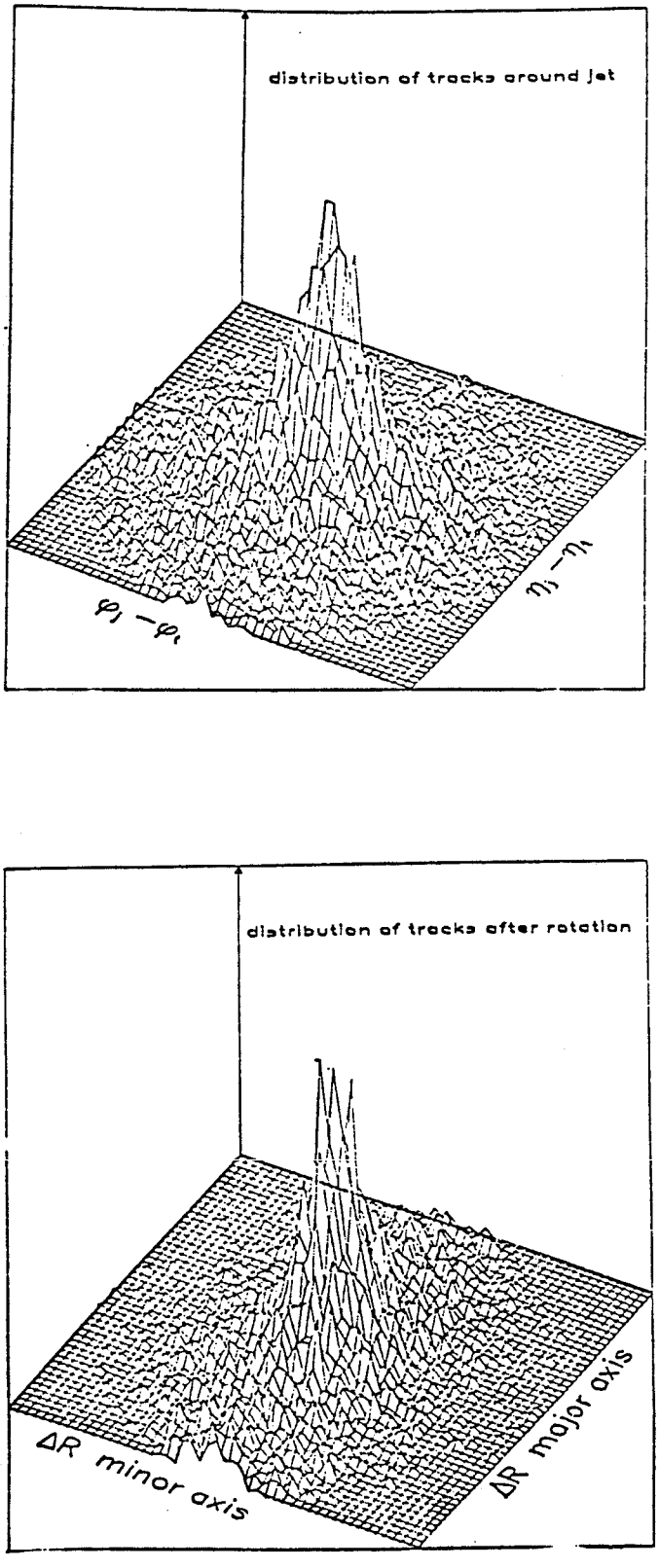

Figure 61: Distribution of Tracks in Jet

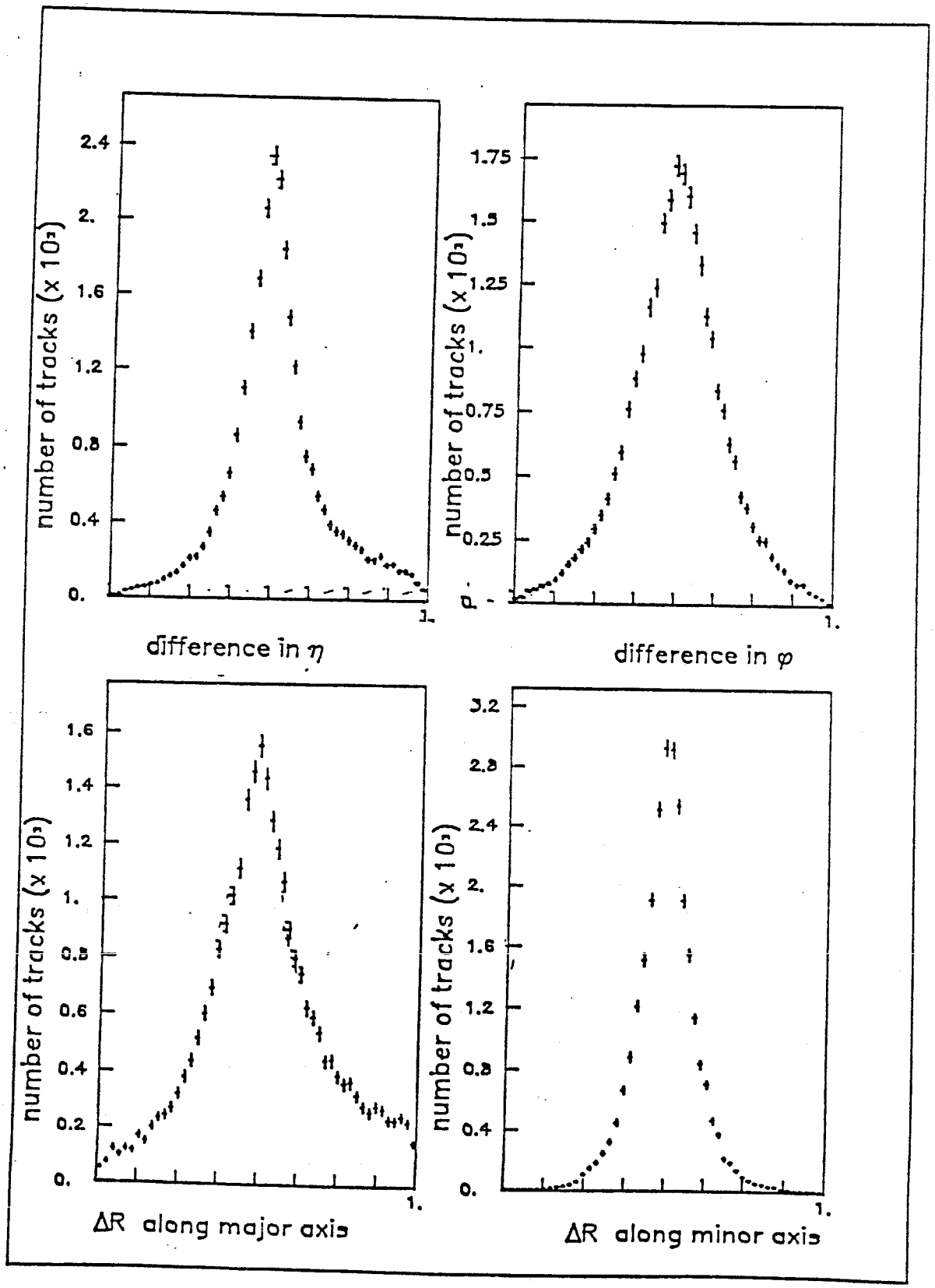

Figure 62: Projections of figure 61

minor axes as defined in equation 5.5.3 above. It is found that there is little variation with the multiplicity of the jet however there is a correlation between the ratios of major to minor axes with jet E_t. Table 14 show the data divided into 5 GeV transverse energy bins with the corresponding R.M.S. values of the major and minor axes. This shows that as jets increase in transverse energy then not only do the jets become smaller in R, but the ratio between the major and minor axes becomes more marked.

Table 14: Sizes of Major and Minor axes

transverse energy (GeV)	major axis R.M.S.	minor axis R.M.S.	ratio
20 – 25	71.1	30.9	2.30
25 – 30	62.2	24.0	2.59
30 – 35	57.6	21.8	2.64
35 – 40	59.1	18.8	3.14
40 – 45	51.8	15.9	3.26
45 – 50	58.8	16.9	3.48
55 – 60	47.7	13.6	3.51

As there are two jets in these events one can also look at any correlations between the angles and major and minor axes between jets. Figure 63 shows the two jet α's, and the projections along $\alpha_1 = \alpha_2$ and $\alpha_1 + \alpha_2 = 0$. Again no marked effect is seen, as with the plot of the α for the highest E_t jet, against the angle between the jet and beam in (η,ϕ) space. Defining the ellipticity as the ratio of the major and minor axes, then we can ask how the probability of the ellipticity of the lowest E_t jet being above a certain value E_0 varies with the ellipticity of the highest E_t jet. Figure 64 shows this, plotting the probability of the second jet having an ellipticity above 2, 7, 12, or 17, as a function of the ellipticity of the highest jet.

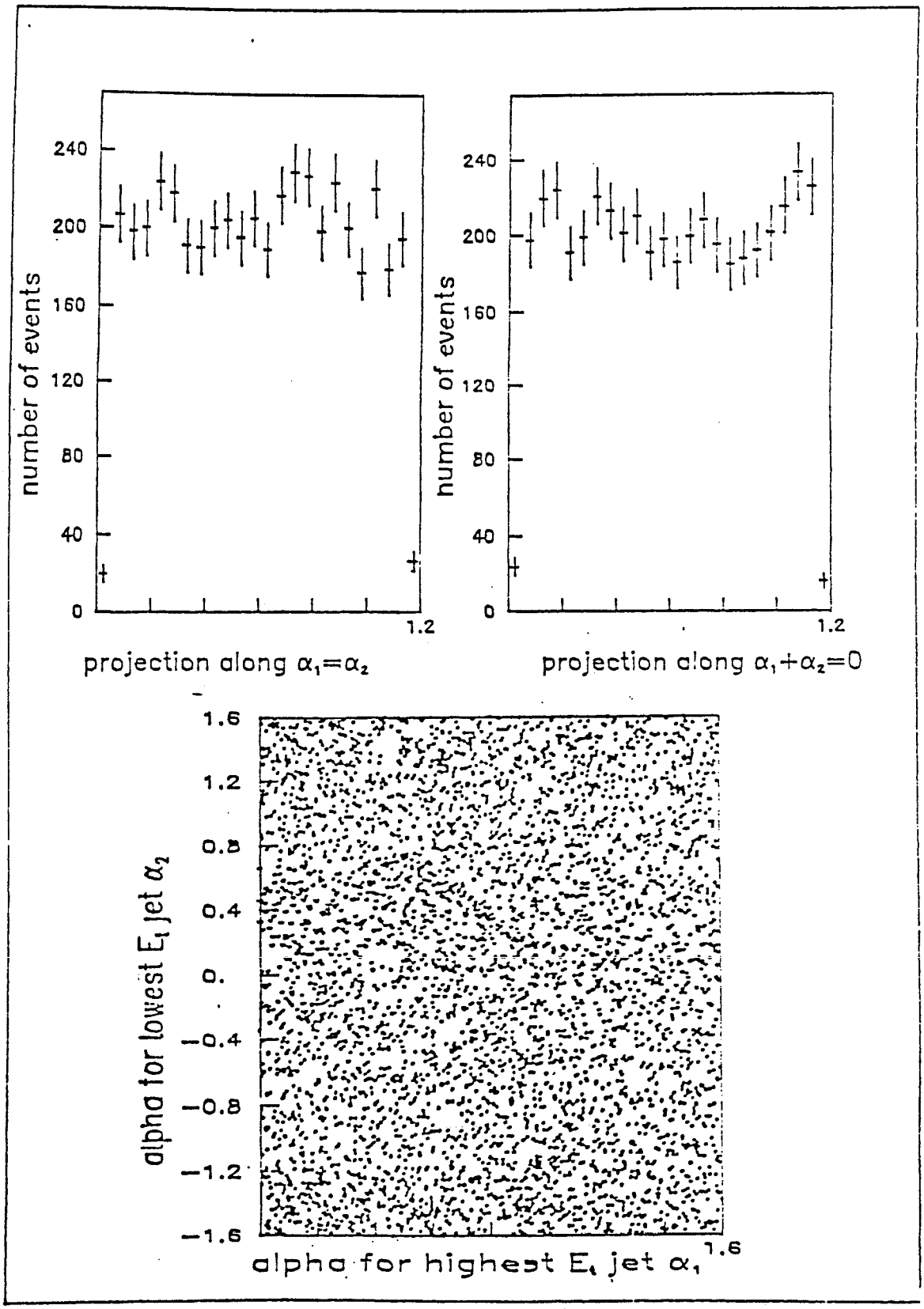

Figure 63: Comparison of the α's in Two Jet Events

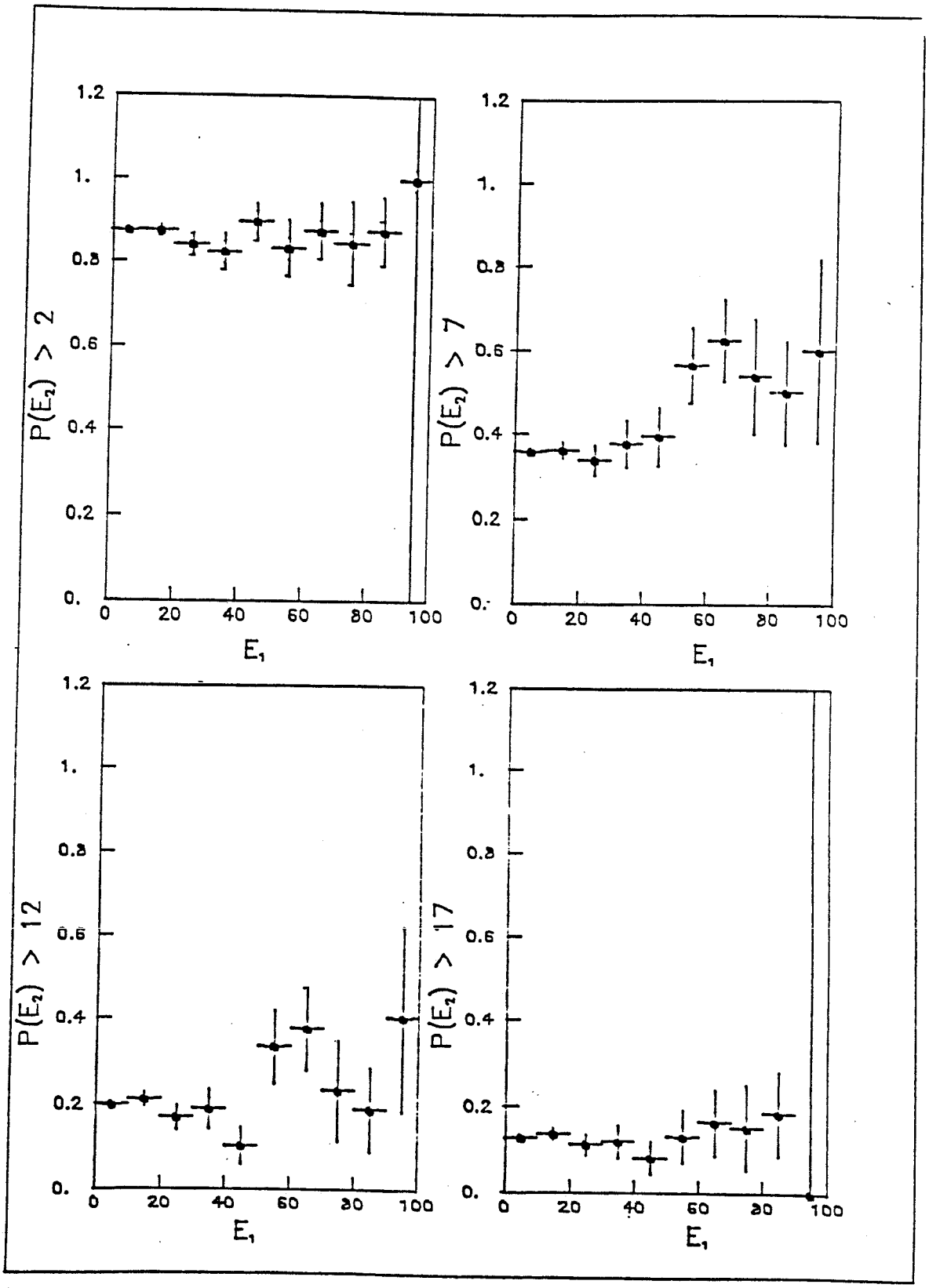

Figure 64: Comparison of Ellipticities in Two Jet Events

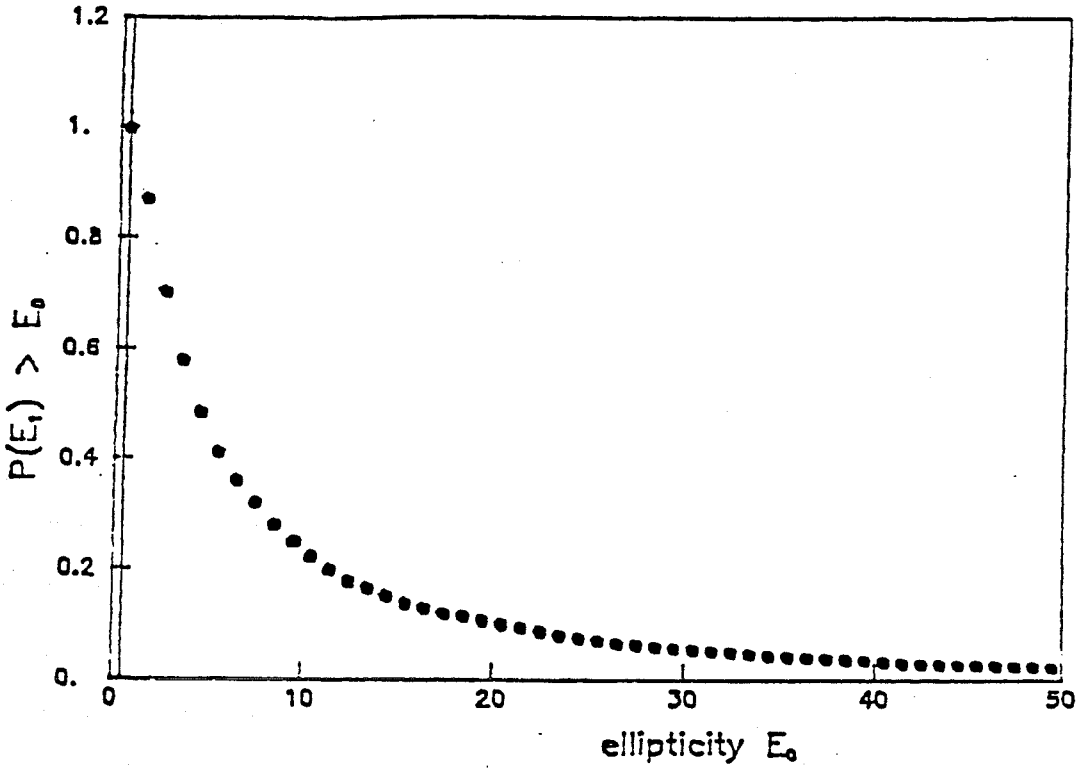

Figure 65: Probability of Jet Ellipticity

The probability does not vary greatly with the ellipticity of the highest E_t jet (within the statistical errors quoted), although a slight increase is expected due to the dependence of the ellipticity with E_t. Figure 65 shows the probability that a jet has an ellipticity greater then E_0, as a function of E_0. It is seen that the probability does not fall rapidly, the probability of a jet being greater than 10 is as much as 0.25.

5.7 Summary and Conclusions

In this chapter we have studied the properties of the jet algorithm in UA1. The occurrence of single jets in the 1982 data can be explained by inefficiencies in the apparatus, or from physics which has a small cross section, such as the tau decay channel of the W boson. The jet algorithm is well behaved and jet selection can be made by using software techniques rather than scanning. It should be noted

that in 1983 and 1984 this work was carried further at CERN with a much larger data sample. The result was the publication of a few events which had a single jet accompanied with missing energy [45]. These events may be attributable to production mechanisms in the standard model, such as the production of the top quark, or the neutrino decay of the Z^0. The small number of events has been used to put a limit on the cross-sections for supersymmetric phenomena where it is assumed that the missing energy arises from non-interacting particles such as the supersymmetric partners of the gluon and the photon.

We have then combined the information from the calorimetric definition of the jet, and the tracks in the central drift chamber, to get an idea of the jet shape and one can place a limit on the presence of tracks which one expects from the string model. The properties of jet shape are investigated and the jets appear to be elliptical, independent of the cuts imposed by the geometry of the apparatus. There is no correlation between the ellipticities of jets in two-jet events, and the ellipticity is found to increase with the transverse energy of the jet. Further work with comparison from Monte Carlo generation may prove that it is possible to use these ellipticities to identify final state gluon bremsstrahlung from the partons, improving the present algorithm where jets closer than unity in R are combined.

6. MUON-JET ANALYSIS

In chapter II, it was stressed that UA1 is a hybrid detector, making it a powerful tool for investigating the details of interaction products in the new energy regime at the collider. Here the energy available for producing particles is much higher than the rest masses of the known quarks and leptons, and interactions can produce events with particles of many different types. One interesting type of event is that with a single muon and one or more jets in the final state; analysis of such events makes use of the calorimetry, jet finding, and the muon detection. The presence of a single muon implies the presence of a particle which has decayed via the electroweak interaction, because muons do not couple to the strong interaction. Candidates from the standard model for the parent are the IVB's or quarks. If there is a jet in the event then the most likely production mechanism is the decay of quarks, because the cross-section for IVB production with a jet is small. In the case of QCD production of quark-antiquark pairs, the jet(s) in the event can arise from the other quark, from the hadronic products of the semi-leptonic decay, or from a gluon bremsstrahlung.

This chapter investigates the 234 nb^{-1} data sample from the 1984 muon-jet trigger. The original data sample was too great in size to scan, and the author was forced to use software techniques to remove sources of background. This data sample is shown to be rich in heavy $q\bar{q}$ pairs produced from QCD processes, however the light $q\bar{q}$ pairs give a large background in the form of muon decays of $\pi^{\pm}$'s and $K^{\pm}$'s, and the events must be removed as the momentum measurement of the muons is unreliable. We present the differential cross-section as a function of the muon p_t for muon-jet events, and by comparison with Monte Carlo, convert this to the total cross-section for heavy flavour at the collider.

6.1 Expectations from QCD

To compare the properties of the data to the predictions from QCD we have used the ISAJET Monte Carlo [46]. The main reason for this choice was the result of extra work in the UA1 collaboration

which has enabled the generated events to be processed through a UA1 detector simulation. This enables a direct comparison of the data with the Monte Carlo.

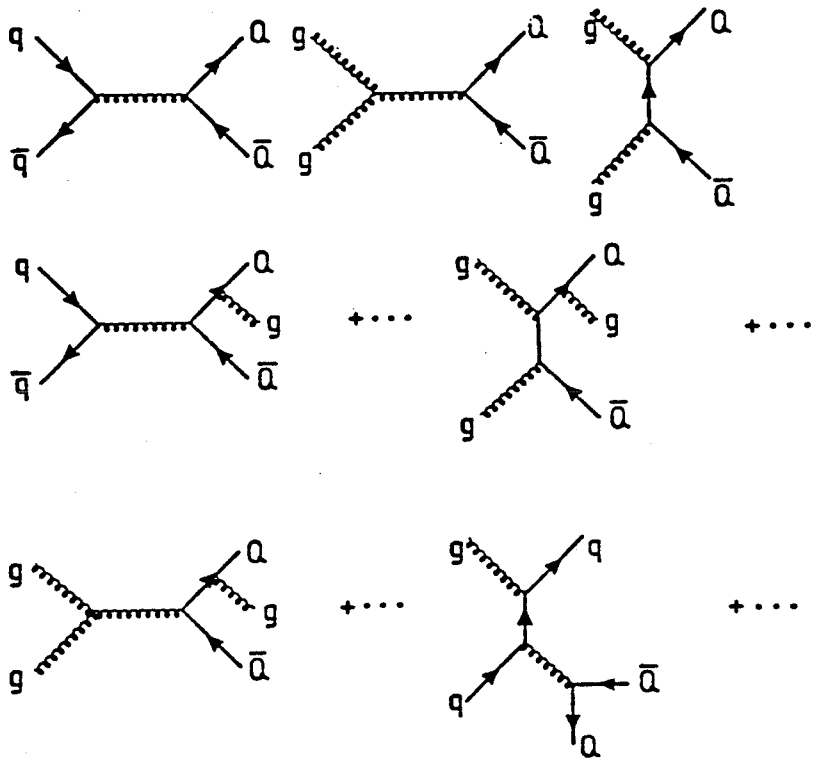

Figure 66: Lowest order diagrams for $q\bar{q}$ production

The ISAJET generator and subsequent simulation programs have been compared with data from the dimuon analysis [47] and the analysis of isolated high p_t leptons [48]. Overall, a good agreement has been found, indicating that for physics with low backgrounds, shapes of distributions can be predicted by the Monte Carlo. The object of this analysis was to compare not only the shapes, but also the absolute normalisations, testing the QCD predictions for the heavy $q\bar{q}$ pair production cross-sections.

The ISAJET generator was used to produce events containing lowest order QCD production of heavy quark pairs over the whole range of interest. The first and second order production mechanisms

for quark-antiquark pairs are shown in figure 66. The Monte Carlo uses the structure function of the proton parameterised by Eichten et al. [8] and the cross-sections are from the lowest order QCD processes as calculated by Combridge et al. [10] with $\Lambda = 0.2$ GeV. The partons are then evolved into jets using the leading log algorithm from Fox & Wolfram [11], and the jets hadronised by the Field & Feynman method [13]. The production of muons from electroweak decay of heavy flavour hadrons are calculated using standard V−A theory, with heavy quark fragmentation parameterised by Peterson et al. [12] (as described in chapter I).

The events were then processed through the detector simulation program, resulting in a total of 13,150 events which had a muon with a transverse momentum larger than 6.5 GeV/c. Events were generated with $q\bar{q}$ pairs with the initial transverse momenta (p_t^i) of the partons between 10 GeV/c and 90 GeV/c for charm, bottom and top quark pairs. In this study the mass of the top quark was assumed to be 40 GeV/c^2. The program which was used enabled the forcing of the muonic decay of the heavy quark, and so it was possible to produce the muon either from the primary decay of the quark (first generation) or to decay the quark hadronically and produce the muon from the daughter quark (second generation). The p_t^i ranges and integrated luminosities for the production are shown in table 15. Pilot tests showed that the probabilities for obtaining events in the luminosity of the 1984 run with $p_t^\mu > 7$ GeV/c and $E_t^{jet} > 10$ GeV were negligible for second generation $c\bar{c}$, third generation $t\bar{t}$, and for $q\bar{q}$ pairs with p_t^i outside the ranges shown in table 15.

These events were then selected with identical cuts to those applied to the data (described in section 4 below).

Later in the analysis, it was found that the above Monte Carlo lacked a subset of the second order diagrams in figure 66 which produce a $q\bar{q}$ pair from the fragmentation of a single gluon. This extra process was present in the EUROJET Monte Carlo [49], although it was not possible to use the detector simulation for technical reasons. To overcome this problem, the EUROJET Monte Carlo was run to find the cross-sections for the first and second order processes ($\sigma_E^{2\to2}$ and $\sigma_E^{2\to3}$ respectively) which produced events which passed our selection criteria. It was then possible to calculate the factor needed to increase the cross-sections from the ISAJET program (σ_I), i.e.

Table 15: ISAJET production summary

initial quark p_t (GeV/c)	luminosity (pb^{-1}) (branching ratio = 1.0)	events	run
$c\bar{c}$ 1st generation			
10 – 15	.5342	500	72
15 – 20	.4883	494	73
20 – 30	.5587	471	74
30 – 50	1.729	500	75
50 – 70	19.12	500	76
70 – 90	119.4	500	77
$b\bar{b}$ 1st generation			
9 – 10	1.540	321	81
10 – 15	.1238	485	82
15 – 20	.1393	482	83
20 – 30	.2094	469	84
30 – 50	.8531	440	85
50 – 70	12.6	500	90
70 – 90	83.15	500	91
$b\bar{b}$ 2nd generation			
12 – 15	2.102	87	86
15 – 20	4.093	420	87
20 – 30	3.520	500	88
30 – 50	5.534	500	89
50 – 70	37.2	500	94
70 – 90	184.0	500	95
$t\bar{t}$ 1st generation			
10 – 15	16.73	500	51
15 – 20	14.39	500	52
20 – 30	8.457	500	53
30 – 50	8.614	500	54
50 – 70	19.13	500	92
70 – 90	104.4	500	93
$t\bar{t}$ 2nd generation			
10 – 15	197.2	500	56
15 – 20	144.0	500	57
20 – 30	60.10	479	58
30 – 50	42.69	500	59
50 – 70	236.2	500	60

$$(\sigma_E^{2\to 2} + \sigma_E^{2\to 3})/\sigma_I. \qquad 6.1.1$$

This ratio was 2.89, and it can be compared to the ratio of 3.6 which was found in a similar study in the dimuon analysis. The final luminosities presented in table 15 were then scaled by this factor. This procedure assumes that the muon p_t spectra have the same shape for the first and second order processes.

6.2 Limits on Contributions from other Physics Processes

A number of potential sources of the events in the final muon-jet sample have been considered. The expected contributions from physics processes other than QCD heavy flavour production are estimated here.

6.2.1 Leptonic decay of an IVB with a Jet

$$p\bar{p} \to X\ W\ \text{jet followed by}\ W \to \mu\bar{\nu}$$

$$p\bar{p} \to X\ Z^0\ \text{jet followed by}\ Z^0 \to \mu^+\mu^-$$

$$p\bar{p} \to X\ Z^0\ \text{followed by}\ Z^0 \to \tau^+\tau^-\ \text{and}\ \tau \to \mu\nu\bar{\nu}$$

The process of producing a jet and a W (or Z) from an interaction is estimated from the electron channel, where the angular acceptance of the electron is a factor of two higher than for muons. In the 1983 and 1984 data samples (390 nb^{-1}), 113 events were found from the electronic decay of the W [50]. Of these 16 events had a jet with an $E_t > 10$ GeV. Assuming that these events would all pass the muon-jet trigger, one expects < 5.1 events in the data sample. For the decay of the Z^0, where the cross-section is a factor of 12 smaller, one expects < 0.4 events. The decay of the W to the τ, which then decays to $\mu\nu\bar{\nu}$ will be < 1 event, due to the branching ratio of the process $\tau \to \mu\nu\bar{\nu}$. The decay of the $Z^0 \to \tau^+\tau^-$, where one τ decays to a muon and the other to a jet (or electron) can found by a similar argument. In the 370 nb^{-1}, there are 16 Z^0 decays in the electron channel, representing a maximum of 1.5 events. This again is an upper limit as it assumes that the muon from the tau decay has $p_t > 7$ GeV/c.

6.2.2 Heavy Quark Decay of the IVB

$$p\bar{p} \rightarrow XW \text{ followed by } W \rightarrow c\bar{s} \text{ or } t\bar{b}$$

$$p\bar{p} \rightarrow XZ^0 \text{ followed by } Z^0 \rightarrow c\bar{c},\ b\bar{b} \text{ or } t\bar{t}$$

with a semi-leptonic decay of one of the quarks.

This process has been used as a signal in the search of the quark decay of the $W^{\pm}$ and Z^0 [51]. Monte carlo predictions suggest that one expects < 10 events (for a top mass of 40 GeV/c^2) in total from these processes. This number is found to be nearly independent of the mass of the top quark, as although the cross-section decreases with increasing top mass, the p_t spectrum of the decaying muons is hard, so that the probability of obtaining a high p_t muon increases with mass. This number does not include the acceptance of the detector and trigger (of order 0.5).

6.2.3 Drell-Yan production of muon pairs

$$p\bar{p} \rightarrow X\ \mu^-\mu^+\ \text{jet}$$

Monte Carlo simulations show that the number of events expected from this process is 2 [52], and are at low p_t^{μ} and E_t^{jet}.

The total number of events from the above processes therefore contribute < 20 events to the 570 events in the final data sample. The contribution from QCD production of light quarks ($d\bar{d}$ and $s\bar{s}$) are covered in the following section.

6.3 Background Sources

The sources of background for muon events has been discussed in chapter III, where it was indicated that the overwhelming contribution to the background was from the decay in flight of $\pi^{\pm}$ and $K^{\pm}$ to muons, which is more important than leakage and punchthrough. For muon-jet events one must also

consider the contribution from the mi s association of the track in the muon chamber (TKU) resulting from a decay, with a high p_t track in the central drift chamber (TKD) close to the decaying track. The methods used to calculate these backgrounds will be presented here. The background in the data sample from fake jets is extremely small; the analysis in chapter V has shown that the understanding of the jet algorithm has enabled these events to be removed early on in the data selection by software cuts.

6.3.1 Decays in Flight

Figure 67 shows the residuals from the best fit of a circle to the track digitisings in the central drift chamber for a muon candidate. The residuals are large and the shape indicates that the track is a decay of a charged kaon to a muon and neutrino, and was rejected. There will be a fraction of events in any muon sample where the kink is not so pronounced, and the reconstructed momentum of the track will not necessarily be the momentum of the original hadron. The method used to calculate the proportion of the data sample from charged π and K decays was similar to that for the dimuon analysis [53]. It uses a look-up table for the probability of a charged hadron with a transverse momentum p_t^h to decay and its momentum to be reconstructed as p_t^d. The table containing this probability, $P(p_t^h, p_t^d)$, was created by the following steps.

- Produce a large number (7500) of Monte Carlo pions and kaons isotropically over the detector with momenta between 2 and 40 GeV/c.
- Allow these hadrons to decay to muons and neutrinos, taking account of the branching ratios and kinematics.
- Reconstruct the momenta of the complete tracks and accept those which pass the quality cuts imposed in the analysis.

We then took the low threshold jet trigger data from the 1983 run which had an identical jet trigger to that in the muon-jet trigger. These two samples will therefore have similar hadron p_t distributions. Each track in the events from the background sample is taken and the probabilities found of it being a

decay with reconstructed momenta p_t^d= 7,8,9,...40 GeV/c. One can then substitute the track momentum with p_t^d by software, repeat the jet finding and missing energy calculation and analyse the event with an identical program to the one used in the data analysis. This gives us an unbiassed bin by bin estimate of the background for each plot made in the data analysis. The original momenta of the Monte Carlo tracks were not corrected for the momentum smearing of the central detector. This has little effect for low p_t tracks (such as in the dimuon calculation), but for this study a correction factor was required. By reconstructing Monte Carlo tracks over the p_t range of interest this correction factor was calculated as 0.56. The final result of the calculation gave 172 events background to the signal of 570 events, with an estimated systematic error of 50%.

6.3.2 Mis-association

When a track is found in the muon chambers it is matched in the reconstruction program to the extrapolation of all possible tracks in the central drift chamber. For muons in jets it is possible that there are ambiguities in the choice of the track which passes the matching requirement, defined as $\chi^2_{\mu-CD}$. A tight cut on this quantity removes the ambiguities, however there is a source of background introduced if the muon track originates from a decay in flight, where the direction of the muon can be shifted towards a neighbouring track in the CD (figure 68). The tight cut and steeply falling p_t distribution for hadrons at the collider ($\propto \exp\{-7p_t\}$) make this background smaller than that for direct decays, and it has been estimated in the following manner.

We take the low threshold jet trigger data sample and search for hadrons which satisfy all the quality cuts (except $\chi^2_{\mu-CD}$). Charged tracks close to the hadron (within $\Delta R < 0.7$) are assumed to be π's or K's, and decayed to muons. The probability for a particle to decay inside a cylinder of radius, R (m),is

$$P(\text{decay}) = RBm/(c\tau p_t), \qquad 6.3.1$$

where m is the mass (GeV/c^2), τ its mean life-time (seconds), B the branching ratio, and p_t the transverse momentum (GeV/c). Assuming a charged particle content of 50% $\pi^\pm$ and 25% $K^\pm$ [54],

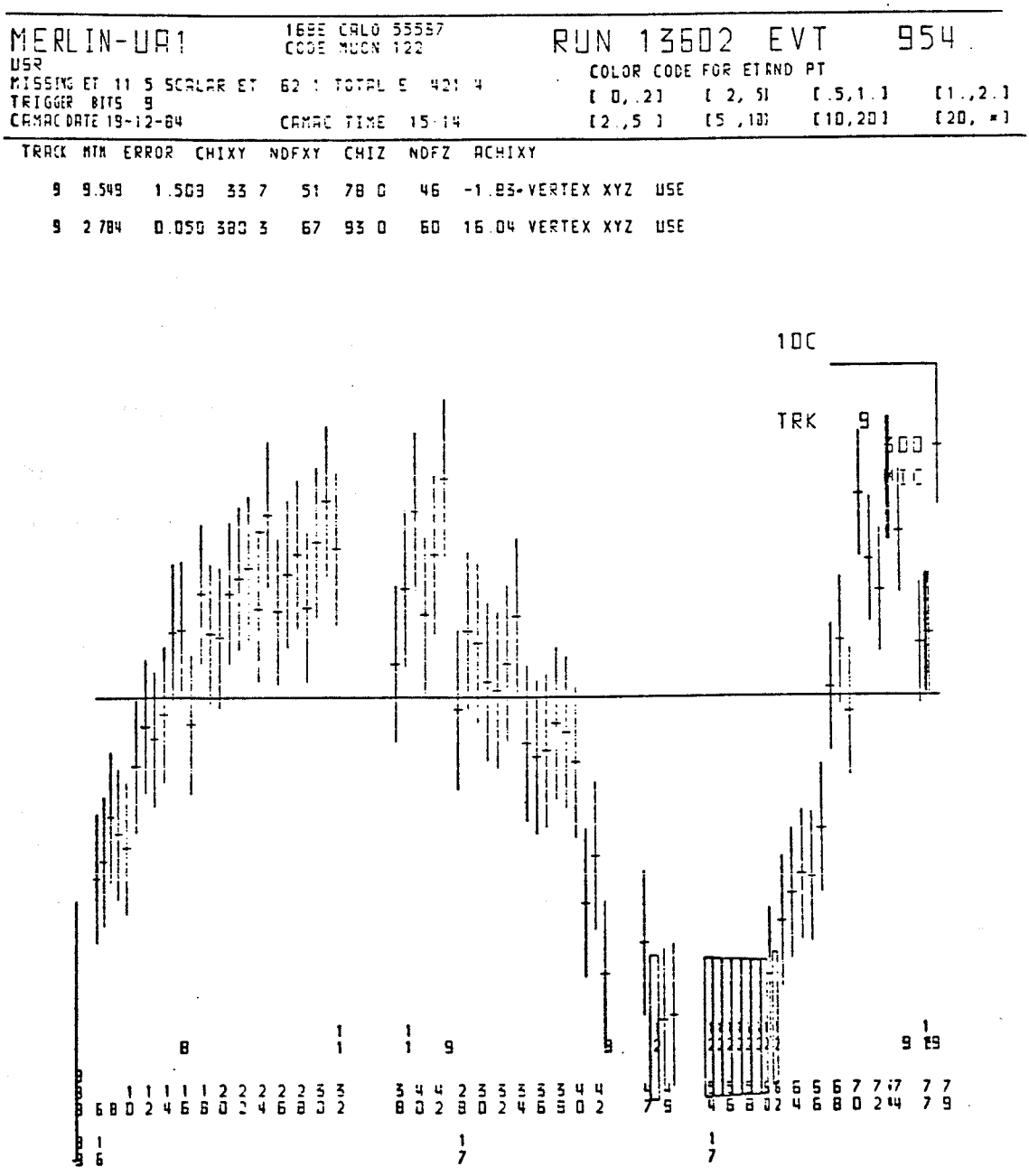

Figure 67: Example of a decay in flight found by scanning

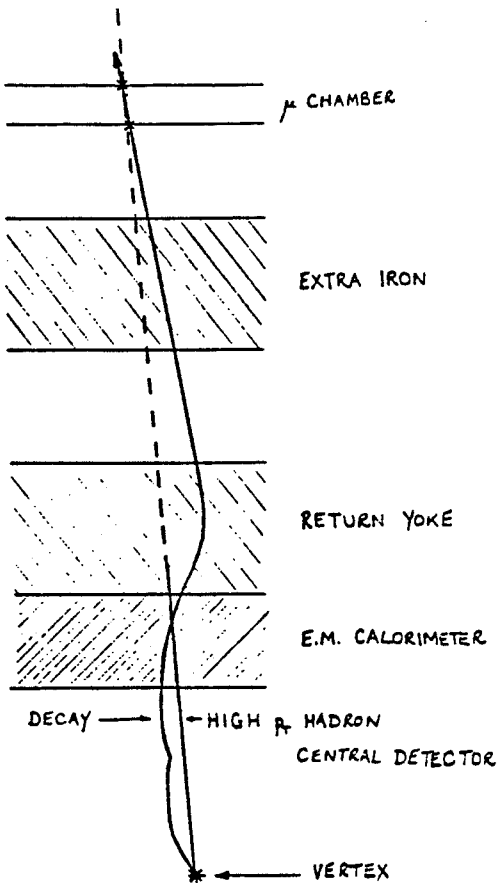

Figure 68: Diagram to show example of mis association (not to scale)

the probability to fake a muon by decay is found to be $0.04/p_t$ per incident hadron. A track in the muon chambers (TKU) is constructed for the low p_t track (with appropriate errors) and the high p_t track is compared to the fake TKU. If the match is good, then the event is taken with the correct weighting for a decay. The event is then analysed in the same manner as in the above section, so that the contribution to the background can be calculated for each bin in the data plots. The total background from this calculation is 129 events for the 570 events in the final sample. The systematic uncertainty on this number is estimated to be 50%.

6.4 Selection of the Data

The data sample used for this study was the high threshold muon-jet triggered events from the 1984 data run, with an integrated luminosity of 234 nb^{-1}. This choice of trigger enabled the calculation of the background arising from events where the identified muon is from a decay in flight of a pion or kaon. Starting from the express-line data sample, 4,165 events have a muon with $p_t > 7$ GeV/c and at least one jet with $E_t > 10$ GeV. Of these 1,362 events have the required muon-jet trigger (bit 16). This sample was too large to validate by scanning and so it was necessary to develop a set of software cuts to replace the scanning procedure. The code was tested with a substantial number of events with a muon and a calorimeter jet over the whole run range, namely the 791 events which fired the low threshold muon-electron trigger. These events were scanned, and the results are given in table 16.

Table 16: Scan Results for Muon-Electron Trigger

584	good events
74	CD track below 7 GeV/c after fixup
56	kink in track, likely decay from pion or kaon
40	CD track pointing to crack in calorimetry
19	double interaction at vertex
8	cosmic ray
5	end-cap em calorimeter problem, giving false jet
4	muon points to secondary vertex
1	muon from beam halo

At this stage, the events have passed only loose quality requirements, and it was necessary to use cuts which have been used as 'standard' in muon type analyses, such as in the IVB searches. The cuts fall into two classes, fiducial and technical, both of which must be included in the acceptance calculation. The efficiency factors were calculated from apparatus Monte Carlos and by comparison with the $W \rightarrow \mu\bar{\nu}$ sample. After this work and also consultation with other analysis groups the cuts converged to those presented in table 17. The overlap between the software and the scan selections are shown in table 18.

Table 17: Cuts to Reproduce Scan Results

Event Cuts	
UA1 jet algorithm	$E_t > 10$ GeV
Total Energy in event	$E_{total} < 630$ GeV.
Secondary Vertex; reject events when both the following are satisfied;	
multiplicity of secondary vertex	$N_2 > 5$
distance from primary vertex	$\lvert(x_1 - x_2)\rvert/\sqrt{(\Delta x_1^2 + \Delta x_2^2)} > 5.$
With at least one muon passing	
track chisquared in the xy plane	$f(\chi^2_{xy}) < 3.$
track length in the xy plane	$\ell_{xy} > 0.4$m
track chisquared in the z direction	$\chi^2_z/N_{points} < 9.$
rapidity of muon	$\lvert\eta_\mu\rvert < 1.5$
transverse momentum of muon	$p_t > 7$ GeV/c
CD and muon track matching	$\chi^2_{\mu-CD} < 4\sigma$

Table 18: Comparison of software and scan selections

		software selection		
		PASS	FAIL	
scan	PASS	387	197	584
	FAIL	58	149	207
		445	346	791

The tracks in the central detector for the 445 events which passed the cuts were then processed through an autofixup process recently developed at CERN. This computer algorithm is based on the scanning procedure which minimises the χ^2 of the track fitted in the central detector by the inclusion or exclusion of digitisings close to the original track. It obtains a better measurement of the momentum and removes extraneous points caused by nearby tracks. The results from autofixup are shown in table 19.

Table 19: Comparison of autofixup and scan

		autofixup		
		PASS	FAIL	
scan	PASS	352	35	387
	FAIL	49	9	58
		401	44	445

This shows an agreement between scanner and program of 81.1%. Applying autofixup has made 35 of the events fail the cuts which they previously passed. These breakdown as follow;

35 events which fail cuts after autofixup

26	p_t lower after fixup
3	$\ell_{xy} < 0.4$m after fixup
1	both p_t lower and $\ell_{xy} < 0.4$m after fixup
5	CD no longer matches muon track

The breakdown for the events for which the scanner has failed, but autofixup accepts is as follows;

49 events passing cuts and autofixup but fail scanning

17	leakage
14	kink
12	low p_t track 'matches' muon track better
4	bad calorimeter cell associated with jet
1	cosmic
1	punchthrough, muon has passed through iron

Of the events which were failed by the scanner but passed auto-fixup, 35% were classified as leakage. Investigation of these events showed that they were not leakage, but had passed through uncalorimeterised iron. As they did not give a m.i.p. signal, then the scanner had mistakenly rejected them as leakage. The 49 events were then rescanned on the MEGATEK facility, and it was found that only two events should have been rejected, these were both classed as decays in flight, and are included in the background calculation in the previous section.

The power of the individual cuts after the autofixup program can now be investigated. From the original sample of 791 events which passed the initial requirements of $E_t^{jet} > 10$ GeV, $p_t^{\mu} > 7$ GeV/c and $\chi_Z^2/N < 9.$, 78% of the events failed only one of the cuts in table 17 after autofixup. The breakdown of these events is shown in table 20. The most powerful cut is track length requirement, which reflects the loose cut (which required only 20 points on the track) on the initial sample from the express line.

Table 20: Power of individual cuts after autofixup

Percentages of events which fail only one of the cuts in table 17 in the original selection after autofixup.	
Total Energy in event	3.3%
Secondary Vertex rejection	3.9%
track chisquared in the xy plane	20.3%
track length in the xy plane	40.6%
transverse momentum of muon	2.2%
CD and muon track matching	29.3%
Total	100%

We then applied this selection technique to the events which had a muon-jet trigger, from the 1,362 events in the original selection, 570 remain in the final sample.

The conclusion of this study showed that it is possible to replace large scale scanning with software selection using a careful choice of cuts. Scanning is still essential for small selections of critical classes of events, where one scanner may completely study each event, but for the present analysis with a large sample one is driven to rely on software rejection techniques.

6.5 Cross-section of Muon-Jet Production in UA1

From the above data selection and corresponding background calculation we can extract the cross-section of muon-jet production in UA1. The jet E_t spectrum is shown in figure 69, and the effect of the hardware trigger at 15 GeV can be seen in the spectrum. For this reason, we have taken two jet

E_t thresholds, 10 GeV and 20 GeV. At the higher threshold the effect of the trigger is small (as it is 90% efficient at this energy). The data presented in this section have a transverse momentum cut on the muon at 10 GeV/c inside the rapidity region of ± 1.5, and the jet transverse energy (defined by the UA1 algorithm) of greater than 10 or 20 GeV, again inside the rapidity region of ± 1.5.

Figures 70 and 71 show the uncorrected p_t spectrum of the muon for the two jet thresholds, with the backgrounds from the two decay calculations. The shallow slope at low p_t in the data is an acceptance problem due to the effect of cutting before and after the autofixup program at the same momentum. We therefore cut at $p_t > 10$ GeV/c, and we can correct for the error on the track momentum using the method described in Appendix D. This correction is found to decrease the data by a factor 0.30. The acceptance of the muons is calculated as follows;

- 0.90 for the efficiency arising from the hard cut on $\chi^2_{\mu-CD}$, calculated from W sample.
- 0.758 from a Monte Carlo simulation of track acceptance in the central drift chamber
- 0.69 for the angular muon chamber acceptance.
- 0.60 for the jet trigger acceptance at 10 GeV, and 0.90 at 20 GeV.

The differential cross-sections as a function of p_t^μ with the acceptance corrections are shown in figures 72 and 73. The fit is a paramaterisation of Ap_t^{-n}, with $n = 6.9 \pm 1.4$, and found by minimising the χ^2 for the $E_t^{jet} > 10$ GeV data. For the low jet threshold, the cross-section for $p_t^\mu > 10$ GeV/c is

$$0.92 \text{ nb} \pm 0.08 \text{ (stat.)} \pm 0.55 \text{ (syst.)},$$

and for $p_t^\mu > 10$ GeV/c and $E_t^{jet} > 20$ GeV/c we have

$$0.54 \text{ nb} \pm 0.05 \text{ (stat.)} \pm 0.33 \text{ (syst.)}.$$

The systematic error has a 10% contribution from the uncertainty in luminosity, and a 50% contribution from the decay calculation. As the errors are dominated by the systematic error from the background calculation for decays in flight, one can conclude that future studies would require better rejection of this class of background.

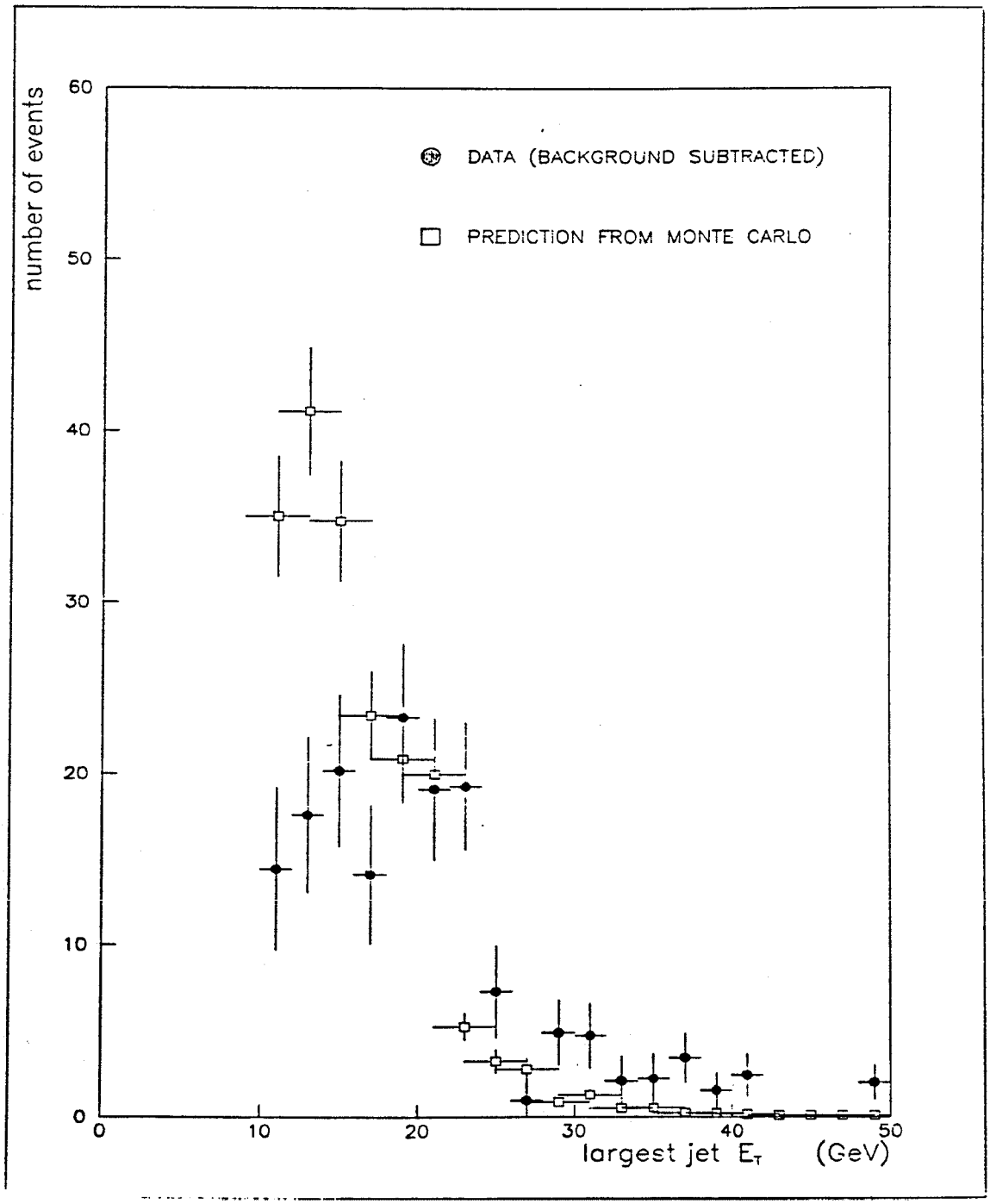

Figure 69: Highest transverse energy of jet in event

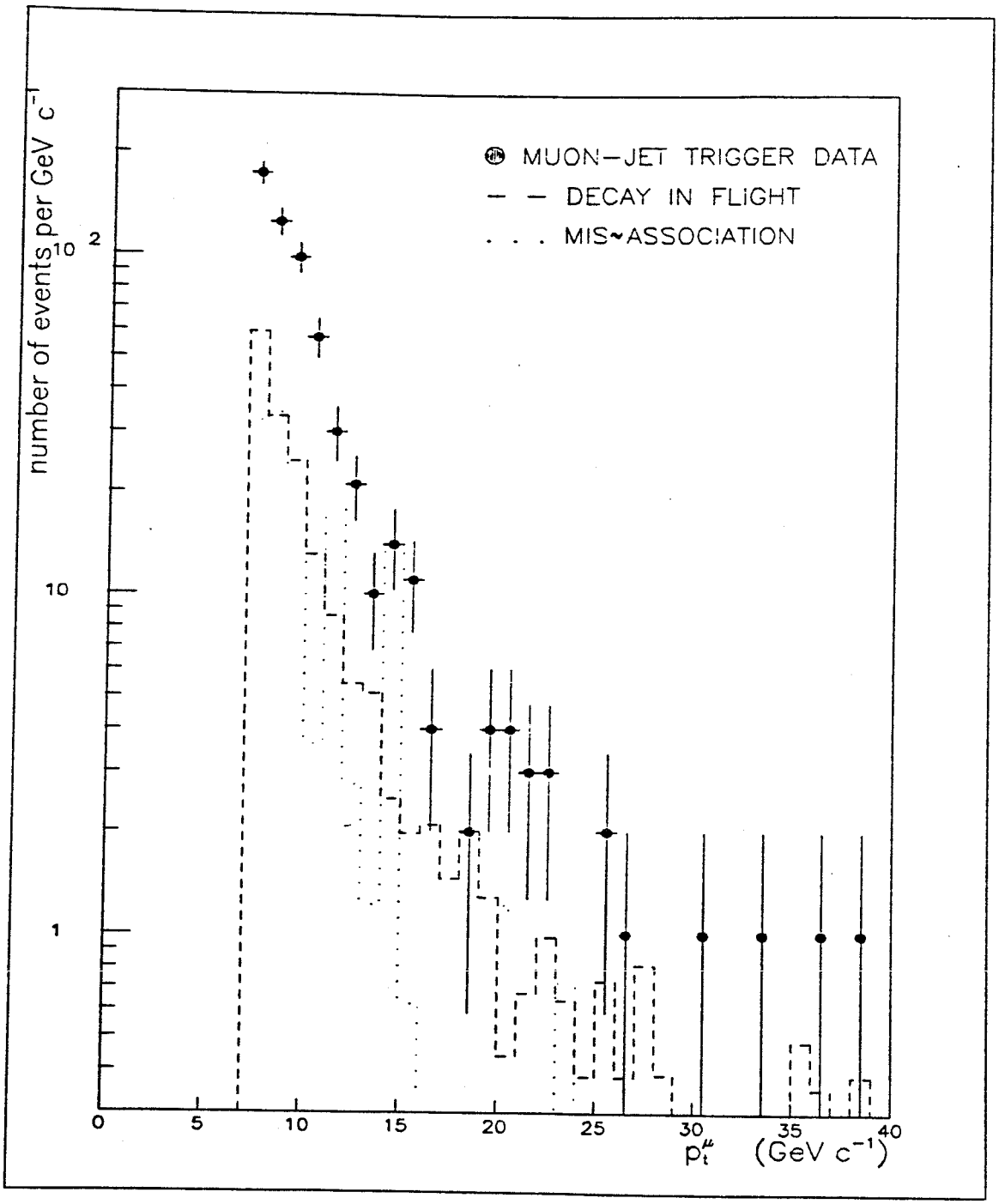

Figure 70: Uncorrected p_t^{μ} spectrum, $E_t^{jet} > 10$ GeV

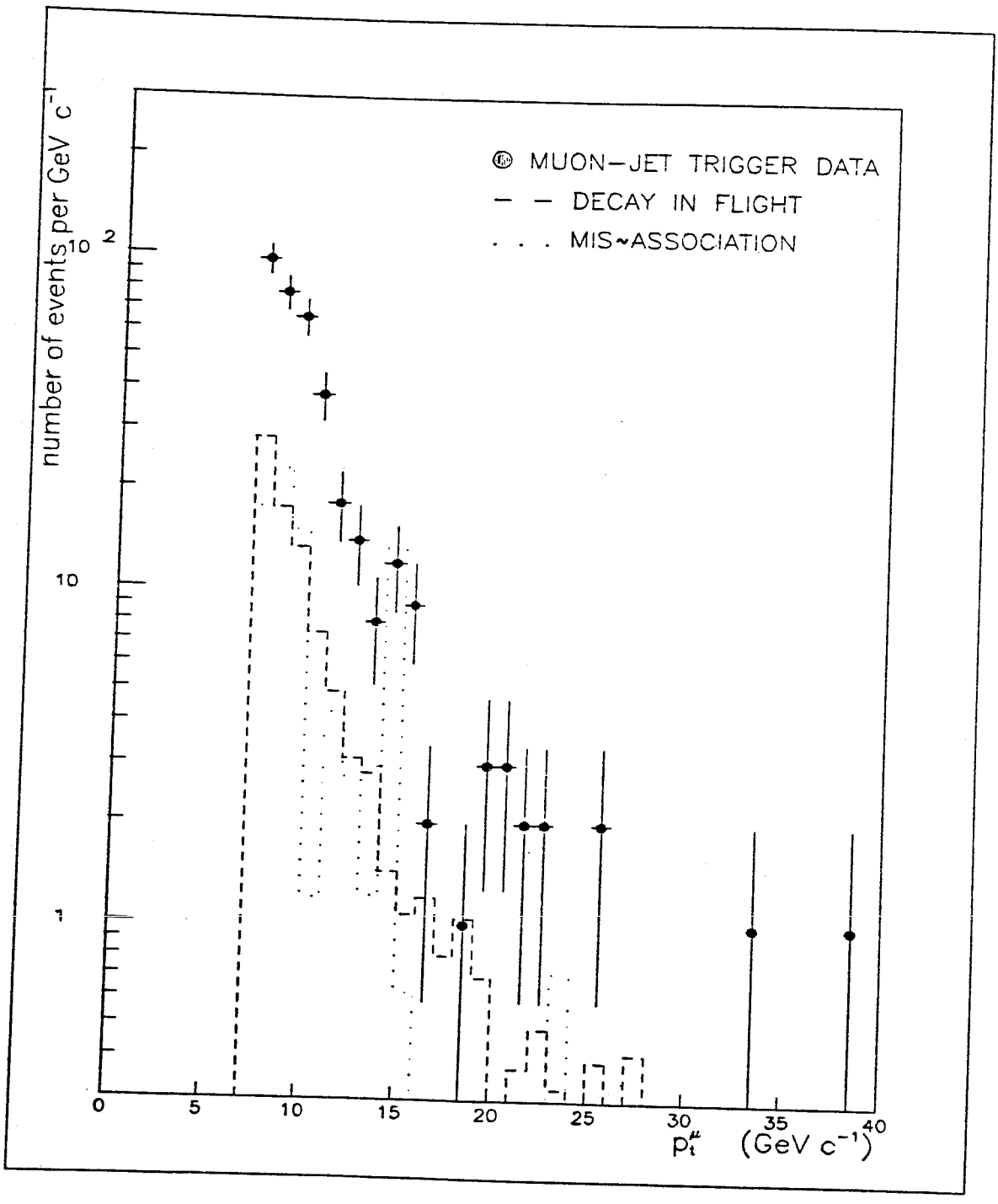

Figure 71: Uncorrected p_t^μ spectrum, $E_t^{jet} > 20$ GeV

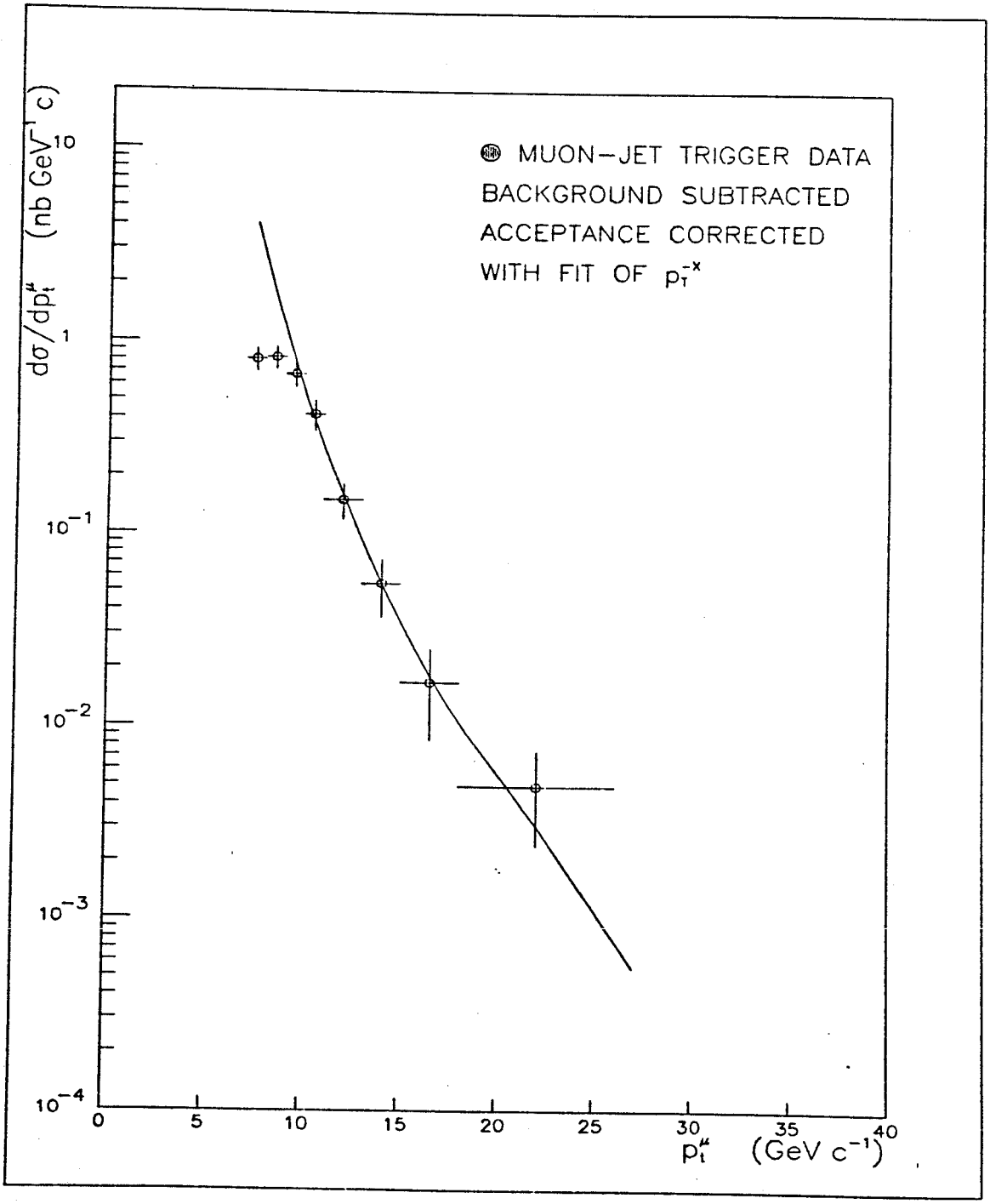

Figure 72: Corrected p_t^μ spectrum, $E_t^{jet} > 10$ GeV

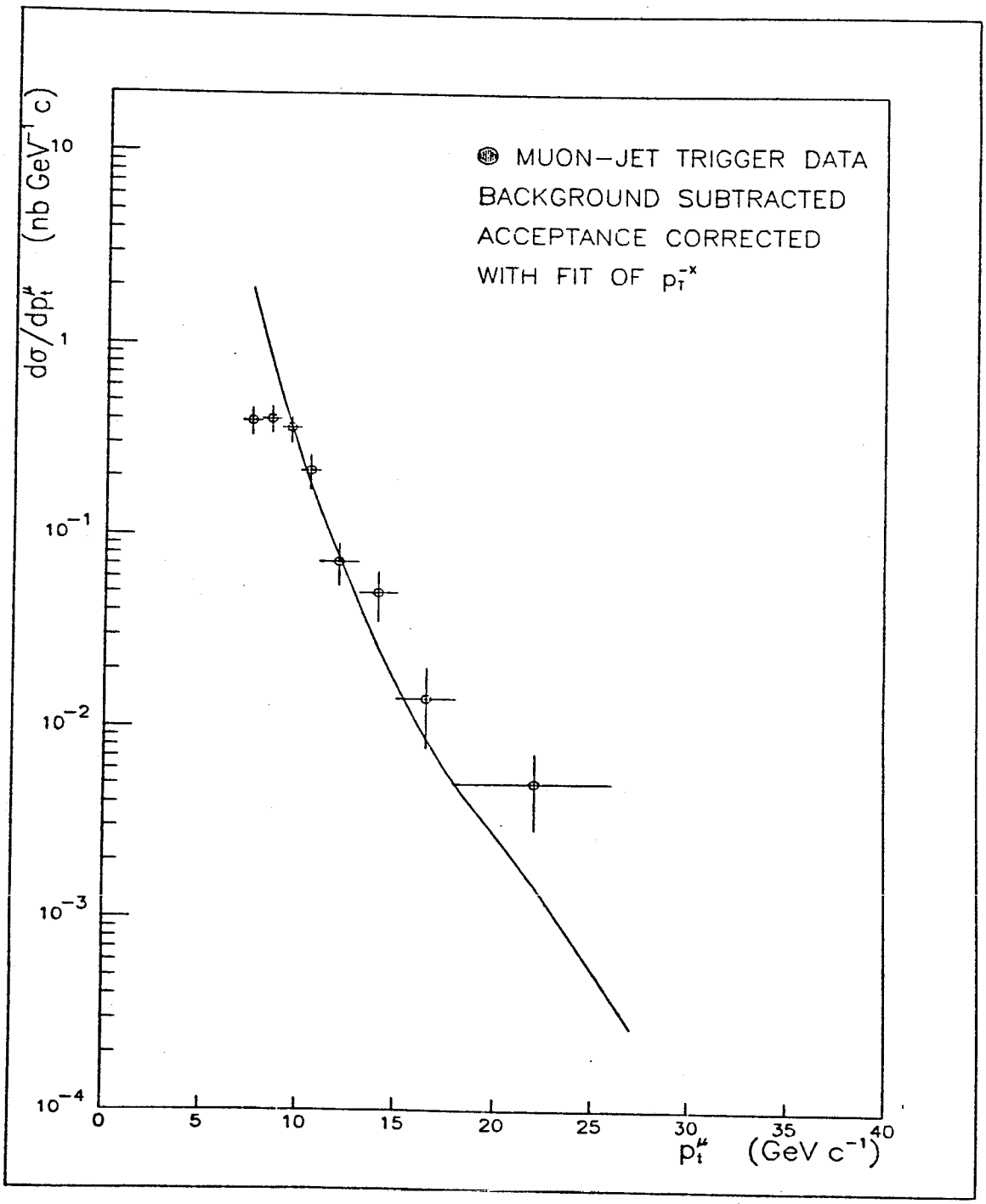

Figure 73: Corrected p_t^μ spectrum, $E_t^{jet} > 20$ GeV

6.6 Comparison of the Data with Monte Carlo

It is now possible to compare the p_t spectrum of the data with the prediction from the Monte Carlo. From the discussion in section 2, it was indicated that the Monte Carlo does not reproduce the initial state bremsstrahlung of the quarks, and so a further cut was introduced in the data, Monte Carlo and background programs to remove events with more than two jets. This cut reduces the event sample to 300 events with $E_t^{jet} > 10$ GeV, but also reduces background from 52% to 45%. Figures 74 and 75 show the spectra of the muon p_t's for the different generated processes, and for the uncorrected data and background for $E_t^{jet} > 10$ and > 20 GeV. Table 21 shows the numbers of events in $234nb^{-1}$ from the data and predicted by the Monte Carlo. We have used the absolute normalisation from the Monte Carlo and the branching ratios of 0.12 for $b \rightarrow \mu^- \bar{\nu} c$ and 0.085 for $c \rightarrow \mu^+ \nu s$ [55]. The branching ratio for $t \rightarrow \mu^+ \nu b$ has been estimated as 0.12 from the simple branching ratio of $W \rightarrow \mu\bar{\nu}$ above the production threshold for heavy quarks.

Figures 76 and 77 show the p_t^{μ} for the data after background subtraction, and the sums of the Monte Carlo processes. The ratio between the numbers of events in the data and Monte Carlo is 0.97 ± 0.19 (statistical errors) for $E_t^{jet} > 10$ GeV. There is a systematic error in this quantity from the uncertainties in the Monte Carlo (200%) and from the background calculation (50%). This result shows that there is remarkable agreement between the data and Monte Carlo. Increasing the cut on the jet to 20 GeV results in a ratio of 0.43 ± 0.09 (statistical error), again showing good agreement between the data and prediction.

To compare the shapes of the p_t distributions of the data and Monte Carlo we take each 1 GeV/c bin and define a χ^2_{fit},

$$\chi^2_{fit} = \Sigma_i (n_i - \alpha m_i)^2 / \sqrt{(\Delta n_i^2 + \alpha^2 \Delta m^2{}_i)} \qquad 6.6.1$$

where $n_i \pm \Delta n_i$ [$m_i \pm \Delta m_i$] is the number of events in the i'th GeV/c bin for the data [Monte Carlo], and α is the normalisation between the data and Monte Carlo. Due to the limit from statistics, we take the p_t range between 10 and 16 GeV/c. The results of this fit are shown in table 22, where the data has

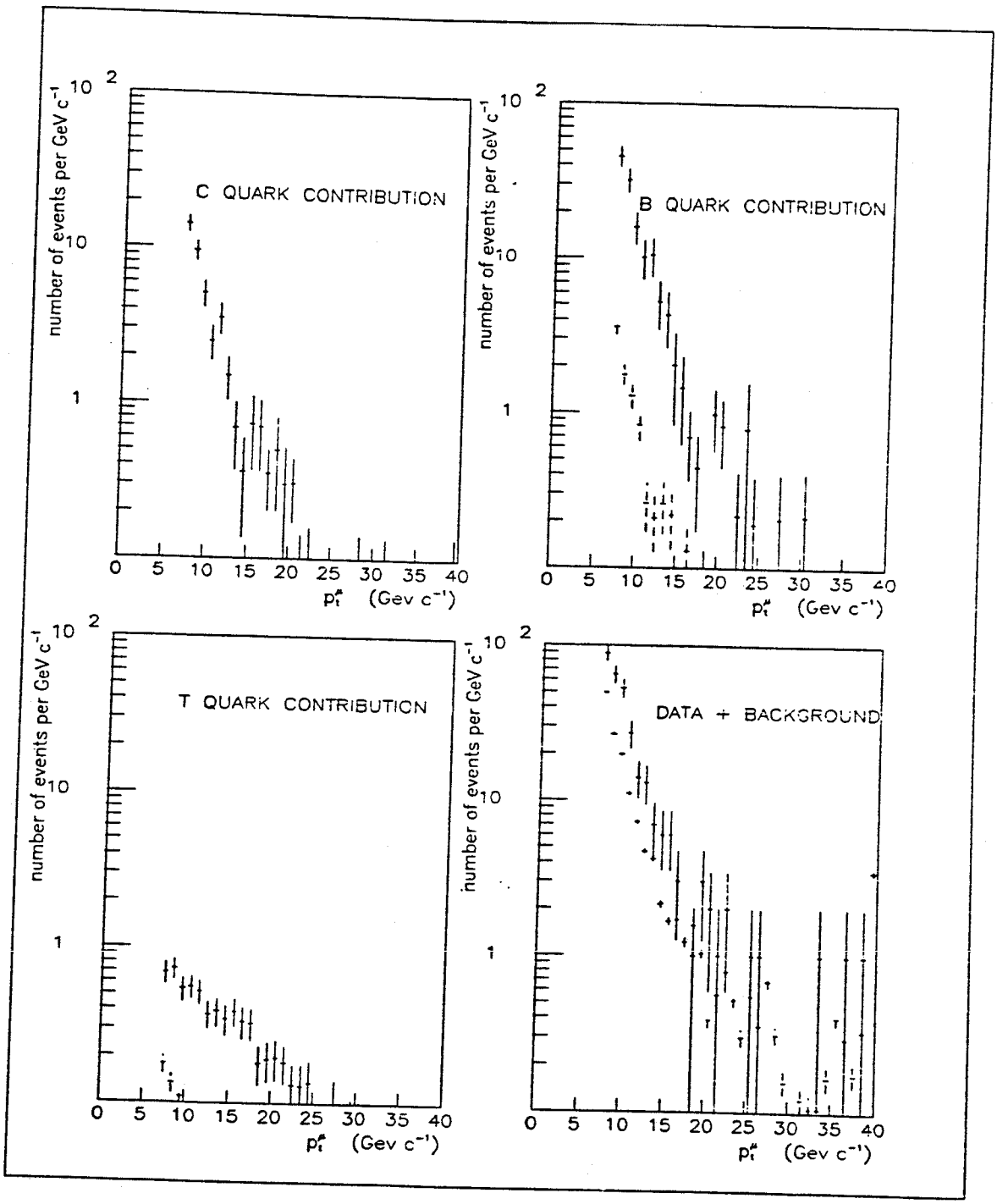

Figure 74: p_t^{μ} separate spectra ($E_t^{jet} > 10$)

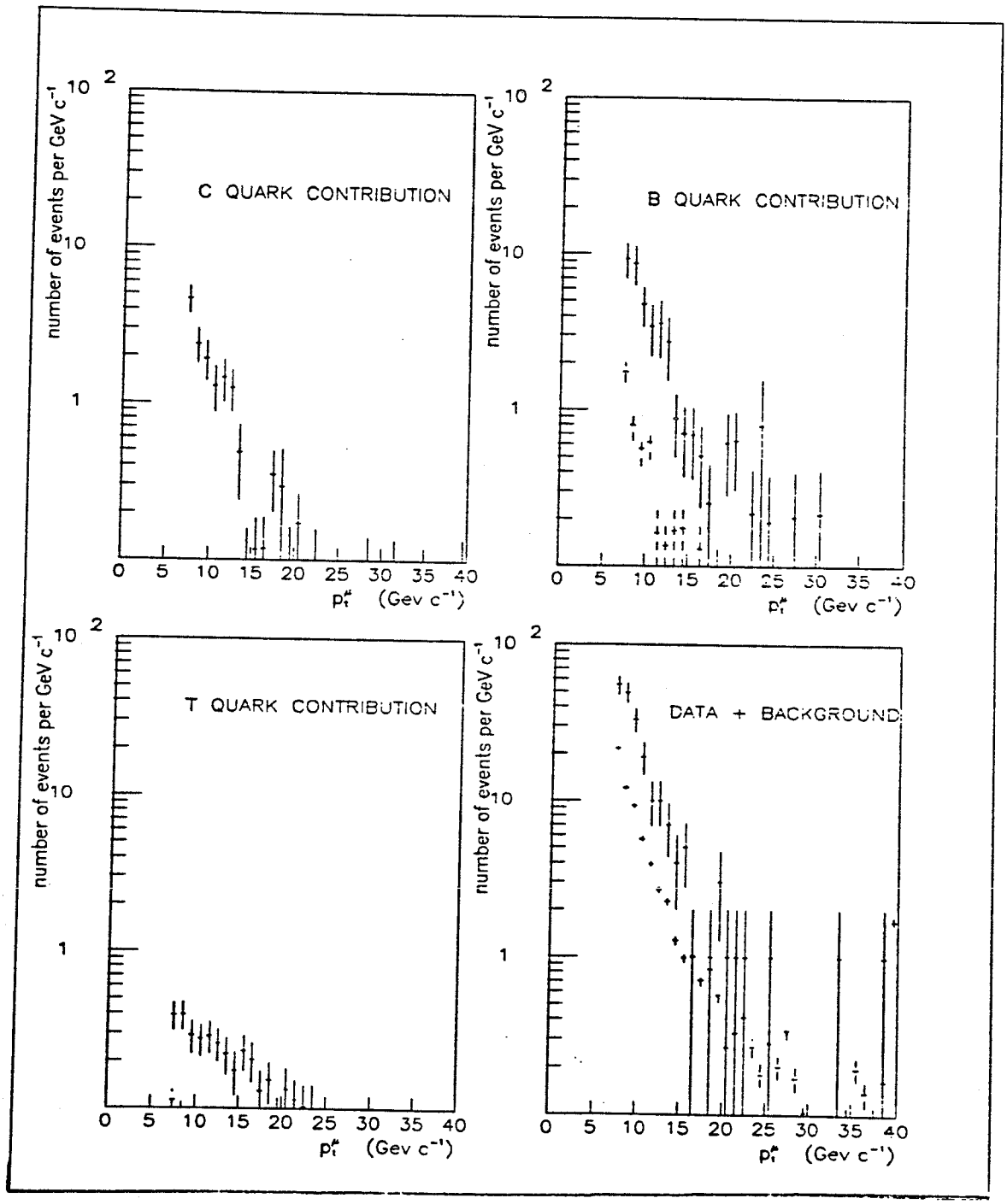

Figure 75: p_t^{μ} separate spectra ($E_t^{jet} > 20$)

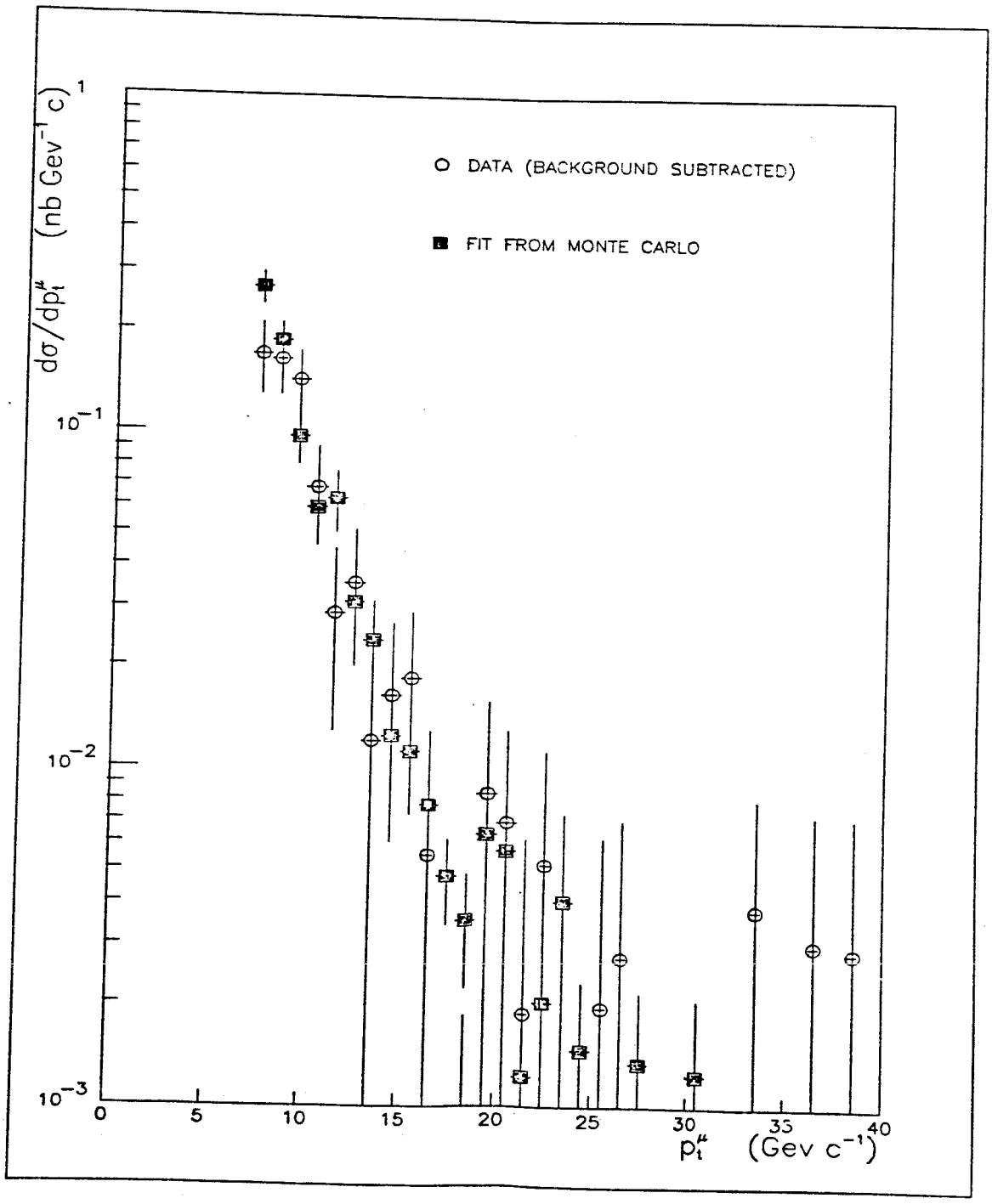

Figure 76: p_t^μ summed spectra ($E_t^{jet} > 10$)

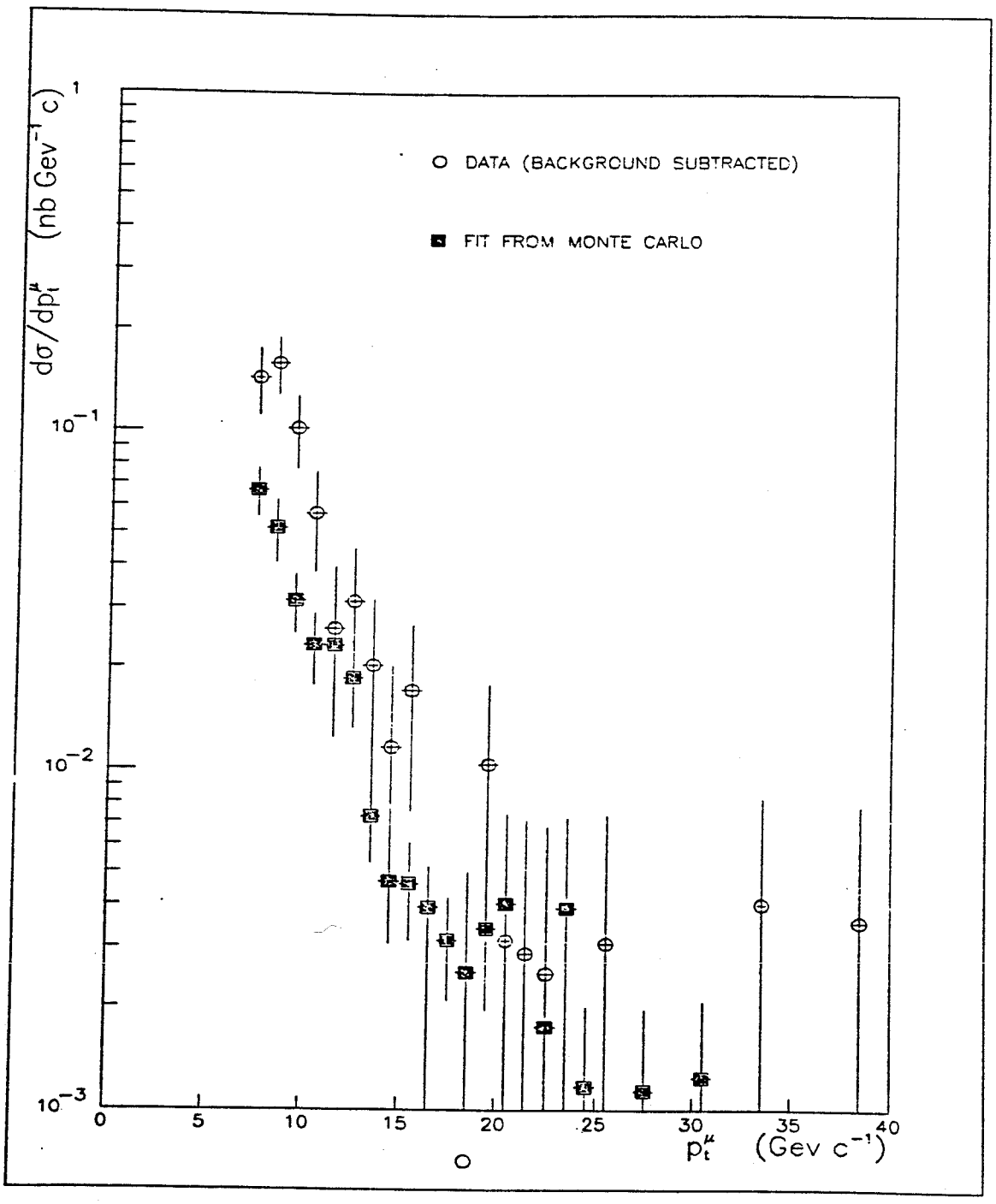

Figure 77: p_t^μ summed spectra ($E_t^{jet} > 20$)

been divided into the samples of 1 jet plus μ, 2 jet plus μ, and either 1 or 2 jets plus μ. Although the ratios between the Monte Carlo and data are affected by the uncertainty in the theoretical cross-section, the values of the (unnormalised) χ^2_{fit}'s tend to favour the 20 GeV data over the 10 GeV data. This is due to the hardware trigger threshold, as mentioned in the previous section. It is also obvious that the number of jets found in the Monte Carlo does not agree with the number in the data, as the ratios of one jet events to two jet events are 4.6 for $E_t^{jet} > 10$ GeV and 3.3 for $E_t^{jet} > 20$ GeV. On average, the number of jets found in the Monte Carlo is smaller than the number in the data, and this will be discussed later.

Table 21: Number of events per 234nb^{-1} in Data and Monte Carlo

	data	charm	bottom 1st. gen	bottom 2nd. gen	top 1st. gen	top 2nd gen
$E_t^{jet} > 10$ GeV $10 < p_t^{\mu} < 16$ GeV/c						
one jet	19±6	7.4±1.2	31±5	1.1±.2	1.0±.1	.09±.02
two jet	58±9	7.0±1.0	19±3	2.0±.3	2.1±.2	.26±.03
both	75±11	14.±2.6	50±6	3.1±.3	3.1±.2	.35±.03
$E_t^{jet} > 20$ GeV $10 < p_t^{\mu} < 16$ GeV/c						
one jet	11±4	1.6±0.5	6±2	0.4±.1	0.4±.1	.04±.01
two jet	53±8	5.0±0.8	11±2	1.5±.2	1.3±.1	.18±.02
both	62±9	6.6±0.9	17±3	1.9±.2	1.7±.2	.22±.03

The shapes of the individual p_t spectra for the charm and bottom quarks in figures 74 and 75 are very similar, as one would expect for heavy $q\bar{q}$ production above threshold. This fact has excluded the possibility of fitting the shapes to compare the ratio of the contributions from b and c quarks with that from e^+e^-.

Table 22: Comparison of Normalisation and Shape

	χ^2_{fit} (4 d.o.f.)	ratio M.C./data (α^{-1})	statistical error
$E_t^{jet} > 10$ GeV $10 < p_t^{\mu} < 16$ GeV/c			
one jet	4.75	2.46	1.15
two jet	7.42	0.54	1.21
both	5.97	0.97	0.19
$E_t^{jet} > 20$ GeV $10 < p_t^{\mu} < 16$ GeV/c			
one jet	4.46	1.22	0.85
two jet	2.26	0.37	0.07
both	3.91	0.43	0.09

From the numbers in table 22 it is possible to extract the total cross-section for b and c quarks in UA1. Using the original version of ISAJET to produce quark pairs with initial $p_t^{\mu} > 5$ GeV/c within a rapidity interval of $|\eta| < 1.5$, we find that the total cross-sections for QCD pair production of b and c quarks are 0.5421 μb and 1.505 μb respectively. These values are then scaled by the factor of 2.89 for the extra processes (equation 6.1.1) not included in the Monte Carlo, and the normalisation from table 22 for 1 or 2 jets above the high jet threshold. The resulting total cross-section for b quarks is

$$0.67\ \mu b \pm 0.14\ (stat.) \pm 0.34\ (syst.),$$

and for c quarks,

$$1.87\ \mu b \pm 0.39\ (stat.) \pm 0.94\ (syst.).$$

The systematic error quoted is from the uncertainty in the background calculation which forms a large fraction (50%) of the data sample. The cross-section for b quarks is consistent with the value obtained from the UA1 dimuon analysis, which is 1.0 μb $\pm$0.1 (stat.) $\pm$0.2 (syst.), for $|\eta| < 2$ and $p_t^i > 5$ GeV/c.

6.7 Conclusions

This chapter has studied muon-jet events at the $p\bar{p}$ collider, with a determination of the (large) backgrounds from decays in flight of light quarks. We have presented the differential cross-section with respect to p_t^{μ}, and made a detailed comparison with heavy flavour production from QCD. The predictions fit the shape of the p_t^{μ} spectra and the absolute normalisation agrees well within the systematic errors present in the Monte Carlo and background calculation. The muon spectra from b and c quarks decay are very similar, and it is not possible to make a separation of the two processes using the muon spectrum alone. Similar attempts using other variables such as E_t^{jet} and ΔR_{μ}^{jet}, have reached the same conclusion.

The process of heavy quark production and their decay to muons appears to be correctly predicted, comparing well with Monte Carlos based principally on data from e^+e^- interactions. The differences between the Monte Carlo and data, such as 'jet counting', arise from the difficulties involved in calculating the underlying event in $p\bar{p}$ collisions. This has been seen in jet fragmentation analysis [43], where it has been found that the underlying events affects both the width of jets and 'jet counting' for low E_t jets. By studying the QCD jet data, these problems are hoped to be understood in the future.

The background from the decays of light quarks represents a large fraction of the muon-jet data, highlighting the need for the detectors described in chapter IV. The information from the Iarocci tubes will help identify the decays, and so make it easier to reject them from the data sample.

The original Monte Carlo used in this analysis has recently been superseded by an improved form of ISAJET where the higher order processes have been included and a better estimate of the underlying event is made. The EUROJET program has also been upgraded to include a UA1 detector simulation, and so an obvious continuation of this work will be to compare these Monte Carlos to the data signal in a similar method.

APPENDIX A

THE UA1 COORDINATE SYSTEM AND TRACK QUALITY MEASUREMENTS

There are three coordinate systems commonly used within UA1, cartesian, bubble chamber, and 'Feynman' covariant systems. The first is used to describe the apparatus, and the second and third are used to define the directions of tracks in the experiment.

Table 23: Right-handed Cartesian System

x	measured along the beam axis in the direction of the antiprotons.
y	vertical axis of the experiment, measured upwards.
z	horizontal axis of experiment, measured outwards from the centre of the SPS.

Table 24: Bubble Chamber System

ℓ	dip angle in dipole field between the track and the plane perpendicular to the field axis.
θ_B	angle between the track and the $\bar{p}$ axis, measured in the plane perpendicular to the field axis.

There are three different χ^2's used in the text to measure track quality and are listed here.

- χ^2_Z/N; where χ^2_Z is the χ^2 of the track in the central drift chamber in the z direction, and N its number of degrees of freedom.

Table 25: Feynman Covariant System

ϕ	azimuthal angle around beam, measured from the horizontal axis.
η	pseudo-rapidity of particle, equal to $-\ln\{\tan(\theta/2)\}$ where θ is the polar angle between the track and the $\bar{p}$ axis (chapter V equation 5.1.2).

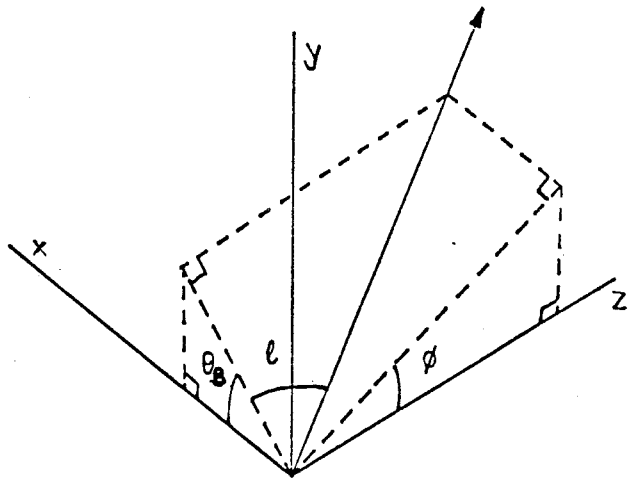

Figure 78: Sketch of angles used in coordinate systems

- $f(\chi^2_{xy})$; a function of the χ^2 of the track in the central drift chamber in the xy plane, χ^2_{xy}, and the number of degrees of freedom, N_{xy}, i.e. $f(\chi^2_{xy}) = \sqrt{(2\chi^2_{xy})} - \sqrt{(2N_{xy} - 1)}$.
- $\chi^2_{\mu-CD}$ which measures the goodness of fit between the track in the central drift chamber and the track in the muon chamber. It can be defined by $\chi^2_{\mu-CD} = 0.25\,\Sigma_i x_i^2/(\Delta(x_i)^2 + \alpha_i^2)$ where the sum is over four values, x_i, measured as differences between the extrapolated tracks from the muon chamber and CD, at the plane midway between the pair of muon chambers. These values are; the distance parallel to the long wires in the muon chambers; the distance parallel to the short wires in the muon chambers; the dip angle, λ; and angle of ϕ. The quantity $\Delta(x_i)$ represents the statistical error on the measurement x_i, and α_i the systematic error associated for that muon chamber.

APPENDIX B

COMMAND MANUAL OF VMEFT

FT Controller in the Birmingham CPUA1

to fill FT processor memory and exercise trigger

JON%VZ 14 May 1984

Description of the subroutines.

This program is based on the note 7−12 May 1984 HR & JS, "Tentative manual for the VMEFT program". The commands can be entered directly from a terminal connected to the micro or through the Nord Mailbox system (not yet ipld). The command and arguments should be entered on the keyboard in response to the prompt ' vmeft > ' or ' data > '. Input will be terminated by a string which does not end in a comma. Commands which produce output have the following string format :

- first long word − total length of string in ASCII
- followed by input command & arguments
- followed by result of command if no error was encountered
- ending with the return code as a long word e.g. rc00 for a good command.

Brief explanations of the non zero return codes are given on page 10 of this listing.

command arguments

LOAD <,arg1>[,arg2][,arg3] ...

Load given module(s); module no. = 1−24,31−34; 0=ALL Loads the current default. The VMEFT card table is not updated, but at the end of the command, the old table is reloaded.

VERI <,arg1>[,arg2][,arg3] ...

Verifies all chips in given module(s) module no. = 1−24,31−34; 0=ALL Compares with current default. The answer contains (in units of words) a) for mod=0, 34 values telling no. of bad chips per module. b) for mod>0, 63 words, namely no. of bad chips, no. of chips tested, and their individual error counts (0−FF). The VMEFT card table is not updated, but at the end of the command, the old table is reloaded.

CONFI <,filename>

Generate :CONF file from loaded :SAVE file. Defaults to SAVE file at %600000.

QFILL

Prints out header of current filling file.

IDFILL

To look at the filling id on a chip or range of chips. The arguments are the same as BWCHM.

BSWON

To unblock sequencer, switch on crates, switch on X,Y,X.Y & S cards.

BINIT

To initialise the 68010.

BLFILL

List the filling ids on the 68010.

BRFILL <,filling id>

Returns the filling labelled "id" and header.

EXIT

Return to monitor of the micro.

MENU

Gives a list of the commands recognised by VMEFT.

MARK

Shows date & time created.

FLIST [,pointer]

Returns list of files on 68010 if a pointer is present (4 chars) then all files beginning with it or having this filetype will be listed. Gives filename, address and length in bytes.

FWRITE <,filename> <,data>

Create a new file containing this data.

FREAD <,filename> <,%HEXA>[,%HEXB]

Reads a file to current output device starting at the HEXAth byte and for HEXB bytes maximum value of HEXB is 1024, which is default.

FDELETE <,filename>

Deletes file.

FEXEC or X [,filename]

Executes file which must have filetype EXEC. EXEC files can contain a list of commands & arguments separated by "."s, eg to load a module create a file like

FWRITE,CRATE:EXEC:1,LOAD,21.LOAD,22.LOAD,23.LOAD,24

and to execute type

FEXEC,CRATE:EXEC:1 or FEXEC,CRATE

If no filename is given then the last EXEC file used with FEXEC is used.

nb If EXEC A calls EXEC B then at the end of EXEC B the program continues inside EXEC A. If EXEC A calls EXEC B which calls EXEC C then at the end of C the program continues from EXEC A, not EXEC B.

FRENAME <,filename1> <,filename2>

Renames filename1 by filename2.

FCOPY <,filename1> <,filename2>

Copies filename1 to filename2.

FAPPEND <,filename1> <,data>

Appends filename with data. Note the comma is replaced with a full stop when the data is appended.

FDIV <,filename>

This command diverts the next command which produces output onto the given file. If the return code of this next output is not rc00 then the output is given to the current output port (eg the terminal) and the file is not affected.

MESS <,message>

Prints MESSage to port.

MESM <,message>

MESsage Marker. Prints MESSage to port.

MESC <,message>

MESage Command. Prints message and awaits reply :

E	Exits exec
Y or cr	Yes, please continue
N	jump to Next MESM command in exec.

MESJ <,ABCD>

MESsage Jump. Jumps to start of current exec, searches for first command beginning ABCD and continues with this command.

FPUSH <,filename> <,%HEXNUM>

To push a file to RAM. Takes a file in the directory & copies to a specified address in memory.

FPULL <,filename> <,%HEXNUM>

To pull a file from RAM. Copies a file in RAM to the next available free memory in VMEFT and enters file to directory. The new file name does not have to be the old one.

BLOOP <,arg1>[,arg2]<,decimal nos.>

To loop on commands, used for testing only. Will loop on subsequent commands if arg ne 0 needs to be reset to 0 before normal use. If arg2 is defined and not zero then output will be suppressed.

BWCOMM <,arg>

Appends COMM1 + (0 − 3) onto a command & sends to output device if arg is not zero.

BSEQ <,arg1>[,arg2]<,dec>[,%HEXA]

Move zero to a sequence via COMM2 + arg1. If defined,arg2 will be moved to this address, nb to unlock the sequencer use BUNLSEQ.

BVLS <,arg1> <,arg2>[,arg3]<,0 or 1> <,%HEXA>[,%HEXB]

To write/read to/from addresses like %00FFHEXA. 0 for write, 1 for read. %HEXA is the lower word of the address and %HEXB is the data word to be written. If %HEXB is not specified for write then zero is written.

BRSCRD <,mod> < ,byte>

To read data from an S card. "mod" = module no. between 1 & 34 "byte" = data word to be read between 0 & 12. If no byte is present, all bytes are given. If no module, then last no. in BRCHM,BVCHM or BWCHM is used.

IR <,number> <,0,1,2,...F>

To read the Input Registers. Reads a word from FFB004 + 100*number and displays to output port.

BG1 <,S> <,1> <,1T> <,G> <,GT> <,%HEXA>

Read/write to Burst Generator at FFC100.

(i) reads status

(ii) one shot

(iii) one shot + test pulse

(iv) generator

(v) generator + test pulse

(vi) any hexadecimal number

replies with YES or NO in (ii) to (v) for track found or not, in (vi) the word is read back. All other possibilities result in error codes.

BG2

Read/write to Burst Generator at FFC200.

BMON <,command>

To execute a monitor command from VMEFT.

BUNLSEQ

Unlocks the sequencer.

BWROU [,WAM0,...,WAM9][2 digit decimals][or 5 x %HEXA]

Loads the 10 WAM's into the router. No arguments implies that the 10 WAM's in the buffer are loaded. The routers can also be given as 5 hex nos.

BRROUB

Read the router values in the buffer.

BRROUM

Read the router values written by last BWCHM,BVCHM or BRCHM.

BSWCR <,crate pattern> <,%HEXA>

To switch crates on or off. Crate patterns are; forward(%100,%200), top(%400), side(%800,%1000), bottom(%2000), new(%4000) or any summed combination, e.g. t+s+b=%3C00. nb First all crates are switched off.

BSWFF

To set computer mode, reset X.Y cards to 0 switch off X,Y,X.Y & S cards and switch off crates.

BSWIT <,pattern 1> <,pattern 2> ... <,%HEXA>

Switch cards on. All cards are switched off and individual can be switched on (up to a maximum of 40). Each pattern contains;

	crate								card							
15	14	13	12	11	10	9	8	7	6	5	4	3	2	1	0
S	C7	C6	C5	C4	C3	C2	C1								
0								Y4	Y3	Y2	Y1	X4	X3	X2	X1
1								S4	S3	S2	S1	XY4	XY3	XY2	XY1

Patterns quoted will execute, read and update internal table if good. Error will be quoted if disagreement occurs. Argument of %0000 results in the loading of the internal table. If 2 words give the same crate and card type only the last word will be recognised.

BSWXY <,one word> <,0> or <,1>

Switch on/off all XY & S cards associated to modules with X & Y cards ON. Argument is 1=ON,0=OFF. The command switches off all XY & S cards and will only switch them on if the argument is 1 AND all X & Y cards are on in the crate.

BOPXY <xy mode patt.> <,1>,<,3> or <,7>

Switch operation mode of all XY cards

XY mode = 1 for muon chambers alone

3 for inverted H cal.

7 for HC normal

Pattern is read back & checked & an error set if appropriate.

BOPFT <FT mode patt.> <,9>,<,10> or <,12>

Set operation mode of FT.

bit pattern, D0 computer mode (9)

D1 normal mode (10)

D2 selftrigger mode (12)

D3 TTOL bit (=1)

Will not default for error.

BPSU

Checks crate PSU & displays on FT panel, 00 if ok, FF (flashing) if not. Also GREEN diode on sequencer goes out if any crate psu fails.

BWCH <,chip> <,filling id> <,router load>

Write to a chip assuming crate card switched on 'chip' = 1 to 37, 'filling id' = any id of existing fillings (0 = default to be taken from the last chip accessed); 'router load' = 0 loads the router from the last BWROU command; 'router load' = 1 loads the router corresponding to this chip and the crate & card pattern which has just previously been loaded.

BRCH <,chip> <,router load>

To read a chip, arguments as BWCH; filling is returned with the command.

BVCH <,chip> <,filling id> <,router load>

To verify a chip, arguments as BWCH; the number of bad words is returned with the command.

BWCHM [,][module][,][projection][,][chip][,][filling id][, last chip]

To write to a chip or range of chips on a card. Addresses a chip and writes a filling to it. If 'last chip' is given then all chips between the first and last are filled on that card. If not then the default values are those used in the last reference to BWCHM,BRCHM or BVCHM.

BRCHM [,][module][,][projection][,][chip][,last chip]

To read a chip or range of chips.

BVCHM [,][module][,][projection][,][chip][,] [filling id][,last chip]

To verify a chip or range of chips.

BWTT <,module> <,proj.> <,chip> <,tt patt>

Write into given 'mod,proj' the WAMS defined by 'chip,t.t. pattern' mod = 1 − 24, 31 − 34; proj = 1 (short),2 (long); chip = 1 − 37; tt pattern in A0 − A9 expected result in A12.

BEXTT <TTOL flag>

Execute track test and return the results.

APPENDIX C

GAUSSIAN FIT

From chapter IV, one has equation 4.3.5

$$C_i = A\exp-\{(x_i-x_R)^2/d^2\}. \qquad C.1$$

Taking logs,

$$\ln C_i = \ln A - (x_i-x_R)^2/d^2, \qquad C.2$$

which has the form

$$y_i = a - m(x_i-b)^2. \qquad C.3$$

To fit by a least squares method, one differentiates

$$\Sigma w_i(a-m(x_i-b)^2-y_i)^2 \qquad C.4$$

with respect to a, m, and b, and sets the results equal to zero. Here, x_i and y_i are measured quantities, and the summation is over N strips with $N>2$. Solving the three equations for b, m and a, one obtains respectively;

$$\frac{\{.yw.wx.wx^4-w.xyw.x^4w+xyw.x^2w.x^2-xw.x^2w.x^2yw+w.x^2yw.x^3w-yw.x^2w.x^3w.\}}{2\{.w.x^2yw.x^2w-xw.xw.x^2yw-yw.x^2w.x^2w+xw.xyw.x^2w-w.xyw.x^3w+yw.xw.x^3w.\}} \qquad C.5$$

$$\frac{(.yw.wx-w.xyw.)}{(.xw.x^2w-w.x^3w.)-2b(.xw.xw.-x^2w.w.)} \qquad C.6$$

and

$$\{.wy.-m(.wx^2-2bwx+wx^2.)\}/.w.. \qquad C.7$$

Here, the notation requires implicit summations over N for quantities separated by '+', '−' or '.'.

The weight, w_i is found from considering the χ^2 which is fitted, i.e.

$$\chi^2 = \Sigma(y_i-\bar{y})^2/\Delta y_i^2 \qquad C.8$$

where Δy_i is the error on y_i. From above, $y_i=\ln(\alpha N_i)$, where N_i is the number of ADC counts on the i'th strip, and α is a constant from the calibration of the apparatus. The error in the measurement of N_i will be $\sqrt{N_i}$, and by differentiation, $\Delta y_i = 1/\sqrt{N_i}$. Hence the weighting is then

$$w_i = 1/\Delta y_i^2 = N_i \propto C_i. \qquad C.9$$

APPENDIX D

UNFOLDING A DISTRIBUTION WITH A GAUSSIAN ERROR

In the UA1 central drift chamber the one measures the reciprocal of the transverse momentum, $1/p_t$. This quantity has a Gaussian error, described by $\Delta(1/p_t) = \sigma$. It is possible to unfold the real distribution of $d\sigma/dp_t$ from the data by the following method. Let the true (theoretical) distribution be described by $d\sigma = f(u)du$, where $u = 1/p_t$, and is measured as u' with normal errors so that $<u'> = u$, and $\sigma_{u'} = \sigma$. The measured distribution will then be the true distribution integrated over all the possible values of u,

$$g(u')du' = du'(2\sigma^2\pi)^{-1/2}\int e^{-(u-u')^2/2\sigma^2} f(u)du. \qquad \text{D.1}$$

As the value of σ is small, we make the following approximation from the Binomial Theorem,

$$f(u) = f(u') + (u-u')f'(u') + (u-u')^2 f''(u')/2. \qquad \text{D.2}$$

Substituting into D.1, and integrating, we find

$$g(u')du' \approx du'[f(u') + (\sigma^2/2) f''(u')]. \qquad \text{D.3}$$

In order to obtain the true distribution, we need to weight each event by $f(u')/[f(u') + \sigma^2 f''(u')/2]$. This requires a knowledge of f(u), which is paramaterised using the data as $f(u) \propto u^n$. The weight for each event is then $[1 + \frac{\sigma^2}{2} n(n+1)u^{-2}]^{-1}$. In the analysis in chapter VI, we have fitted the parameter, n, by an iterative procedure. A distribution with $n=4$ is first taken and the data corrected by the above method, the parameter n is then fitted by a least squares method (using MINUIT [56]), and then this value used to correct the original data. After several iterations (normally 4) the value of n is found to converge.

REFERENCES

[1] C.Rubbia, P.McIntyre and D.Cline. Producing Massive Intermediate Vector Bosons with Existing Accelerators. Proc. of the International Neutrino Conference: Aachen 1976.

[2] A.Astbury et.al. A 4-π solid angle detector for the SPS used as a Proton-Antiproton collider at a centre of mass energy of 540 GeV. CERN/SPSC/78-06 1978

[3] Proceedings of the School for Young High Energy Physicists. Edited by R.J.Cashmore. RAL-84-009.

The 1984 CERN School of Physics Proceedings. Edited by C.Jarlskog. CERN 85-11.

[4] S.Glashow. Nuclear Physics **22** (1961) 579.

S.Weinberg. Physics Review Letters **19** (1967) 1264.

A.Salam. 1968 in Elementary Physics Theory. Relativistic groups and Analyticity (Nobel Symposium No. 8), edited by Svartholm, Almquist and Wiksell, Stockholm.

[5] see for example the proceedings of the International Colloquium on High Energy Lepton and Photon Interactions, Kyoto, August 1985.

[6] H.Abramowicz et al. Tests of QCD and Non-Asymptotically-Free Theories of the Strong-Interaction by an Analysis of the Nucleon Structure Functions xF_1, F_2, and $\bar{q}$. Z. Phys. **C13** (1982) 199.

H.Abramowicz et al. Neutrino and Antineutrino Charged Current Inclusive Scattering in Iron in the Energy Range $20 < E_\nu < 300$ GeV. Z. Phys. **C17** (1983) 283.

[7] G.Altarelli & G.Parisi. Asymptotic Freedom in Parton Language. Nuclear Physics **B126** (1977) 298.

[8] E.Eichten, I.Hinchliffe, K.Lane and C.Quigg. Supercollider Physics. Fermilab publication 84/17T February 1984.

[9] UA1 collaboration. Angular Distributions and Structure Functions from Two-Jet Events at the CERN SPS $p\bar{p}$ Collider. Phys.Lett. **136B** (1984) 294.

[10] B.Combridge, J.Kripganz and J.Ranft. Hadron Production at Large Transverse Momentum and QCD. Phys. Lett. **70B** (1977) 234.

[11] G.C.Fox and S.Wolfram. A Model for Parton Showers in QCD. Nucl. Phys. **B168** 285. (1980).

[12] C.Peterson, D.Schlatter, I.Schmitt and P.M.Zerwas. Scaling violations in inclusive e^+e^- annihilation spectra. Phys. Rev. **D27** (1983) 105.

[13] R.D.Field and R.P.Feynman. A Parametrization of the Properties of Quark Jets. Nucl. Phys. **B136** (1978) 1.

[14] B.Andersson, G.Gustafson and C.Peterson. A Semiclassical Model for Quark Jet Fragmentation. Z. Physik. **C1** (1979) 105.

[15] D.H.Perkins. Introduction to High Energy Physics. Addison-Wesley Publishing Company, Inc..

[16] R.Horgan & M.Jacob. Jet production at Collider Energy. Nuclear Physics **B179** (1981) 441.

[17] UA1 collaboration. A proposal to upgrade the UA1 detector in order to extend its physics program. CERN/SPSC/83-48 1983.

[18] S.van der Meer. Stochastic cooling and the accumulation of antiprotons. Reviews of Modern Physics, **57** 3 part 1 (1985).

[19] M.Calvetti, J.Timmer, Y.G.Xie. Measuring dE/dx in the central detector. UA1/TN83-80 1983.

[20] M.J.Corden et al. Central Hadron Calorimeter of UA1. Nuclear Instruments and Methods **A238** (1985) 273.

[21] A.Astbury et al. The UA1 Calorimeter Trigger. Nuclear Instruments and Methods **A238** (1985) 288.

[22] M.Della Negra et al. 168E's in 1983 Run. UA1/TN84-35.

[23] R.Bock, E.Pagiola, J.Zoll. HYDRA Systems Manual, CERN publication, 1 March 1972.

[24] I.R.Kenyon. Guide to the DST package. UA1 technical note, 12/8/82.

[25] The UA1 collaboration. Observation of the muonic decay of the charged intermediate vector boson. Phys. Lett. **134B** (1984) 469.

[26] J.Streets and M.J.Corden. Muon Trigger Efficiency. UA1 Technical note 18 March 1984.

[27] H.Reithler. Hardware Improvements for the muon Fast Trigger. UA1 Technical note 10 July 1983.

[28] The UA1 collaboration. A proposed upgrade of the forward muon detection in UA1. CERN/SPSC/83-79.

[29] H.Reithler and J.Streets. Tentative manual for the VMEFT program. UA1 Technical note 12 May 1984.

[30] M.Demoulin. Preliminary version of some features of CPUA1MON. private communication, 27/5/84.

[31] J.Streets. Status of offline analysis of the first level muon trigger. Transparencies presented at run meeting, 11 October 1984.

[32] UA1 collaboration. A proposed upgrade of the large angle muon detection in UA1. CERN/SPSC/82-51.

[33] I.R.Kenyon. Measurement of momenta for muons using side chambers and central detector. TN83-39 1983.

[34] G.Battistoni et al. Resistive Cathode Detectors with Bidimensional Strip Readout: Tubes and Drift Chambers. Nuclear Instruments and Methods **176** (1980) 297.

[35] G.Battistoni et al. Resistive Cathode Transparency. Nuclear Instruments and Methods **202** (1982) 459.

[36] G.Battistoni et al. Electrodeless Plastic Streamer Tubes. Nuclear Instruments and Methods **217** (1983) 429.

[37] G.Bauer et al. Resolution of Plastic Streamer Tubes with Analog Strip Readout. (In preparation).

[38] S.Centro. Star System Description. UA1 Technical Note, PD-5.4.1984.

[39] A.Bettini et al. Some tests on the readout of Iarocci tubes with X-ray source. PDUA1 83/1 1983.

[40] Mark 1 Collaboration, G.Hanson et. al. Phys. Rev. Lett. **35** (1975) 1609.

[41] Results from the UA2 experiment, presented by J.P.Reppelin at the 21st International conference on high energy physics. (Paris,1982) C3-571.

[42] See for instance, T.J.V.Bowcock. Ph.D. Thesis, University of London.

[43] Ph.Ghez, Ph.D. Thesis, Annecy (LAPP), in preparation.

[44] I.Kenyon and J.Streets. Some comments on jet studies at Birmingham. UA1/TN83-13 1983.

[45] UA1 Collaboration. Experimental Observation of Events with a Large Missing Transverse Energy Accompanied by a Jet or Photon(s) in $p\bar{p}$ Collisions at $\sqrt{s}$ = 540 GeV. Phys. Lett. **139B** (1984) 115.

[46] F.E.Paige and S.D.Protopopescu. ISAJET version 4.10, BNL 29777, 1981.

[47] The UA1 Collaboration. Intermediate-Mass Dimuon Events at the CERN $p\bar{p}$ Collider at $\sqrt{s}$= 540 GeV. Phys. Lett. **147B** (1984) 241.

[48] Associated Production of an Isolated, Large Transverse Momentum Lepton (Electron or Muon), and Two Jets at the CERN $p\bar{p}$ Collider. Phys.Lett. **147B** (1984) 493.

[49] Talks given by A.Ali and B. van Eijk at the 5^{th} Topical Workshop on $p\bar{p}$ Collider Physics. Aosta, February 1985. pages 165 & 272. Edited by M.Greco.

[50] The UA1 Collaboration. W Production Properties at the CERN SPS Collider. Lett. Nouvo Cimento **44** 1 1. (1985)

[51] J.Ransdell. Phd. Thesis , Riverside, in preparation.

[52] N.Ellis. ISAJET monte carlo study (private communication).

[53] N.Ellis, M.Jimack, J.Streets. Estimation of the Background to the Dimuon Sample from $\pi^{\pm}$ and $K^{\pm}$ Decays in Flight. UA1 Technical Note, July 30 1985.

[54] M.Banner et al. Inclusive Charged particle production at the CERN $p\bar{p}$ Collider. Physics Letters **122B** (1983) 322.

[55] Particle Data Group. Review of Particle Properties. Reviews of Modern Physics **56** 2 II, April 1984.

[56] F.James and M.Roos. Function Minimization and Error Analysis. CERN Computer Centre Program Library, D506.